Buckling of spherical shells with large axisymmetric imperfection and application in soft robotics

By

Chuan Qiao

Department of Mechanical Engineering

McGill University

Montreal, Quebec, Canada

April 2021

A thesis submitted to McGill University in partial fulfillment of the requirements for a doctoral degree

Dedication

To my father and mother

Abstract

Spherical shells are ubiquitous in nature and engineering for their simple geometry and excellent load-bearing capacity. A long-standing topic of spherical shells subject to uniform external pressure is their highly unstable post-buckling response that leads to a catastrophic collapse. This type of failure fully exhausts the load-bearing capacity of the shell, and it is thus detrimental for traditional engineering applications. On the other hand, recent advances in soft robotics and metamaterials demonstrate that geometric nonlinearities and elastic instabilities can be harnessed to generate distinctive functions, such as shape morphing, fast motion, and logic operation.

This thesis proposes the use of a large axisymmetric imperfection to control the buckling mode of spherical shells, and demonstrates its application when integrated into a soft bi-shell valve for the fast actuation of soft robots. On the first front, the proposed imperfection can escape the classical bifurcation of perfect spherical shells, and induce snap-through buckling followed by a stable post-buckling; this response provides increasing pressure resistance over a large change in volume. The buckling of the imperfect shell is investigated through a theoretical study that employs exact expressions of the middle surface strains, curvature changes, and live pressure loading along with validating experiments and numerical simulations. The post-buckling characteristics and transition between four buckling modes can be programmed by tuning the defect geometry and shell radius to thickness ratio. On the second front, a new concept for soft valves is proposed: a bi-shell valve consisting of an imperfect shell and a shallow spherical cap. The bi-shell valve harnesses the snap-through interaction of the constituent shells to convert a slowly imparted volume into a fast volume output. Upper bounds and performance metrics are presented to guide the design of the bi-shell valve, and its performance is illustrated through an application that demonstrates the fast actuation of a soft striker.

Overall, the work in this thesis contributes to unveil original aspects of shell buckling with results that are promising for diverse applications. Geometric imperfections can be programmed into spherical shells to trigger new buckling modes that can be exploited for the design of soft robots, mechanical metamaterials, and soft matter. Furthermore, the bi-shell valve concept here introduced can inspire the design of future soft valves with unique actuation modes for soft pneumatic robots.

Résumé

Les coques sphériques sont omniprésentes en sciences naturelles et en ingénierie en raison de leur géométrie simple et leurs excellentes propriétés mécaniques. En particulier, les coques sphériques soumises à une pression externe uniforme sont étudiées exhaustivement pour leur régime post-flambement instable qui résulte en une défaillance catastrophique. Ce mode de défaillance doit être évité pour les structures d'ingénierie traditionnelles puisqu'il limite leur capacité de support de charge. Cependant, les avancées dans le domaine des robots souples et des métamatériaux permettent d'utiliser les instabilités élastiques afin de générer de nouvelles fonctionnalités comme la transformation de forme et l'amplification de la réponse des structures.

Cette thèse formalise l'utilisation d'imperfections axisymétriques pour contrôler le flambement de coques sphériques. Une application sur une valve bi-coque souple est mise de l'avant pour illustrer que le concept permet d'augmenter la réponse des robots souples. En premier lieu, il est démontré qu'en raison de l'imperfection axisymétrique, la réponse de la coque diffère du résultat classique de bifurcation pour une coque sans imperfection. L'imperfection produit un flambement à pression constante suivi d'un régime post-flambement stable. Cette réponse non-linéaire de la coque fournit une augmentation de la résistance à la pression externe associée à un grand changement de volume. Le flambement de la coque imparfaite est étudié théoriquement à l'aide d'une formulation exacte de la déformation de la surface moyenne, des changements du rayon de courbure et de la pression. Cette approche théorique est par la suite validée par des expériences sur des prototypes et des simulations numériques. Le régime post-flambement et la transition entre quatre modes de flambement peuvent être programmés en modifiant le défaut de géométrie ainsi que le rapport entre le rayon et l'épaisseur de la coque. En deuxième lieu, il est proposé un nouveau concept pour une valve souple: une valve bi-coque construite à partir d'une coque avec une imperfection axisymétrique et une autre coque sans imperfections, mais avec un angle polaire très faible. Cette bi-coque utilise l'instabilité de flambement afin de convertir un débit de volume d'entrée lent en un débit de sortie rapide. Il est aussi présenté les limites du concept ainsi que des métriques de performance pour comparer le design avec la littérature scientifique. Le potentiel de la bi-coque flexible est démontré à travers l'actuation rapide d'un robot souple perforeur.

Cette thèse met de l’avant le flambement élastique de coques ainsi que les imperfections de géomtérie qui peuvent être utilisés dans le design de robots souples, de métamatériaux, et de matière désordonnée. Finalement, le concept de bi-coque présenté dans cette thèse pourrait alimenter le développement de valves souples munies de nouvelles fonctionnalités.

Acknowledgment

I would like to take this chance to express my sincerest thanks to a group of people including my supervisor, my friends and my family for their help and support. First, I would like to express my thanks to my PhD supervisor, Professor Damiano Pasini, who gave me the opportunity to study at McGill and guided me into the amazing world of shell buckling. I have benefited so much from his scientific vision, technical guidance and expertise, as well as his continuous encouragement during my PhD study. I am grateful for his advices in my research as well as career. I am also especially thankful for his help with the difficulties emerged during the COVID-19 pandemic.

I would like to thank the nice friends of “The Pasini Group” whom I have had pleasure to meet and work with. First, I wish to thank Lu Liu, who worked with me on several projects and helped me a lot with both my research and my life in Montreal. I would like to thank David Melancon and Nicholas D'Ambrosio who helped me with French and English. My gratitude goes to Haichao An whom I collaborated with. I would like to express my thanks to other members in our group: Hang Xu, Ahmed Moussa, Amin Jamalimehr, Asma El Elmi, Ruizhe Ma, Morad Mirzajanzadeh, Shakurur Rahman, Xiao Shang, Carlos Gil Yáñez, Wendy Li, Lei Wu, Amr Farag, Gerard Reynolds, Amirmohammad Rahimizadeh, Jiazhen Leng, Aziz Madrane, Meisam Asgari, Yingjun Wang, and many others, thank you for the good times and precious memories.

I would like to thank my parents. They are the most important people to me and have given me endless love and support, encouraging me to pursue my goals.

Finally, I would like to thank the National Sciences and Engineering Research Council of Canada (NSERC), and the McGill Engineering Doctoral Award (MEDA) for their collaborative financial support.

Table of contents

List of figures

List of tables

Contribution of the author

This is a manuscript-based thesis consisting of two journal articles. The title of the articles, name of the authors, and their contributions are listed below:

1) Elastic thin shells with large axisymmetric imperfection: from bifurcation to snap-through buckling

Chuan Qiao, Lu Liu, Damiano Pasini

Department of Mechanical Engineering, McGill University, Montreal, Quebec H3A 0C3, Canada

Journal of the Mechanics and Physics of Solids, 2020. 141, 103959.

***Author contributions**:*

C.Q.: Conceptualization, Methodology, Investigation, Validation, Writing - original draft.

L.L.: Methodology, Software.

D.P.: Conceptualization, Methodology, Investigation, Supervision, Writing - original draft, Writing - review & editing, Project administration, Funding acquisition.

2) Bi-shell valve for fast actuation of soft pneumatic actuators via shell snapping interaction

Chuan Qiao, Lu Liu, Damiano Pasini

Department of Mechanical Engineering, McGill University, Montreal, Quebec H3A 0C3, Canada

Advanced Science, 2021, 2100445. https://doi.org/10.1002/advs.202100445

***Author contributions**:*

C.Q.: proposed the preliminary idea under D.P. guidance, developed the concept, designed the research, fabricated the prototypes, performed the experiments and conducted the FEM simulations, and wrote the manuscript.

L.L.: developed the concept and fabricated the prototypes.

D.P.: guided C.Q. to propose the preliminary idea, developed the concept, designed the research, wrote the manuscript, and supervised the research

Chapter 1

Introduction and literature review

Chapter 1: Introduction and literature review

1.1 Pressurized spherical shells

1.1.1 Background

A spherical shell is a unique three-dimensional structure that not only can enclose a given volume with the smallest surface area, but has also a good load-carrying capacity that provides both structural support and protection. Spherical shells are widespread in nature across different length scales from virus shells [1], cell walls of baker's yeast [2], and pollen grains [3], to gecko eggs [4] and coconut shells [5, 6] (Figure 1-1).

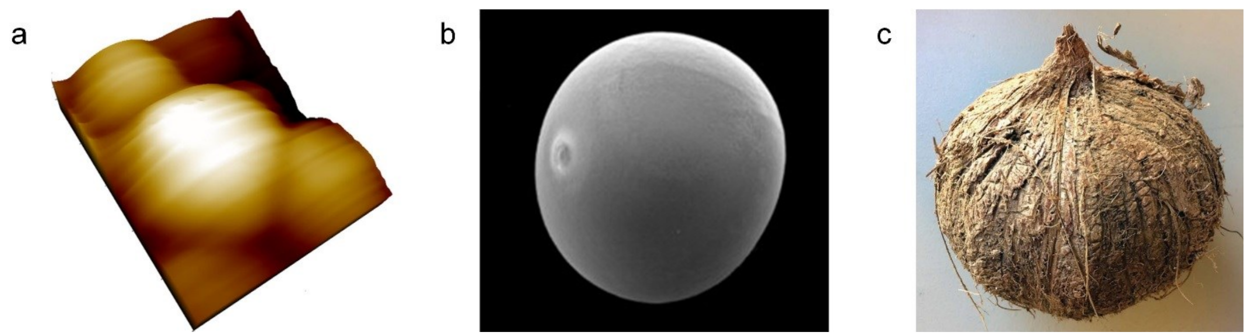

Figure 1-1 (a) AFM topography image of yeast cells [2]. (b) Pollen grain of Zea mays [3]. (C) Photograph of a coconut shell [6].

In engineering, spherical shells have also broad applications, with the early examples dating back to the 1600s when the Italian aeronautics pioneer Lana de Terzi [7] first proposed a hypothetical airship that operates with the buoyancy of multiple evacuated spheres (Figure 1-2a). His concept was later proved theoretically possible by vacuum structures with a near-spherical geometry [8, 9]. Another famous example is the Magdeburg hemispheres, which were made of a pair of large copper hemispheres to demonstrate the power of atmosphere pressure [10]. When the air inside the Magdeburg hemispheres was extracted by a vacuum pump, even two teams of horses could not pull the Magdeburg hemispheres apart (Figure 1-2b).

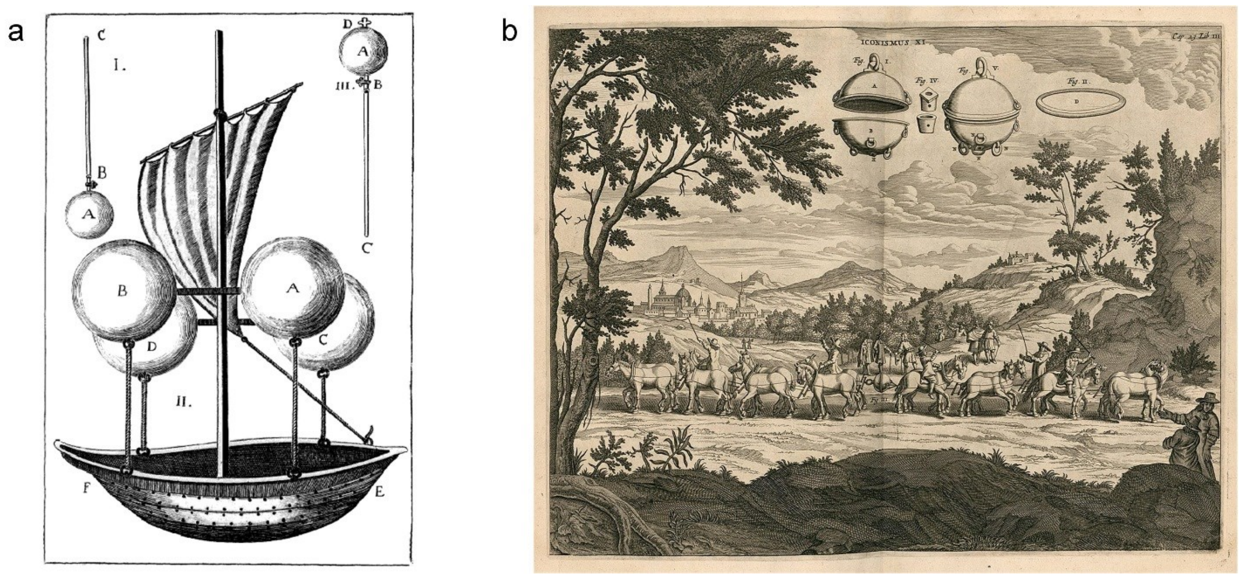

Figure 1-2 Early applications of spherical shells. (a) The vacuum airship of Lana de Terzi. The ship flies with the buoyance of four vacuum spheres [7]. (b) The Magdeburg hemispheres. The horses fail to pull the evacuated hemispheres apart [10].

In more recent years, spherical shells have played and continue to play a very distinct role in a multitude of engineering sectors (Figure 1-3). They appear at the microscale, e.g. carbon nanospheres [11], nanocomposite spherical caps [12], microcapsule for drug delivery [13], and microscopic actuators [14], as well as at the macroscale, e.g. aerospace vehicles [15], underwater pressure hulls [16, 17], underwater robots [18], pressure vessels [19], impact energy absorbers [20], Plexiglas protective shields [21], soft robots [22, 23], and many others.

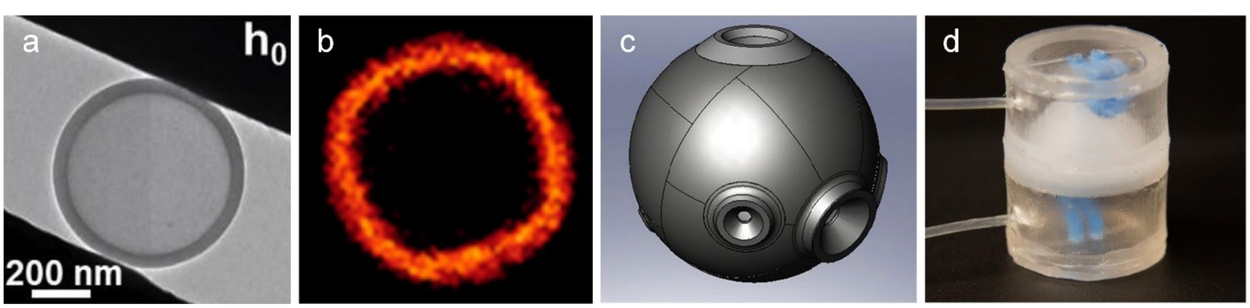

Figure 1-3 Examples of recent applications of spherical shells. (A) Carbon nanosphere [11]. (B) Microcapsule for drug delivery [13]. (C) Underwater pressure hull [19]. (D) Soft robot [22].

The most harmful loading applied to a spherical shell is an external pressure, which causes the classical abrupt and catastrophic collapse characterized by bifurcation buckling (Figure 1-4). Two reasons make bifurcation buckling difficult to predict. First, the pre-buckling shape of the sphere is almost identical to the undeformed one, a factor making buckling prediction from deformation challenging. Second, since the buckling pressure is extremely sensitive to the initial geometric imperfections, even a small defect can severely impair the pressure resistance of the shell, another factor that makes the buckling event even more unpredictable.

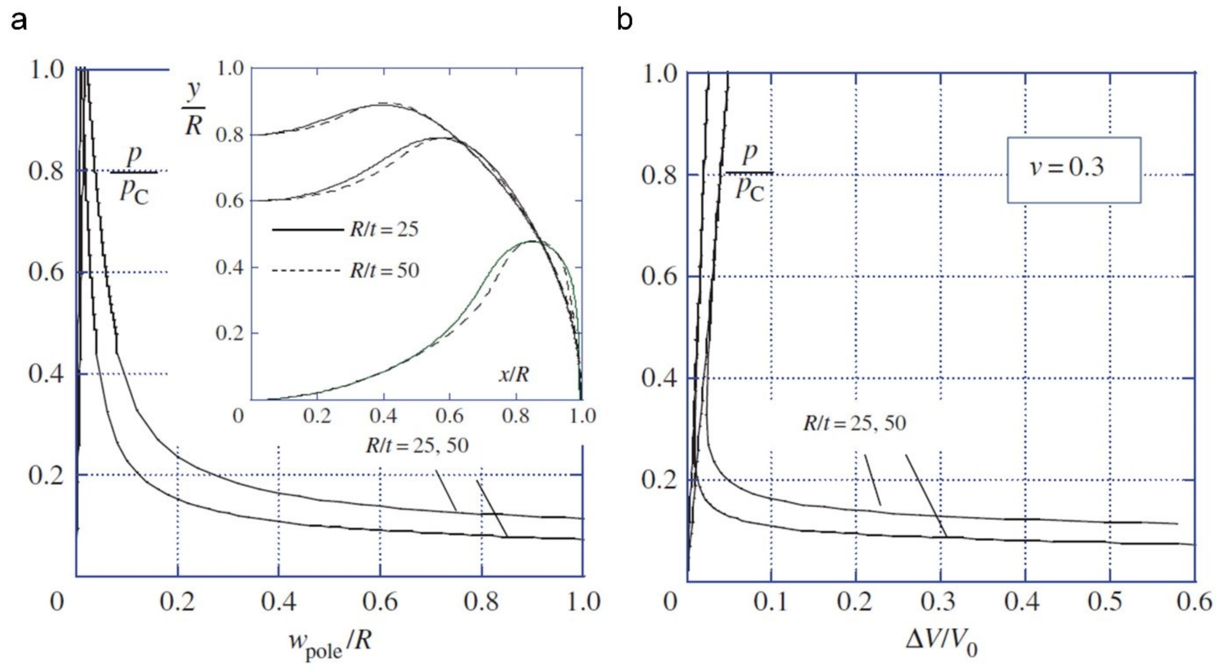

Figure 1-4 Axisymmetric buckling behavior of spherical shells based on shell theory [24]. (a) Pressure-pole displacement curves. (b) Pressure-volume change curves. The normalization factors are the theoretical buckling pressure p_C, the sphere radius R, and the negative of the volume within the middle surface of the undeformed sphere V_0. The insert in (a) shows the deformed middle surface at three stages of deformation.

In this thesis, we focus on the buckling behavior of imperfect spherical shells subject to external pressure and we use the novel insights gained from this analysis to design a soft valve for soft pneumatic robots. The following survey consists of two parts. The former focuses on the mechanics of perfect spherical shells followed by a detailed review shedding light on the role of geometric imperfections. The latter examines soft robots that use elastic shells to achieve a number of functionality and performance that have broad application in engineering and beyond.

1.1.2 Perfect spherical shells

Externally pressurized spherical shells with perfect geometry can fail by following one of two deformation mechanisms. One is plastic yielding, characterized, for example, by the maximum stresses reaching the yield strength of the base material; the other is elastic buckling [25]. The lowest value of external pressure that triggers one of these two modes determines the failure pressure of the spherical shell.

For the former failure mode, i.e. plastic yielding, the equi-biaxial compressive stress of an externally pressurized spherical shell in the uniform state σ is simply

$$\sigma = \frac{pR}{2t} \tag{1-1}$$

where p is the pressure, R is the shell radius, and t is the shell thickness.

If the yielding occurs when the maximum stress reaches the yield stress σ_{Y}, then the pressure at yielding p_{Y} can be expressed as

$$p_{\mathrm{Y}} = \frac{2t\sigma_{\mathrm{Y}}}{R} \tag{1-2}$$

For the latter failure mode, i.e. elastic buckling, the theoretical buckling pressure of a spherical shell subject to external uniform pressure was first derived by Zoelly [26] and van der Neut [27] through a linear buckling theory as

$$p_{\mathrm{C}} = \frac{2E}{\sqrt{3\left(1-\nu^2\right)}}\left(\frac{t}{R}\right)^2 \tag{1-3}$$

where p_{C} is the buckling pressure, E is the Young's modulus, ν is the Poisson's ratio, and t/R is the thickness to radius ratio. According to Eqs. (1-2) and (1-3), the spherical shell can undergo elastic buckling when the buckling pressure is lower than the yielding pressure $p_{\mathrm{C}} < p_{\mathrm{Y}}$, a condition that requires

$$\frac{t}{R} < \frac{\sigma_y \sqrt{3\left(1-\nu^2\right)}}{E} \tag{1-4}$$

Hutchinson [24] recently revisited the buckling of a spherical shell under uniform external pressure. Using the buckling analysis of a thin shell, he derived the lower bound estimate of the lowest eigenvalues, i.e. buckling stress and buckling pressure, which reproduced the results of Koiter [28]. From the PhD thesis of van der Neut [27], Koiter found that the spherical shell has simultaneous axisymmetric and non-axisymmetric eigenmodes when it bifurcates from the uniformly compressed state, and he reached the same result using the moderate rotation theory. In Figure 1-5, Hutchinson plotted two examples of the axisymmetric mode for shells with different radius to thickness ratio R/t, where the inward deflection at the upper pole w_{pole} is enlarged for visualization purposes. While Koiter noted that the buckling pressure for some radius to thickness ratios, R/t, is slightly different from Zoelly's prediction in a relative order R/t, Hutchinson pointed out that the difference is never larger than 1%, a value obtained through numerical calculations that use the moderate rotation theory under either live or dead pressure conditions. Therefore, Zoelly's buckling pressure is universally regarded as the buckling pressure of a perfect spherical shell.

For a complete spherical shell, Walker [29] theoretically studied the non-linear post-buckling behavior in the vicinity of the buckling pressure. The author assumed that the buckling of the shell has a rotationally symmetric wave pattern, and he gave specific attention to the deformation modes that are symmetric about the equator, in the longitudinal direction. He employed a series expansion technique to approximately solve the algebraic equations of equilibrium, while two types of assumed functions are considered, viz. Legendre polynomials and localized Rayleigh functions (finite elements). His results show that the exact coefficients of the series can be directly obtained with Legendre polynomials, while in the finite element method, the coefficients converge monotonically to the exact values with the increase in the number of elements.

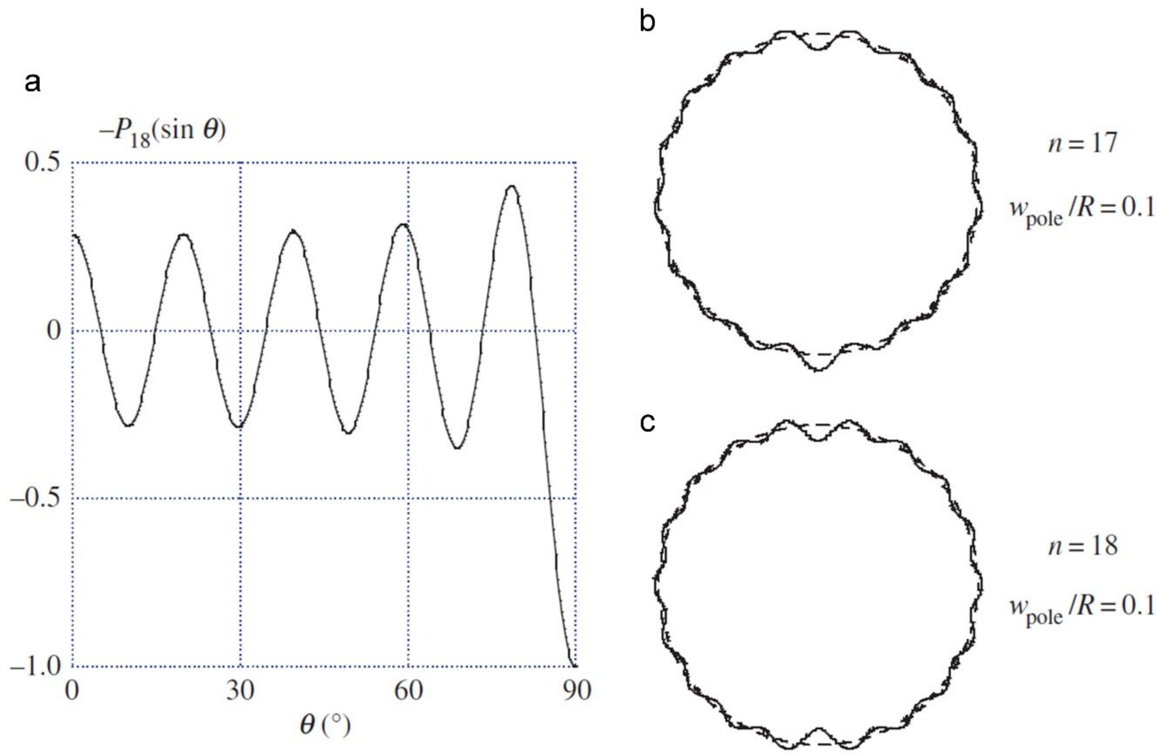

Figure 1-5 (a, c): the axisymmetric bifurcation mode symmetric about the equator for the perfect shell with $R/t = 103.5$ and $\nu = 0.3$. θ is the meridional angle defined as $\theta = 0^{\circ}$ at the equator and $\theta = 90^{\circ}$ at the upper pole. (b), the axisymmetric bifurcation mode antisymmetric about the equator for $R/t = 92.6$ and $\nu = 0.3$ [24].

Zhukov and Srubshchik [30] investigated the post-buckling behavior of a closed spherical shell. Using the Liapunov-Schmidt method for a broad class of operator equations in the Banach space, the authors considered new equilibrium modes of a uniformly compressed elastic shell with closed spherical geometry when the loading pressure approaches the critical value and triggers instability in the shell.

Hill [31] obtained closed-form expressions of the buckling pressure of a thick-walled spherical shell that buckles under a uniform external pressure. He considered a particular isotropic incompressible hyperelastic material, which involves handling a fourth-order system of highly nonhomogeneous ordinary differential equations. His solutions were used to derive the buckling criterion, which can be solved numerically to obtain the critical pressures. The predictions are in agreement with results obtained for thin shells through classical theory as well as with existing results for thicker shells modelled with a neo-Hookean material.

1.1.3 Imperfect spherical shells

1.1.3.1 Experimental buckling pressure

Recently, Wagner et al. [32] summarized a collection of experimental data for isotropic spherical shells under external pressure from different sources (Figure 1-6). The geometry of the shell is defined by a dimensionless shape parameter λ

$$\lambda = \sqrt[4]{12\cdot\left(1-\nu^2\right)}\cdot\sqrt{\frac{R}{t}}\cdot 2\cdot\sin\left(\frac{\phi}{2}\right) \tag{1-5}$$

where R is the radius, t is the thickness, ϕ is the angular width of the spherical cap measured from its symmetry axis, and ν is the Poisson's ratio. The experimental buckling pressure is represented with the knockdown factor (KDF) κ_d, which is defined as the ratio of the measured buckling pressure of a manufactured shell $p_{\max}$ over the theoretical buckling pressure of a perfect shell p_{C}

$$\kappa_d = \frac{p_{\max}}{p_{\mathrm{C}}} \tag{1-6}$$

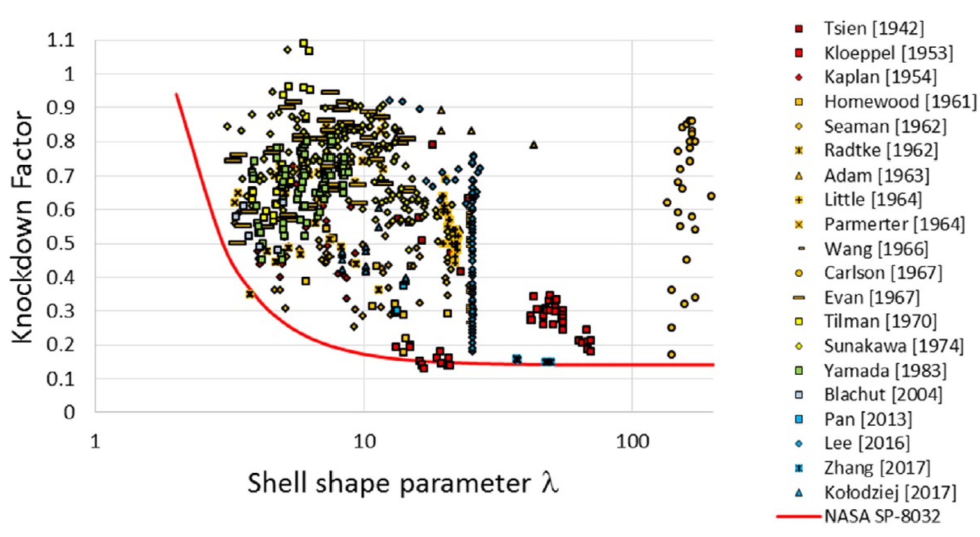

Figure 1-6 Distribution of experimental data of spherical shells under external pressure [25].

For perfect spherical shells that are free from geometric defects and buckle at the theoretical buckling pressure in Eq. (1-3), $\kappa_d = 1$. However, for imperfect shells that have defects due to manufacturing, a broad scattering of the measured buckling pressure is observed in Figure 1-6; the worst cases are far from the baseline of the theoretical prediction with a drop that can be as high as 80%. Although the theoretical buckling pressure provides a reference for the design of spherical shells, the buckling pressure measured in experiments often fails to match the theoretical prediction. In addition, the experimental knockdown factor can be above 1 when a stable asymmetrical mode occurs before the final buckling in the common dimple-like mode [33].

In 1939, von Kármán and Tsien [34-36] were among the first to investigate the discrepancies between theoretical predictions and experimental results. They proposed a "lower" buckling load based on the post-buckling state that is dependent on neither the initial geometric imperfection nor the loading arrangement. Later in 1945, Koiter [37] developed a general theory of elastic stability that unveils the buckling sensitivity of imperfect spherical shells subject to external pressure. An asymptotic method was used to capture the relation between imperfection sensitivity and initial post-buckling behavior. Following Koiter's seminal work, an extensive study was performed to investigate the buckling load of imperfection-sensitive structures [38]. Since Koiter's method relies on the perturbation expansion of the perfect shell, Lee, Hutchinson and co-workers [24, 39] have recently demonstrated that Koiter's method is only valid for an extremely small range of the normal displacement at the pole in the post-buckling region; this is because the classical mode quickly localizes at the pole after bifurcation to form a dimple-like mode. More comprehensive reviews on the buckling of imperfect spherical shells under external pressure in history can be found in references [24, 40, 41].

Since the imperfections in experimentally fabricated shells have random sizes, shapes, and distributions, the deterministic relationship between the representative distribution of defects and the load-bearing capacity of the shell has rarely been found [39]. An alternative approach to circumvent this difficulty in shell design is to investigate imperfection sensitivity with equivalent or substitute imperfections that are intentionally introduced into an ideal shell geometry [32]. The substitute imperfections are usually studied with numerical or theoretical methods, while experimental investigations only recently become available with advances in fabrication techniques that enable to precisely engineer imperfections [39, 42, 43]. In the following subsections, we briefly review the substitute imperfections that have recently attracted most research attention.

1.1.3.2 Local dimple imperfection

The simplest form of imperfection is a local inward dimple, which can be either a dimple with an arbitrary shape or a dimple induced by indentation (Figure 1-7 a and b). While the former is determined by the choice of the researcher, the latter is obtained from the deformation pattern due to indentation. For the first type, Budiansky [44] used nonlinear shallow shell theory to study a clamped shallow shell with a dimple-like imperfection. The geometry of the dimple was expressed as an analytical function of the distance from the symmetry axis of the shell. While an inward dimple typically decreases the buckling pressure, an outward dimple can increase it for shallow shells. Koga and Hoff [45] studied the dimple imperfection examined by Budiansky [44] and found that the buckling pressure has a minimum value for dimples defined by a varying geometric parameter. More recently, the sensitivity of a Gaussian dimple was also studied by Lee et al. [39].

For the second type, Wagner et al. [32] studied a dimple imperfection in the form of a local concentrated indentation. This defect was induced in a first load step of the numerical simulation before applying pressure on the surface of the shell. With a sensitivity study of the knockdown factor to the amplitude of the dimple, three regions were identified. For shallow dimples (indentation displacement $v/t < 0.5$), the knockdown factor is nearly constant (~0.9). When the dimple amplitude further increases, the knockdown factor quickly drops for $v/t \geq 0.5$ until reaching a plateau (~0.1) at $v/t = 1.5$. Furthermore, Błachut examined a shell with inward dimple induced by a concentrated radial force and found the decrease in the knockdown factor before reaching a plateau value [46, 47].

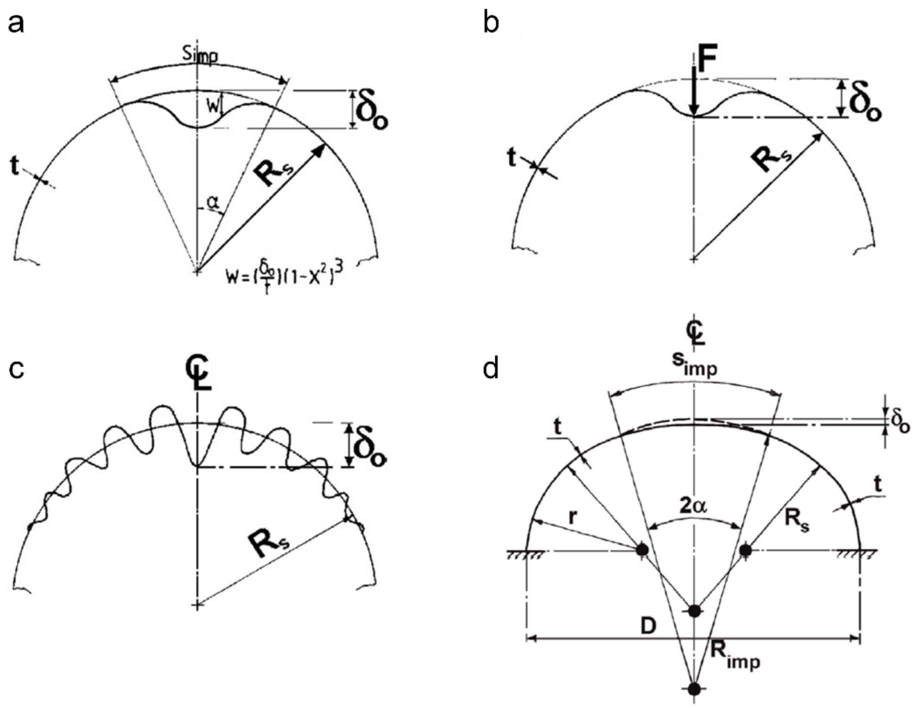

Figure 1-7 Types of imperfections [47]. (a) Dimple of arbitrary shape. (b) Force-induced dimple. (c) Eigenmode imperfection. (d) Local flattening.

1.1.3.3 Buckling eigenmode imperfection

The so called "buckling eigenmode imperfection" is one of the most frequently used types of imperfection. It is typically superimposed onto a shell with perfect geometry through a scaling factor (Figure 1-7c). Similar to the case of a dimple imperfection, the knockdown factor first decreases quickly with the amplitude of the eigenmode imperfection until it reaches a plateau [46, 48]. While effective, this approach has some drawbacks. First, the choice of the eigenmode is not unique because several deformation states are possible for a given pressure and a prescribed imperfection amplitude [49]. Second, the eigenmode imperfections often feature a complex shape, which might be questionable as the realistic counterpart might not necessarily exist [46]. The results from imperfection sensitivity, therefore, might be of limited use for practical shells. Third, it is not clear how to choose an imperfection amplitude that can provide a general conservative lower-bound estimation of the buckling pressure [32, 50].

1.1.3.4 Increased-radius flat spots

Fabricated spherical shells often feature flat spots of various size and radius [47, 51, 52]. In Figure 1-7d, the geometry of the flat spot is defined by the imperfection amplitude δ_0, the semi-angle α, and alternatively the increased radius R_{imp}. For a spot with a given amplitude δ_0 or semi-angle α, the magnitude of the increased radius R_{imp} can be an infinite number if the spot is completely flat. By varying R_{imp} for a given δ_0, the lower bound of the buckling pressure can be obtained through numerical simulations, and the result has been benchmarked against experimental data [19, 53]. Similar to other imperfections, the knockdown factor decreases with the amplitude of the flat spot until reaching a plateau [39]. It is also possible that the buckling pressure of imperfect shells can stay near the theoretical buckling pressure for a range of imperfections with small amplitude at the apex [46].

1.1.3.5 Other types of imperfections

Besides the abovementioned imperfections, other types of imperfections have also been explored by several other authors. Wagner et al. [32] introduced perturbation cutouts to determine the lower bound of buckling pressure. Their results show a robust agreement with a large collection of experimental data. Paulose and Nelson [54] investigated an inhomogeneous shell with a circular soft spot that is made of the same material as the rest of the shell but with reduced thickness. From a numerical study, they found that the shell can undergo either a single buckling transition or two separate buckling transitions depending on the imperfection geometry; the results were later corroborated by experiments conducted by Yan et al. [43]. For brittle shells, Zhang et al. [55] found that thickness-reduced spots can also affect the collapse sites. When the area and magnitude of thickness-reduced spots are small, most shells exhibit global instability. On the other hand, when the area and magnitude of the thickness reduction are large, buckling occurs locally on the boundary of the thickness-reduced spots.

1.1.4 Research gaps on pressurized spherical shells

The buckling of spherical shells under external pressure is catastrophic for two reasons. First, it is challenging to predict buckling from either the shell deformation or the applied pressure. The deformation prior to buckling, for example the radial displacement, is tiny compared to the radius of the shell. On the other hand, the buckling pressure scatters in a wide range due to the extreme sensitivity to imperfections. Second, once buckling occurs, the shell immediately loses pressure resistance and becomes unstable, which would lead to a full eversion of the shell under prescribed pressure. While the effects of imperfections on the buckling pressure of spherical shells have been extensively studied [32, 39], how to avoid the disastrous post-buckling behavior with as-designed imperfections has received less attention. Within this context, this thesis aims at contributing to address the following research gaps.

- First, while only a few attempts have managed to find new buckling pathways by locally decreasing the shell thickness [43, 54, 56], the immediate collapse of the shell occurring at an extremely small volume change is still a behavior that cannot be bypassed .
- Second, the focus of the existing literature is limited to small-sized imperfections whose amplitude is close to the thickness of the shell [32, 46]. The effects of large defects with an amplitude comparable to the radius of the shell is yet to explore.

1.2 Soft pneumatic robots

While traditional applications employ spherical shells as structural elements to carry load, emerging frontiers of research, e.g. soft pneumatic robots, exploit the nonlinear buckling response of spherical shells to perform new functional tasks involving for example shape morphing, fast motion, and logic computation. In this section, we review the research on soft pneumatic robots with an emphasis on their actuation methods and their control with soft valves.

1.2.1 Background

Soft robots are pushing the boundaries of robotic applications by tackling tasks that are difficult to accomplish for traditional rigid robots [57]. The advantage of building robots with compliant materials is that they can undergo large elastic deformations with small actuation forces, which is inherently suitable for complex shape morphing [58], passive adaptation to unknown environment [59], handling of delicate objects [60], and safe collaborations with human [61, 62] (Figure 1-8). In these scenarios, the application of rigid robots is limited by the requirement of a complex control system that has to precisely regulate the force and movement of the robot. On the other hand, soft robots can reduce the control requirement by leveraging the trade-off between morphology and control, thereby passively governing the response of the soft robotic body. This approach is known as "morphological computation" or "material intelligence", which embeds control into the physical structure of the robot [22, 63-66]. Other advantages of soft robots include low mass and cost, high cycle life, and damage resistance to impact [57, 67, 68].

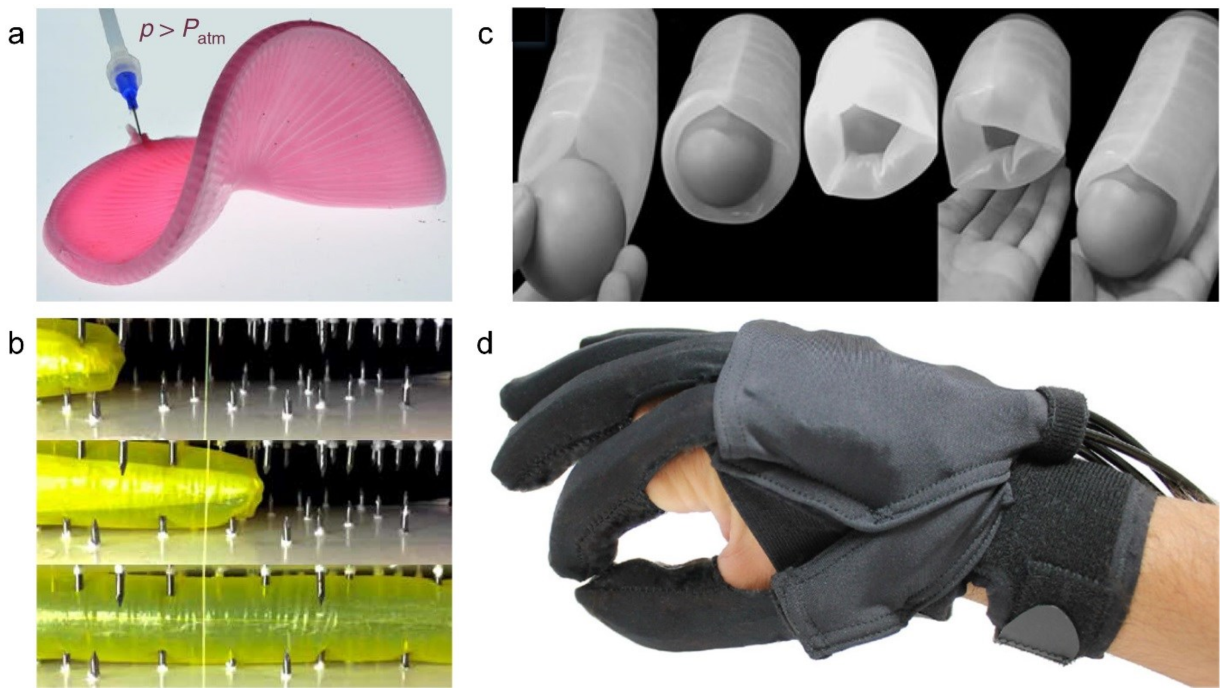

Figure 1-8 Application of soft robots. (a) Complex shape morphing [58]. (b) Passive adaptation to unknown environment [59]. (c) Handling of delicate objects [60]. (d) Safe cooperation with human [61].

Among soft robots, soft pneumatic robots have gained huge attention because of their simple structural design, high energy and force density, and fast actuation speed with large stroke [69, 70]. A broad range of applications with soft pneumatic robots have emerged. These applications can be loosely categorized into locomotion, manipulation, and human-robot interaction [63, 71]. Locomotion of soft robots has recently been summarized by Calisti et al. [72], who listed multiple modes such as crawling [73], legged locomotion [74], jumping [23], swimming [75], and others [22, 76]. Soft robotic manipulation is achieved with three methods: jamming of granular materials

[77], grasping in an octopus-like manner [78], and grasping with fingers [79, 80]. Soft robots used in human-robot interaction include implantable devices [81], surgical tools [82], and wearable devices [61, 62].

In the following subsections, we first focus on the actuation methods of soft pneumatic robots and then review the applications of soft valves in the actuation control of soft robots.

1.2.2 Actuation methods

The actuation of soft pneumatic robots is achieved by one of these two approaches: 1) inflation or deflation of fluid in a system of internal channels [58], 2) mechanical manipulation exerted by external propellers [60, 83]. The former usually actuates soft robots with pressure control, volume control, or other non-mechanical actuation methods involving chemical or physical changes. The latter needs an external mechanism to directly apply a force on a fully inflated soft robot. In this section, we review the application of both methods for actuation.

1.2.2.1 Pressure control

Pressure control is one of the most widely used methods for actuation of soft pneumatic robots. This strategy imposes a prescribed constant pressure on the robot. Due to the low density and low viscosity of air, soft pneumatic robots can be quickly inflated or deflated with a large amount of air under pressure control [58, 78]. Another advantage of pressure control is that it can continuously inflate soft robots until the internal pressure of the robot reaches a target value, with no limit on the amount of air for actuation. For this reason, pressure control has been applied to soft pneumatic robots of various size from miniature actuators at millimeter scale [80, 84] to macroscale robotic arm and soft robots [59] (Figure 1-9). Pressure control, however, has two drawbacks. First, the volume change of soft pneumatic robots in pressure control depends on the compliance of the robot, which can become uncontrollable if structural instability occurs. For example, when elastic balloons and spherical shells undergo snap-through buckling subject to pressure loading, they will suddenly exhibit a large deformation that cannot be avoided by adjusting the actuation pressure [22, 23, 85, 86]. Second, pressure control cannot be easily implemented, because it needs a bulky system to generate and control the pressure for actuation.

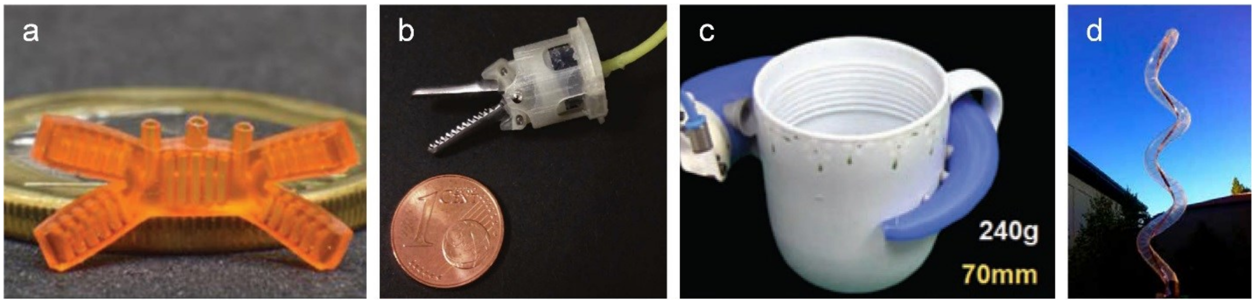

Figure 1-9 Pressure controlled soft robots. (a) A miniature multigait soft robot [80]. (b) a gripper driven by a linear elastic actuator [84]. (c) An octopus-inspired robotic arm [78]. (d) A soft robot that can grow in length [59].

An apparatus for pressure-controlled actuation typically consists of four components: the pressure source, the valve control system, the microcontroller system, and the tubing for connection. The pressure source is a device that can generate the pressure for actuation, such as air compressors [87], vacuum pumps [73, 88], and air tanks with compressed gas [22]. The valve control system is a set of valves used to regulate the air flow between the pressure source and the soft robot. For example, pressure regulators can control the pressure of the gas to the target value, and solenoid valves can provide on/off control of the flow. The operations of the valves are controlled by microcontrollers, e.g. Arduino microcontroller [74, 89]. Finally, the pressure source, the valves, and the soft robot are connected through a tubing system.

1.2.2.2 Volume control

An alternative to pressure control is volume control, a strategy typically implemented with a syringe pump that imparts the volume change to a soft pneumatic robot (Figure 1-10). The advantage of volume control over pressure control is that the former can avoid unexpected volume changes that can emerge when the motion of the robot encounters an instance of structural instability, which is common in soft robotics. For this reason, volume control is a widespread method used to characterize the pressure-volume change response of soft pneumatic robots (Figure 1-10a) [22, 68, 69]. Another advantage of volume control is that it also controls the flow rate for actuation, an outcome that can be exploited to simplify the control of soft robot [90] (Figure 1-10b). Volume control, however, has been so far not suitable to generate fast actuation because the actuation speed is limited by the maximum flow rate of the syringe pump. Only a few attempts have successfully achieved fast movements with volume control by incorporating snap-through instability of spherical caps [23] or balloons [86] into the structure of the actuators.

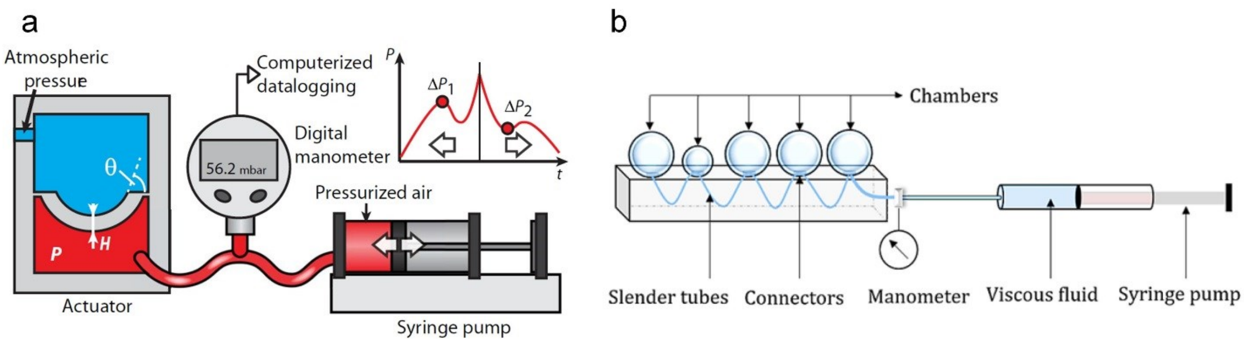

Figure 1-10 Schematic of volume controlled actuation. (a) A bistable valve characterized with a syringe pump [22] (b) Multiple fluid-driven elastic actuators controlled by a single syringe pump [90].

1.2.2.3 Non-mechanical control

Besides the aforementioned methods relying on mechanical control, strategies using non-mechanical control have also been applied for actuation of soft pneumatic robots. These can generate pressure from a diverse set of sources, such as the deformation of dielectric elastomers, the evaporation of low boiling point fluids, the chemical decomposition of monopropellants, and explosive chemical reactions. Although these methods do not require an external air compressor or a syringe pump to drive the robot, they all need an integrated system to couple the non-mechanical control with the actuation of the soft pneumatic robot. Each of them are reviewed below.

Dielectric elastomer. The first experimental observation of actuation trigger by a dielectric elastomer was reported by Roentgen [91] in 1880. A large electric field was shown able to change the shape of a film of natural rubber. The schematic is shown in Figure 1-11a. When a voltage is applied to a film of dielectric elastomer sandwiched between two compliant electrodes, the dielectric elastomer expands subject to biaxial forces in the plane parallel to its surface. In soft pneumatic robots, this phenomenon can be used to control the volume of balloon actuators [85, 92, 93]. For example, Hines et al. [92] studied an inflatable soft actuator that consists of a closed chamber and two balloons on top. The balloons are made of a dielectric elastomer with both inner and outer surfaces coated with carbon grease electrodes. When voltage is applied to the electrodes on one balloon, the dielectric elastomer of this balloon expands to increase the volume, thus causing the volume of the other balloon to decrease.

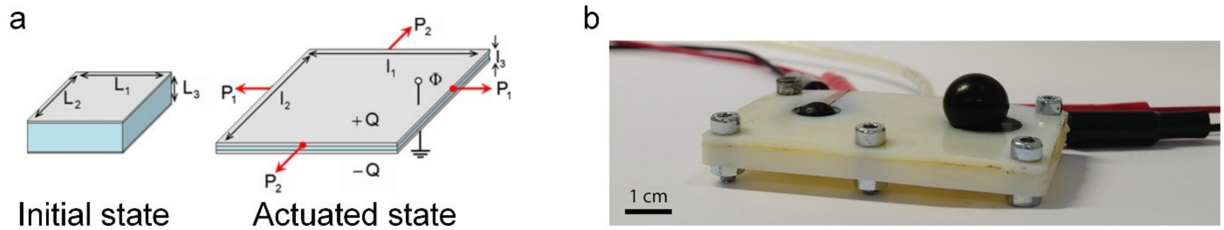

Figure 1-11 (a) Voltage-induced deformation of dielectric elastomer membrane [93] (b) A multi-membrane soft actuator made of dielectric elastomer [92]

Low boiling point fluid. Several fluids with low boiling point have been shown suitable for the actuation of soft pneumatic robots. These include ethanol, diethyl ether, acetone, Novec 7000, and dichloromethane [94]. When these fluids are heated in a sealed container, they can generate a high pressure ranging between 59 and 709 mbar. Among the options, Novec 7000 has been used in many soft robots because it has the lowest boiling point (34 ℃) and has no flash point. The flash point here means the lowest temperature at which the vapor of the fluid can be ignited. However, Garrad et al. [94] noted that Novec 7000 can diffuse through most silicone elastomers, an outcome that may limit the life span of soft actuators. Senzaki et al. [95] developed a wearable thin actuator for a portable rehabilitation device that can be silently driven by a liquid with low boiling point. Nakahara et al. [96] introduced an electric phase-change actuator that can be used to make a self-folding box and a gripper. Garrad et al. [94] demonstrated that it is easy to actuate existing soft pneumatic actuators with low-boiling point fluids by integrating a compliant heating element into the robot.

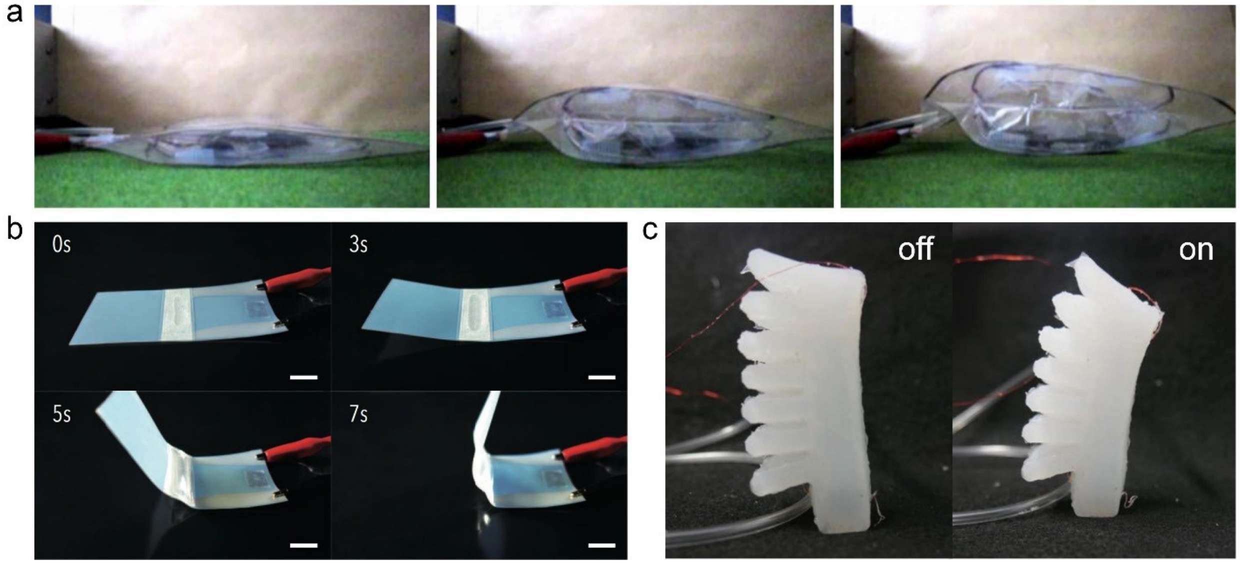

Figure 1-12 Soft actuators can be driven by low boiling point fluid to (a) increase the thickness [95], (b) rotate [96], or (c) bend [94].

Chemical decomposition. Chemical decomposition of monopropellants has been used as a pressure source for soft robots. The advantage is that this strategy does not require power from batteries or external sources. The decomposition of hydrogen peroxide has one of the highest energy density among common monopropellant fuels, following the formula of $2H_2O_2$ (l) → $2H_2O$ (l, g) + O_2 (g) [97]. At ambient pressure, the decomposition of hydrogen peroxide can provide a huge volumetric expansion of about 240 times the initial volume [98]. Wehner et al. [99] reported an octopus-like soft robot that have eight arms powered by the decomposition of hydrogen peroxide (Figure 1-13). In the reaction chamber, the decomposition is catalyzed by platinum to rapidly inflate actuators in the arm to 50 kPa with a volume expansion that is 160 times the original volume.

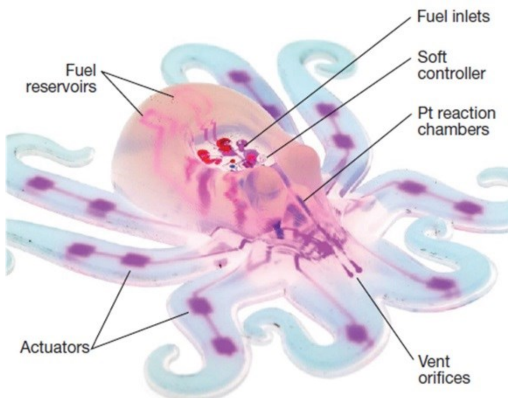

Figure 1-13 An octopus-like soft robot powered by catalyzed decomposition of hydrogen peroxide [99].

Explosive chemical reaction. Explosive chemical reactions are used in soft pneumatic robots that need extremely fast actuation speed, e.g. jumping robots (Figure 1-14). In Figure 1-14, the jumping soft robot is able to jump with the combustion of an internal mixture of butane and oxygen [100]. Common fuels for explosive combustion are hydrocarbons including methane, butane and propane, which can produce a pulse of high pressure gas for the fast motion of soft robots. Among these fuels, Loepfe et al. [101] found that propane/butane-air mixture has a slightly higher energy than methane-air mixture, while both propane and butane can release more energy when they directly react with nitrous oxide instead of air or oxygen. The combustion in soft robots is commonly triggered by an electric spark, which can be easily integrated into the robot and quickly provided with millisecond precision [102]. A limitation of using explosive chemical reactions for actuation is that the combustion products must be exhausted before the next actuation, an outcome that poses challenges for the design of the soft robot [103].

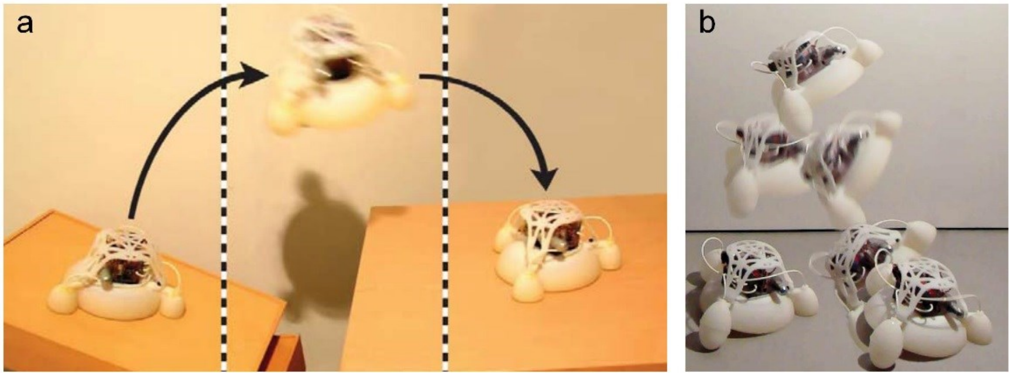

Figure 1-14 A jumping robot powered by explosive combustion [100]. (a) Jumping from an angled surface onto a table. (b) Directional jump on the ground.

1.2.2.4 Mechanical manipulation

While most soft pneumatic robots are driven by a volume change that is caused by either inflation or deflation, there are also a few exceptions. One has been demonstrated by manipulating the robot with mechanical propellers. Figure 1-15a shows the example. An untethered, inflated robotic truss that is made from thin-walled inflatable tubes and roller modules [83]. The roller modules are mounted on the tubes to separate two edges without creating a seal, and can be connected to other modules in the truss to form a node. This soft robotic truss can undergo shape change by continuously relocating the roller modules on each tube, while the volume and the total edge length of the tubes do not change. Another example is shown in Figure 1-15b, which illustrates the schematic of a soft swallowing robot composed of a soft guiding body and a rigid traction body [60]. The soft body is supported by the air that fills its internal space, with a portion of its outer wall fixed. When the inner wall is driven by the rigid traction body, the soft guiding body can swallow or spit objects.

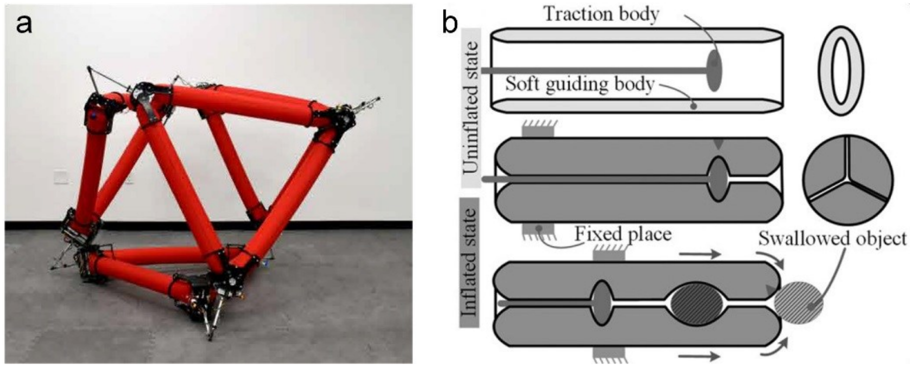

Figure 1-15 Soft robots actuated with mechanical manipulation. (a) An isoperimetric robot driven by rolloer modules [83]. (b) Schematic of a swallow robot controlled by a rigid traction body [60].

1.2.3 Soft valves

In general, soft robots need to rely on valves to control the air flow for their actuation. While hard valves are easy to use and are commercially available, their applications face three major limitations. I) They are made of rigid materials that cannot resist impact damage; II) they are relatively expensive; and III) they are difficult to miniaturize due to the challenge of scaling electromagnetic forces at small scales [104, 105]. To overcome these drawbacks, we are recently seeing research efforts devoted to the design of valves fabricated with soft materials. Shepherd et al. [102] incorporated soft check valves into a soft robot to exhaust the product gas of an explosion that powers the jumping of the robot (Figure 1-16a). Napp et al. [105] introduced a soft band-pass valve, which can shut off the flow when the flow rate exceeds a threshold value (Figure 1-16b). Actuators connected by this valve can be inflated to different levels of pressure using a single modulated pressure source. Rothemund et al. [22] proposed a soft bistable valve that can act as a pneumatic oscillator when integrated into a feedback pneumatic circuit. This valve can be driven by a single source of constant pressure that automatically controls a soft robot. An example is a soft gripper that can grasp once it touches an object (Figure 1-16c).

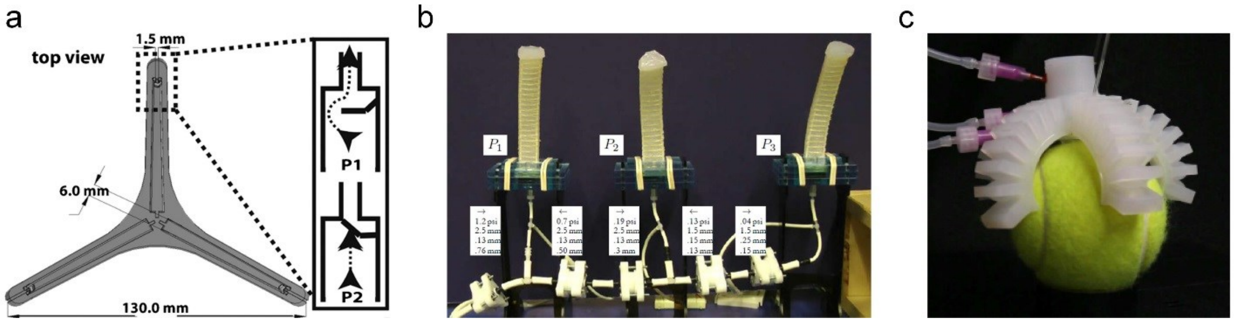

Figure 1-16 (a) A tripedal soft robot with soft check valve embedded at the ends of the legs [102]. (b) Three pneumatic actuators connected by band-pass valves [105]. (c) A gripper controlled by a bistable valve at the top [22].

Besides basic control functions achieved by a single soft valve, more intricate control logic can be implemented through soft fluidic circuits that contain multiple interacting valves. Mosadegh et al. [106] introduced a soft microfluidic circuit that consists of check valves and switch valves. This system can act as a pneumatic oscillator that translates a constant flow input into an oscillatory flow output. Wehner et al. [99] integrated this circuit into an octopus-like soft robot (Figure 1-17a) to autonomously switch the flow between the blue and red channels, with each channel controlling four legs of the robot. Preston et al. [76] described a soft oscillator that consists of a ring of three bistable valves introduced by Rothemund et al. [22]. This oscillator can generate periodic pressure signals to drive a rolling robot by sequentially inflating the balloons on the surface of the robot (Figure 1-17b). Preston et al. [107] also demonstrated that the bistable valves can act as pneumatic NOT, AND, and OR digital logic gates, which can form a toggle switch to convert human input to a binary pneumatic signal for a soft gripper (Figure 1-17c).

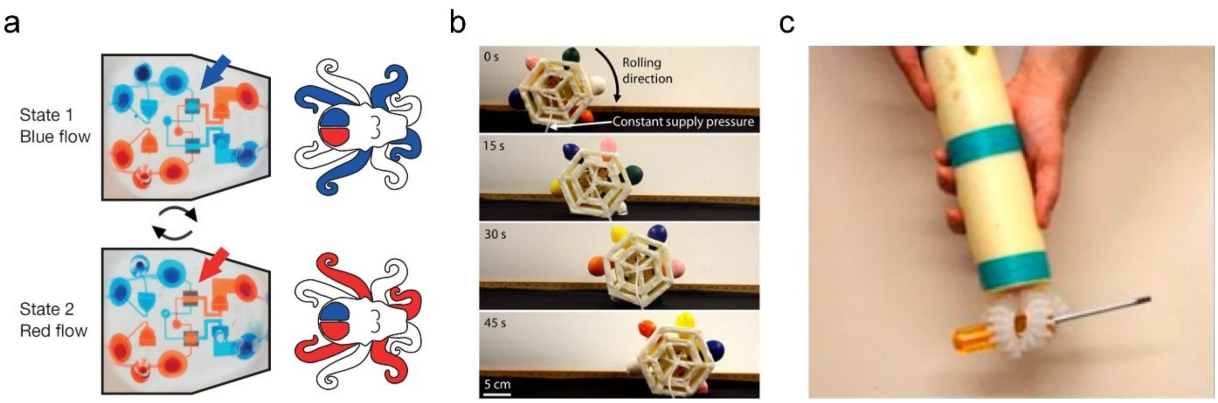

Figure 1-17 Soft robots controlled by fluidic circuits. (a) A octopus-like soft robot control [99]. (b) A rolling robot [76]. (c) A soft gripper [107].

1.2.4 Challenges on soft pneumatic robots

As discussed above, high-speed motion of soft pneumatic robot can be achieved with either pressure control, explosive chemical reactions, or elastic instability of the robot body. These methods might be difficult to implement due to the following challenges:

- Pressure control requires a bulky system of pressure supply, hard valves, and control algorithms to provide a desired pressure for actuation [58, 78].
- Chemical explosion needs a complex combustion system embedded in the body of the robot that can deliver fuel to the combustion chamber, ignite the fuel, and exhaust the product gas [102].
- The drawback of the last method is that for existing soft robots, their physical structure of the robot, i.e. its own body, needs to be designed or modified to integrate elastic instability [23, 85, 86].

These challenges highlight the need for a convenient and effective approach to enable fast motion of soft robots. A possible solution to address this issue is to use soft valves. In this context, we observe the following challenge in the literature.

- While several soft valves have demonstrated a great potential in controlling the actuation of soft pneumatic robots [22, 99], their function is mainly restricted to flow control only.

The attainment of other functions for rapid actuation, such as the capacity to use a slow volume input to generate a fast volume output, is still to explore.

1.3 Thesis objectives

The overall goal of this thesis is to contribute to the field of shell buckling and gain novel insights on shell instability that can be directly transferred to soft robotics. More specifically, this work is deployed along two complementary tracks. The first investigates the role of geometric defects on the buckling of spherical shells under external pressure, and the second exploits the lessons learned from the first to generate a novel functional response that finds direct application in pneumatic soft robots.

The specific objectives of the former are to:

- Study the effects of a large axisymmetric imperfection on the buckling response of elastic spherical shells subject to uniform external pressure, with the goal of escaping the classical bifurcation buckling that is highly unstable.
- Formulate shell buckling equations of an imperfect shell with exact expressions of the Lagrangian stretching strains and changes in curve of the shell middle surface as well as live pressure loading.
- Unveil the existence of multiple buckling modes that an imperfect shell can undergo, map the instability domains and their boundaries, and finally elucidate the competition between buckling modes.

For the latter, the specific objectives are to:

- Apply the insights for the first investigation to the design of a volume-controlled soft valve that can fast actuate soft pneumatic robots. In particular the snap-through buckling interactions of spherical shells should be leveraged to produce a fast volume output.
- Investigate the role of the soft valve constituents in producing a fast volume output and propose practical guidelines for the design of a novel soft valve for the actuation of soft robots.

- Characterize the performance of the soft valve with fabricated prototypes, and demonstrate its implementation through an illustrative application.

1.4 Structure of the thesis

This thesis is manuscript-based and consists of four chapters. Chapter 1 provides an introduction and literature review of pressurized spherical shells and soft pneumatic robots. In particular, the first part briefly introduces the background, and is followed by a systematic review of the buckling of perfect and imperfect spherical shells under uniform external pressure. The second part surveys soft pneumatic robots, including their background, their actuation methods, and soft valves for their control. The chapter concludes with the objectives and structure of the thesis.

Chapter 2 presents a systematic study on the effects of an as-designed geometric imperfection on the elastic buckling of hemispherical shells subject to uniform external pressure. A modified Euler coordinate system is employed to derive the theoretical model for the imperfect shell with the exact expressions for the stretching and bending strains as well as live pressure loading. Experiments and numerical simulations are performed to validate the theoretical model. The effects of the as-designed defect are studied by comparing the buckling behavior between the imperfect shell and a perfect one that is free from geometric imperfection. The effects of as-manufactured defects, such as thickness non-uniformity, are also discussed. In addition, a sensitivity analysis on the role of defect geometry and shell radius to thickness ratio is performed. Possible buckling modes of the imperfect shell are mapped into charts with their corresponding buckling performance.

Chapter 3 introduces a bi-shell valve for the rapid actuation of soft pneumatic robots that can harness shell snapping interaction to convert a slow volume input into a fast volume output. The pressure-volume change responses of the bi-shell valve and the constituent shells are characterized with both experiments and numerical simulations, while the role of each constituent shell in generating the volume change and energy output of the valve is investigated with theoretical analysis. The output of the valve is studied with pertinent performance metrics. Finally, a two-steps approach for the valve design is proposed, and applied to develop a bi-shell valve that can fast actuate a pneumatic striker.

Finally, Chapter 4 highlights the main results and contributions of this thesis and concludes with a brief description of possible paths for future work.

1.5 References

[1] D. L. D. Caspar and A. Klug, *Physical principles in the construction of regular viruses.* Cold Spring Harbor Symposia on Quantitative Biology, 1962. **27**: p. 1-24.

[2] J. Arfsten, S. Leupold, C. Bradtmöller, I. Kampen, and A. Kwade, *Atomic force microscopy studies on the nanomechanical properties of saccharomyces cerevisiae.* Colloids and Surfaces B: Biointerfaces, 2010. **79**(1): p. 284-290.

[3] E. Katifori, S. Alben, E. Cerda, D. R. Nelson, and J. Dumais, *Foldable structures and the natural design of pollen grains.* Proceedings of the National Academy of Sciences, 2010. **107**(17): p. 7635-7639.

[4] L. Kratochvíl and D. Frynta, *Egg shape and size allometry in geckos (squamata: Gekkota), lizards with contrasting eggshell structure: Why lay spherical eggs?* Journal of Zoological Systematics and Evolutionary Research, 2006. **44**(3): p. 217-222.

[5] X. T. Nguyen, S. Hou, T. Liu, and X. Han, *A potential natural energy absorption material – coconut mesocarp: Part a: Experimental investigations on mechanical properties.* International Journal of Mechanical Sciences, 2016. **115-116**: p. 564-573.

[6] B. Gludovatz, F. Walsh, E. A. Zimmermann, S. E. Naleway, R. O. Ritchie, and J. J. Kruzic, *Multiscale structure and damage tolerance of coconut shells.* Journal of the Mechanical Behavior of Biomedical Materials, 2017. **76**: p. 76-84.

[7] F. Lana de Terzi, *Wikipedia*. 1670. [cited 2020 Dec. 14]; Available from: https://en.wikipedia.org/wiki/Vacuum_airship#/media/File:Flying_boat.png.

[8] J. W. Snyder and A. N. Palazotto, *Design and modal analysis of a unique structure under an internal vacuum*, in *58th aiaa/asce/ahs/asc structures, structural dynamics, and materials conference*.

[9] T. T. Metlen, *Design of a lighter than air vehicle that achieves positive buoyancy in air using a vacuum*. 2013, Air Force Institute of Technology.

[10] O. v. Guericke. [cited 2020 Oct. 15]; Available from: https://en.wikipedia.org/wiki/Magdeburg_hemispheres.

[11] W. Yang, J. Yang, Y. Dong, S. Mao, Z. Gao, Z. Yue, S. J. Dillon, H. Xu, and B. Xu, *Probing buckling and post-buckling deformation of hollow amorphous carbon nanospheres: In-situ experiment and theoretical analysis.* Carbon, 2018. **137**: p. 411-418.

[12] M. Haboussi, A. Sankar, and M. Ganapathi, *Nonlinear axisymmetric dynamic buckling of functionally graded graphene reinforced porous nanocomposite spherical caps.* Mechanics of Advanced Materials and Structures, 2019: p. 1-14.

[13] J. Jose, M. Kamp, A. van Blaaderen, and A. Imhof, *Unloading and reloading colloidal microcapsules with apolar solutions by controlled and reversible buckling.* Langmuir, 2014. **30**(9): p. 2385-2393.

[14] V. S. R. Jampani, D. J. Mulder, K. R. De Sousa, A.-H. Gélébart, J. P. F. Lagerwall, and A. P. H. J. Schenning, *Micrometer-scale porous buckling shell actuators based on liquid crystal networks.* Advanced Functional Materials, 2018. **28**(31): p. 1801209.

[15] A. Evkin, M. Kolesnikov, and D. A. Prikazchikov, *Buckling of a spherical shell under external pressure and inward concentrated load: Asymptotic solution.* Mathematics and Mechanics of Solids, 2017. **22**(6): p. 1425-1437.
[16] B. B. Pan, W. C. Cui, Y. S. Shen, and T. Liu, *Further study on the ultimate strength analysis of spherical pressure hulls.* Marine Structures, 2010. **23**(4): p. 444-461.
[17] B. B. Pan, W. C. Cui, and Y. S. Shen, *Experimental verification of the new ultimate strength equation of spherical pressure hulls.* Marine Structures, 2012. **29**(1): p. 169-176.
[18] A. Khan, W. Liquan, W. Gang, M. Imran, H. M. Waqas, and A. A. Zaidi, *Concept design of the underwater manned seabed walking robot.* Journal of Marine Science and Engineering, 2019. **7**(10): p. 366.
[19] J. Błachut and K. Magnucki, *Strength, stability, and optimization of pressure vessels: Review of selected problems.* Applied Mechanics Reviews, 2008. **61**(6): p. 060801-060801-060833.
[20] X. L. Dong, Z. Y. Gao, and T. X. Yu, *Dynamic crushing of thin-walled spheres: An experimental study.* International Journal of Impact Engineering, 2008. **35**(8): p. 717-726.
[21] Y.-l. Zhang, J. Jin, H.-l. Hou, S.-y. Liu, and X.-l. Wei, *The buckling strength of plexiglass protective shield under static water pressure.* Engineering Failure Analysis, 2019. **99**: p. 169-179.
[22] P. Rothemund, A. Ainla, L. Belding, D. J. Preston, S. Kurihara, Z. Suo, and G. M. Whitesides, *A soft, bistable valve for autonomous control of soft actuators.* Science Robotics, 2018. **3**(16): p. 7986.
[23] B. Gorissen, D. Melancon, N. Vasios, M. Torbati, and K. Bertoldi, *Inflatable soft jumper inspired by shell snapping.* Science Robotics, 2020. **5**(42): p. 1967.
[24] J. W. Hutchinson, *Buckling of spherical shells revisited.* Proceedings of the Royal Society A: Mathematical, Physical and Engineering Sciences, 2016. **472**(2195): p. 20160577.
[25] B. Pan and W. Cui, *An overview of buckling and ultimate strength of spherical pressure hull under external pressure.* Marine Structures, 2010. **23**(3): p. 227-240.
[26] R. Zoelly, *Ueber ein knickungsproblem an der kugelschale*. 1915, Ph.D. thesis, ETH Zurich: Zurich, Switzerland.
[27] A. van der Neut, *De elastische stabiliteit van den dunwandigen bol*. 1932, Ph.D. thesis, Delft: The Netherlands.
[28] W. Koiter, *The nonlinear buckling problem of a complete spherical shell under uniform external pressure, parts i, ii, iii and lv.* Proc Kon Ned Akad Wet B, 1969. **72**(1): p. 40-123.
[29] A. C. Walker, *An analytical study of the rotationally symmetric non-linear buckling of a complete spherical shell under external pressure.* International Journal of Mechanical Sciences, 1968. **10**(9): p. 695-710.
[30] M. I. Zhukov and L. S. Srubshchik, *Post-buckling behavior of a closed spherical shell: Pmm vol. 35, n≗ 5, 1971, pp. 840–847.* Journal of Applied Mathematics and Mechanics, 1971. **35**(5): p. 794-802.
[31] J. M. Hill, *Critical pressures for the buckling of thick-walled spherical shells under uniform external pressure.* The Quarterly Journal of Mechanics and Applied Mathematics, 1976. **29**(2): p. 179-196.
[32] H. N. R. Wagner, C. Hühne, and S. Niemann, *Robust knockdown factors for the design of spherical shells under external pressure: Development and validation.* International Journal of Mechanical Sciences, 2018. **141**: p. 58-77.

[33] S. C. Tillman, *On the buckling behaviour of shallow spherical caps under a uniform pressure load.* International Journal of Solids and Structures, 1970. **6**(1): p. 37-52.
[34] H.-S. Tsien, *A theory for the buckling of thin shells.* Journal of the Aeronautical Sciences, 1942. **9**(10): p. 373-384.
[35] T. von Kármán and H.-S. Tsien, *The buckling of spherical shells by external pressure.* Journal of the Aeronautical Sciences, 1939. **7**(2): p. 43-50.
[36] T. von Kármán and H.-S. Tsien, *The buckling of thin cylindrical shells under axial compression.* Journal of the Aeronautical Sciences, 1941. **8**(8): p. 303-312.
[37] W. T. Koiter, *On the stability of elastic equilibrium*. 1945, Polytechnic Institute of Delft: Delft, The Netherlands. (An English translation is available as NASA Tech. Trans. F 10833, 1967.)
[38] J. W. Hutchinson and W. T. Koiter, *Postbuckling theory.* Appl Mech Rev, 1970. **23**: p. 1353-1366.
[39] A. Lee, F. López Jiménez, J. Marthelot, J. W. Hutchinson, and P. M. Reis, *The geometric role of precisely engineered imperfections on the critical buckling load of spherical elastic shells.* Journal of Applied Mechanics, 2016. **83**(11): p. 111005-111005-111011.
[40] J. W. Hutchinson, *Eml webinar overview: New developments in shell stability.* Extreme Mechanics Letters, 2020. **39**: p. 100805.
[41] W. Hutchinson John and J. M. T. Thompson, *Nonlinear buckling behaviour of spherical shells: Barriers and symmetry-breaking dimples.* Philosophical Transactions of the Royal Society A: Mathematical, Physical and Engineering Sciences, 2017. **375**(2093): p. 20160154.
[42] F. L. Jiménez, J. Marthelot, A. Lee, J. W. Hutchinson, and P. M. Reis, *Technical brief: Knockdown factor for the buckling of spherical shells containing large-amplitude geometric defects.* Journal of Applied Mechanics, 2017. **84**(3): p. 034501-034501-034504.
[43] D. Yan, M. Pezzulla, and P. M. Reis, *Buckling of pressurized spherical shells containing a through-thickness defect.* Journal of the Mechanics and Physics of Solids, 2020. **138**: p. 103923.
[44] B. Budiansky, *Buckling of clamped shallow spherical shells*. 1959, HARVARD UNIV CAMBRIDGE MA.
[45] T. Koga and N. J. Hoff, *The axisymmetric buckling of initially imperfect complete spherical shells.* International Journal of Solids and Structures, 1969. **5**(7): p. 679-697.
[46] J. Błachut, *Buckling of composite domes with localised imperfections and subjected to external pressure.* Composite Structures, 2016. **153**: p. 746-754.
[47] J. Błachut, *Locally flattened or dented domes under external pressure.* Thin-Walled Structures, 2015. **97**: p. 44-52.
[48] H. N. R. Wagner, C. Hühne, J. Zhang, W. Tang, and R. Khakimova, *Geometric imperfection and lower-bound analysis of spherical shells under external pressure.* Thin-Walled Structures, 2019. **143**: p. 106195.
[49] M. Deml and W. Wunderlich, *Direct evaluation of the 'worst' imperfection shape in shell buckling.* Computer Methods in Applied Mechanics and Engineering, 1997. **149**(1): p. 201-222.
[50] H. a. D. Abramovits, *Stability and vibrations of thin-walled composite structures*. 2017, Woodhead Publishing, an imprint of Elsevier: Duxford.

[51] G. D. Galletly and A. Muc, *Buckling of fibre-reinforced plastic-steel torispherical shells under external pressure.* Proceedings of the Institution of Mechanical Engineers, Part C: Journal of Mechanical Engineering Science, 1988. **202**(6): p. 409-420.

[52] J. Błachut and O. R. Jaiswal, *On the choice of initial geometric imperfections in externally pressurized shells.* Journal of Pressure Vessel Technology, 1999. **121**(1): p. 71-76.

[53] J. Błachut and G. D. Galletly, *Influence of local imperfections on the collapse strength of domed end closures.* Proceedings of the Institution of Mechanical Engineers, Part C: Journal of Mechanical Engineering Science, 1993. **207**(3): p. 197-207.

[54] J. Paulose and D. R. Nelson, *Buckling pathways in spherical shells with soft spots.* Soft Matter, 2013. **9**(34): p. 8227-8245.

[55] J. Zhang, Y. Wang, W. Tang, Y. Zhu, and X. Zhao, *Buckling of externally pressurised spherical caps with wall-thickness reduction.* Thin-Walled Structures, 2019. **136**: p. 129-137.

[56] N. P. Bende, A. A. Evans, S. Innes-Gold, L. A. Marin, I. Cohen, R. C. Hayward, and C. D. Santangelo, *Geometrically controlled snapping transitions in shells with curved creases.* Proceedings of the National Academy of Sciences, 2015. **112**(36): p. 11175-11180.

[57] G. M. Whitesides, *Soft robotics.* Angewandte Chemie International Edition, 2018. **57**(16): p. 4258-4273.

[58] E. Siéfert, E. Reyssat, J. Bico, and B. Roman, *Bio-inspired pneumatic shape-morphing elastomers.* Nature Materials, 2019. **18**(1): p. 24-28.

[59] E. W. Hawkes, L. H. Blumenschein, J. D. Greer, and A. M. Okamura, *A soft robot that navigates its environment through growth.* Science Robotics, 2017. **2**(8): p. eaan3028.

[60] H. Li, J. Yao, C. Liu, P. Zhou, Y. Xu, and Y. Zhao, *A bioinspired soft swallowing robot based on compliant guiding structure.* Soft Robotics, 2020. **7**: p. 491-499.

[61] P. Polygerinos, K. C. Galloway, E. Savage, M. Herman, K. O. Donnell, and C. J. Walsh. *Soft robotic glove for hand rehabilitation and task specific training*. In *2015 IEEE International Conference on Robotics and Automation (ICRA)*. 2015.

[62] J. Fang, J. Yuan, M. Wang, L. Xiao, J. Yang, Z. Lin, P. Xu, and L. Hou, *Novel accordion-inspired foldable pneumatic actuators for knee assistive devices.* Soft Robotics, 2020. **7**(1): p. 95-108.

[63] D. Rus and M. T. Tolley, *Design, fabrication and control of soft robots.* Nature, 2015. **521**(7553): p. 467-475.

[64] H. Hauser, A. J. Ijspeert, R. M. Füchslin, R. Pfeifer, and W. Maass, *Towards a theoretical foundation for morphological computation with compliant bodies.* Biological Cybernetics, 2011. **105**(5): p. 355-370.

[65] C. Paul, *Morphological computation: A basis for the analysis of morphology and control requirements.* Robotics and Autonomous Systems, 2006. **54**(8): p. 619-630.

[66] C. Laschi, B. Mazzolai, and M. Cianchetti, *Soft robotics: Technologies and systems pushing the boundaries of robot abilities.* Science Robotics, 2016. **1**(1): p. eaah3690.

[67] D. Yang, M. S. Verma, J.-H. So, B. Mosadegh, C. Keplinger, B. Lee, F. Khashai, E. Lossner, Z. Suo, and G. M. Whitesides, *Buckling pneumatic linear actuators inspired by muscle.* Advanced Materials Technologies, 2016. **1**(3): p. 1600055.

[68] B. Mosadegh, P. Polygerinos, C. Keplinger, S. Wennstedt, R. F. Shepherd, U. Gupta, J. Shim, K. Bertoldi, C. J. Walsh, and G. M. Whitesides, *Pneumatic networks for soft robotics that actuate rapidly.* Advanced Functional Materials, 2014. **24**(15): p. 2163-2170.

[69] B. Gorissen, E. Milana, A. Baeyens, E. Broeders, J. Christiaens, K. Collin, D. Reynaerts, and M. De Volder, *Hardware sequencing of inflatable nonlinear actuators for autonomous soft robots.* Advanced Materials, 2019. **31**(3): p. 1804598.

[70] M. De Volder, J. Peirs, D. Reynaerts, J. Coosemans, R. Puers, O. Smal, and B. Raucent, *Production and characterization of a hydraulic microactuator.* Journal of Micromechanics and Microengineering, 2005. **15**(7): p. S15-S21.

[71] C. Lee, M. Kim, Y. J. Kim, N. Hong, S. Ryu, H. J. Kim, and S. Kim, *Soft robot review.* International Journal of Control, Automation and Systems, 2017. **15**(1): p. 3-15.

[72] M. Calisti, G. Picardi, and C. Laschi, *Fundamentals of soft robot locomotion.* Journal of The Royal Society Interface, 2017. **14**(130): p. 20170101.

[73] L. Qin, X. Liang, H. Huang, C. K. Chui, R. C.-H. Yeow, and J. Zhu, *A versatile soft crawling robot with rapid locomotion.* Soft Robotics, 2019. **6**(4): p. 455-467.

[74] Y. Tang, Y. Chi, J. Sun, T.-H. Huang, O. H. Maghsoudi, A. Spence, J. Zhao, H. Su, and J. Yin, *Leveraging elastic instabilities for amplified performance: Spine-inspired high-speed and high-force soft robots.* Science Advances, 2020. **6**(19): p. eaaz6912.

[75] Y. Tang and J. Yin, *Design of multifunctional soft doming actuator for soft machines.* Advanced Materials Technologies, 2018. **3**(7): p. 1800069.

[76] D. J. Preston, H. J. Jiang, V. Sanchez, P. Rothemund, J. Rawson, M. P. Nemitz, W.-K. Lee, Z. Suo, C. J. Walsh, and G. M. Whitesides, *A soft ring oscillator.* Science Robotics, 2019. **4**(31): p. 5496.

[77] E. Brown, N. Rodenberg, J. Amend, A. Mozeika, E. Steltz, M. R. Zakin, H. Lipson, and H. M. Jaeger, *Universal robotic gripper based on the jamming of granular material.* Proceedings of the National Academy of Sciences, 2010. **107**(44): p. 18809-18814.

[78] Z. Xie, A. G. Domel, N. An, C. Green, Z. Gong, T. Wang, E. M. Knubben, J. C. Weaver, K. Bertoldi, and L. Wen, *Octopus arm-inspired tapered soft actuators with suckers for improved grasping.* Soft Robotics, 2019. **7**(5): p. 639-648.

[79] K. Suzumori, S. Iikura, and H. Tanaka, *Applying a flexible microactuator to robotic mechanisms.* IEEE Control Systems, 1992. **12**(1).

[80] Y.-F. Zhang, C. J.-X. Ng, Z. Chen, W. Zhang, S. Panjwani, K. Kowsari, H. Y. Yang, and Q. Ge, *Miniature pneumatic actuators for soft robots by high-resolution multimaterial 3d printing.* Advanced Materials Technologies, 2019. **4**(10): p. 1900427.

[81] E. T. Roche, R. Wohlfarth, J. T. B. Overvelde, N. V. Vasilyev, F. A. Pigula, D. J. Mooney, K. Bertoldi, and C. J. Walsh, *<p>a bioinspired soft actuated material</p>.* Advanced Materials, 2014. **26**(8): p. 1200-1206.

[82] T. Ranzani, G. Gerboni, M. Cianchetti, and A. Menciassi, *A bioinspired soft manipulator for minimally invasive surgery.* Bioinspiration & Biomimetics, 2015. **10**(3): p. 035008.

[83] N. S. Usevitch, Z. M. Hammond, M. Schwager, A. M. Okamura, E. W. Hawkes, and S. Follmer, *An untethered isoperimetric soft robot.* Science Robotics, 2020. **5**(40): p. eaaz0492.

[84] G. Gerboni, M. Brancadoro, G. Tortora, A. Diodato, M. Cianchetti, and A. Menciassi, *A novel linear elastic actuator for minimally invasive surgery: Development of a surgical gripper.* Smart Materials and Structures, 2016. **25**(10): p. 105025.

[85] R. Baumgartner, A. Kogler, J. M. Stadlbauer, C. C. Foo, R. Kaltseis, M. Baumgartner, G. Mao, C. Keplinger, S. J. A. Koh, N. Arnold, Z. Suo, M. Kaltenbrunner, and S. Bauer, *A*

lesson from plants: High-speed soft robotic actuators. Advanced Science, 2020. **7**(5): p. 1903391.
[86] J. T. B. Overvelde, T. Kloek, J. J. A. D'haen, and K. Bertoldi, *Amplifying the response of soft actuators by harnessing snap-through instabilities.* Proceedings of the National Academy of Sciences, 2015. **112**(35): p. 10863-10868.
[87] M. T. Tolley, R. F. Shepherd, B. Mosadegh, K. C. Galloway, M. Wehner, M. Karpelson, R. J. Wood, and G. M. Whitesides, *A resilient, untethered soft robot.* Soft Robotics, 2014. **1**(3): p. 213-223.
[88] L. Yao, R. Niiyama, J. Ou, S. Follmer, C. D. Silva, and H. Ishii, *Pneui: Pneumatically actuated soft composite materials for shape changing interfaces*, in *Proceedings of the 26th annual ACM symposium on User interface software and technology*. 2013, Association for Computing Machinery: St. Andrews, Scotland, United Kingdom. p. 13–22.
[89] N. Vasios, A. J. Gross, S. Soifer, J. T. B. Overvelde, and K. Bertoldi, *Harnessing viscous flow to simplify the actuation of fluidic soft robots.* Soft Robotics, 2019. **7**(1): p. 1-9.
[90] E. Ben-Haim, L. Salem, Y. Or, and A. D. Gat, *Single-input control of multiple fluid-driven elastic actuators via interaction between bistability and viscosity.* Soft Robotics, 2019. **7**(2): p. 259-265.
[91] W. Roentgen, *About the changes in shape and volume of dielectrics caused by electricity.* Annual Physics and Chemistry Series, 1880. **11**: p. 771-786.
[92] L. Hines, K. Petersen, and M. Sitti, *Inflated soft actuators with reversible stable deformations.* Advanced Materials, 2016. **28**(19): p. 3690-3696.
[93] T. Li, C. Keplinger, R. Baumgartner, S. Bauer, W. Yang, and Z. Suo, *Giant voltage-induced deformation in dielectric elastomers near the verge of snap-through instability.* Journal of the Mechanics and Physics of Solids, 2013. **61**(2): p. 611-628.
[94] M. Garrad, G. Soter, A. T. Conn, H. Hauser, and J. Rossiter. *Driving soft robots with low-boiling point fluids*. In *2019 2nd IEEE International Conference on Soft Robotics (RoboSoft)*. 2019.
[95] S. Senzaki, T. Akagi, S. Dohta, and Y. Fujiwara, *Development and analysis of flexible thin actuator with a built-in fluid pressure source.* MATEC Web of Conferences, 2016. **51**: p. 02005.
[96] K. Nakahara, K. Narumi, R. Niiyama, and Y. Kawahara. *Electric phase-change actuator with inkjet printed flexible circuit for printable and integrated robot prototyping*. In *2017 IEEE International Conference on Robotics and Automation (ICRA)*. 2017.
[97] C. D. Onal, X. Chen, G. M. Whitesides, and D. Rus, *Soft mobile robots with on-board chemical pressure generation*, in *Robotics research : The 15th international symposium isrr*, H.I. Christensen and O. Khatib, Editors. 2017, Springer International Publishing: Cham. p. 525-540.
[98] M. Wehner, M. T. Tolley, Y. Mengüç, Y.-L. Park, A. Mozeika, Y. Ding, C. Onal, R. F. Shepherd, G. M. Whitesides, and R. J. Wood, *Pneumatic energy sources for autonomous and wearable soft robotics.* Soft Robotics, 2014. **1**(4): p. 263-274.
[99] M. Wehner, R. L. Truby, D. J. Fitzgerald, B. Mosadegh, G. M. Whitesides, J. A. Lewis, and R. J. Wood, *An integrated design and fabrication strategy for entirely soft, autonomous robots.* Nature, 2016. **536**(7617): p. 451-455.

[100] N. W. Bartlett, M. T. Tolley, J. T. B. Overvelde, J. C. Weaver, B. Mosadegh, K. Bertoldi, G. M. Whitesides, and R. J. Wood, *A 3d-printed, functionally graded soft robot powered by combustion.* Science, 2015. **349**(6244): p. 161-165.

[101] M. Loepfe, C. M. Schumacher, U. B. Lustenberger, and W. J. Stark, *An untethered, jumping roly-poly soft robot driven by combustion.* Soft Robotics, 2015. **2**(1): p. 33-41.

[102] R. F. Shepherd, A. A. Stokes, J. Freake, J. Barber, P. W. Snyder, A. D. Mazzeo, L. Cademartiri, S. A. Morin, and G. M. Whitesides, *Using explosions to power a soft robot.* Angewandte Chemie International Edition, 2013. **52**(10): p. 2892-2896.

[103] M. T. Tolley, R. F. Shepherd, M. Karpelson, N. W. Bartlett, K. C. Galloway, M. Wehner, R. Nunes, G. M. Whitesides, and R. J. Wood. *An untethered jumping soft robot*. In *2014 IEEE/RSJ International Conference on Intelligent Robots and Systems*. 2014.

[104] S. M. Spearing, *Materials issues in microelectromechanical systems (mems).* Acta Materialia, 2000. **48**(1): p. 179-196.

[105] N. Napp, B. Araki, M. T. Tolley, R. Nagpal, and R. J. Wood. *Simple passive valves for addressable pneumatic actuation*. In *2014 IEEE International Conference on Robotics and Automation (ICRA)*. 2014.

[106] B. Mosadegh, C.-H. Kuo, Y.-C. Tung, Y.-s. Torisawa, T. Bersano-Begey, H. Tavana, and S. Takayama, *Integrated elastomeric components for autonomous regulation of sequential and oscillatory flow switching in microfluidic devices.* Nature Physics, 2010. **6**(6): p. 433-437.

[107] D. J. Preston, P. Rothemund, H. J. Jiang, M. P. Nemitz, J. Rawson, Z. Suo, and G. M. Whitesides, *Digital logic for soft devices.* Proceedings of the National Academy of Sciences, 2019. **116**(16): p. 7750-7759.

Chapter 2

Elastic thin shells with large axisymmetric imperfection: From bifurcation to snap-through buckling

Chapter 2: Elastic thin shells with large axisymmetric imperfection: From bifurcation to snap-through buckling

*Chuan Qiao, Lu Liu, Damiano Pasini**

Department of Mechanical Engineering, McGill University, Montreal, Quebec H3A 0C3, Canada

Journal of the Mechanics and Physics of Solids, 2020. 141: 103959.

2.1 Abstract

Elastic thin shells are well-known for their highly unstable post-buckling, a response that exhausts their pressure bearing capacity and leads to catastrophic collapse. This paper examines elastic thin shells with a large axisymmetric imperfection that can escape the classical bifurcation of perfect spherical shells. We employ a shell theory formulation with exact expressions of the middle surface strains, curvature changes, and live pressure along with validating experiments and numerical simulations. The results show that a large axisymmetric imperfection in the form of a circular arc can induce snap-through buckling followed by a stable post-buckling that offers increasing resistance to pressure over a large change in volume. In addition, a sensitivity analysis on the role of defect geometry and shell radius to thickness ratio reveals the emergence of four buckling modes. For small imperfections, bifurcation buckling (mode 1) is dominant and resembles the typical dimple-like mode of perfect spherical shells. For larger imperfections, the shell attains the maximum pressure at the snap-through buckling where strain localization appears either within the imperfection (mode 2) or just below (mode 3). In the fourth mode, snap-through buckling precedes the attainment of the maximum pressure following a post-buckling path characterized by a large change of volume that makes the shell harder and stronger. These findings show that harnessing defect geometry and shell radius to thickness ratio can be effective in programming the post-buckling characteristics and transition between buckling modes, thus offering potential routes for the design of soft metamaterials with application to soft robotics and other sectors.

Keywords: spherical shells, snap-through, buckling, geometric imperfections, soft metamaterials.

2.2 Introduction

Spherical thin shells are ubiquitous in nature from the cell wall of baker's yeast [1], virus shells [2], to pollen grains [3], and coconut shells [4]. They are also widespread in engineering across the spectrum of length scale, from microcapsules for drug delivery [5], to pressure vessels [6], and underwater pressure hulls [7, 8]. The mechanics of spherical thin shells, in particular their nonlinear buckling behaviour, has been extensively studied over the past decades. One of the main findings is that under a uniformly applied external pressure, spherical thin shells exhibit a highly unstable post-buckling response characterized by a sudden drop of load bearing capacity and a strong sensitivity to imperfections. In his seminal work, Zoelly [9] was the first to study defect-free shells through classical linear theory and to derive expressions for the theoretical pressure at which buckling occurs. These predictions offer a buckling load baseline that substantially departs from experimental measures, which typically reach only 1/5 of their theoretical values. This discrepancy is conveniently gauged by the knockdown factor, the ratio of the experimentally measured buckling pressure over its theoretical counterpart, which is commonly used for shell design, and for as-built shells it has a wide span from 0.05 to 1.1 [10-18].

The causes for the low tested values of buckling pressure have been extensively studied for spherical shells [19-21]. Among the first were von Kármán and Tsien [22, 1941], who proposed the notion of a "lower buckling pressure" to indicate the minimum load necessary to keep the shell in the buckled shape. This pressure was arguably supposed to be independent of the load arrangement and the initial imperfections of the shell. Only thereafter, the issue was elucidated by Koiter [24] with his theory of elastic stability under conservative loadings, corroborated later via experiments [15]. From this theory the critical role of geometric imperfections has been unveiled with results showing the high sensitivity of both the critical load and the initial post-buckling behavior to geometric defects, even when these are very small in amplitude.

Geometric imperfections induced by fabrication are typically distributed randomly in a real shell. Since their geometry and size are not always easily quantifiable, a practical approach to obtain at most a qualitative account of the real shell response is to intentionally introduce as-designed imperfections in their ideal geometry. This approach has been widely adopted in the literature of thin shells. For example, Koga and Hoff [25] were among the first to study the role of imperfections introduced in the form of increased-radius and dimple geometries. Their investigation shed light into the role of a number of geometric defects including defect amplitude, angular width and radius to thickness ratio of the shell. Asymmetric pie-shaped imperfections in spherical caps were also studied [26] through a strain-displacement formulation similar to that of Donnell's cylindrical shell theory [27, 28]. The computational results shows a buckling pressure lower than those previously found [29]. Imperfections in the form of Legendre polynomials [30] were also later studied with the goal of assessing the post-buckling behavior and the sensitivity to defect size. More recently Błachut [31-33] performed a series of studies on the buckling of geometrically imperfect domes embedding a set of defects defined by Legendre polynomials, localized flattening, eigenmode imperfections, local inward dimple of arbitrary shape, and force-induced inward dimple. A direct relationship was established by Lee et al. [34] between the experimental buckling pressure and a set of imperfections with varying geometry. The results reveal that defect sensitivity diminishes with the amplitude of the imperfection reaching a threshold value (larger than the shell thickness), above which the knockdown factor of the buckling pressure levels out on a plateau.

Most of the existing works on defect sensitivity of shell buckling have so far studied the post buckling regime, i.e. a monotonic drop of pressure which rapidly exhausts the shell resistance until sudden collapse occurs. This phenomenon deprives shell functionality and has two main features. First, prior to bifurcation, the shell deformation, in particular the displacement of the pole, is tiny compared to the shell radius, thereby yielding almost no change in volume [35]. Second, under a given pressure the shell is unstable for the entire post-buckling regime [35], showing the inability to resist any increase in pressure and spontaneous marching towards full eversion.

In this work, we examine an elastic thin shell shaped with a large axisymmetric imperfection that can bypass the catastrophic collapse typically observed in hemispherical shells under external pressure. While previous works aiming at tuning the post-buckling characteristics of thin shells examine certain types of imperfections, such as soft spots [36] and creases [37], here we explore an alternative route. More specifically, we introduce a parametric set of geometric imperfections

(Section 2.3) that can alter the post-buckling response from a pure monotonic fall of pressure to a stable response with pressure resistance gained through large volumetric deformation. Experiments on proof-of-concepts shells (Section 2.4.1), theoretical analysis (Section 2.4.2), and finite element method (FEM) simulations (Section 2.4.3) are presented to show a buckling response over a large volume change (above 20% the initial volume), a behaviour previously unobserved in the literature of hemispherical thin shells. Finally, a sensitivity study (section 2.5) unveils a direct relation between shell response, defect characteristics and shell geometry, which altogether can be tuned to render three distinct snap-through modes besides bifurcation buckling, which can be exploited for the design of soft metamaterials for soft robotics, mechanism-based structures and smart actuators.

2.3 Shell geometry with large geometric imperfection

We consider a hemispherical thin shell (Figure 2-1) with a large geometric imperfection in the form of an axisymmetric circular-arc indentation that can vary in amplitude, angular width and location. The cross-section of the shell is defined by the radius R and thickness t, defining its slenderness, R/t. The large imperfection traces a circular arc with center O_2 and extent defined by h/l, i.e. the amplitude h to width l ratio, and the angular width θ_w. We examine the cases where the imperfection can vary in angular width θ_w (Figure 2-1c), in position through the meridional angle θ_m (Figure 2-1d), defining the position of its center O_2, and in amplitude h/l from 0 and 0.5 (Figure 2-1e), the former describing the case of an arc collapsed to a line segment, and the latter being a defect in the form of a semicircle. The imperfection is also assumed to lie between the equator and the upper pole of the semi circumference (Figure 2-1e), hence satisfying the constraint on the meridional angle θ_m and the angular width θ_w:

$$\frac{\theta_w}{2} < \theta_m < \frac{\pi}{2} - \frac{\theta_w}{2} \tag{2-1}$$

Figure 2-1f shows two special cases for extremely large imperfections with width $\theta_w = \pi / 2$ and meridional angle $\theta_m = \pi / 4$. The hemispherical shell degenerates into either a cone for amplitude

$h/l=0$, or for $h/l=\left(\sqrt{2}\text{-}1\right)/2$ into a surface of revolution obtained by rotating the generatrix, a concave arc, around the vertical axis.

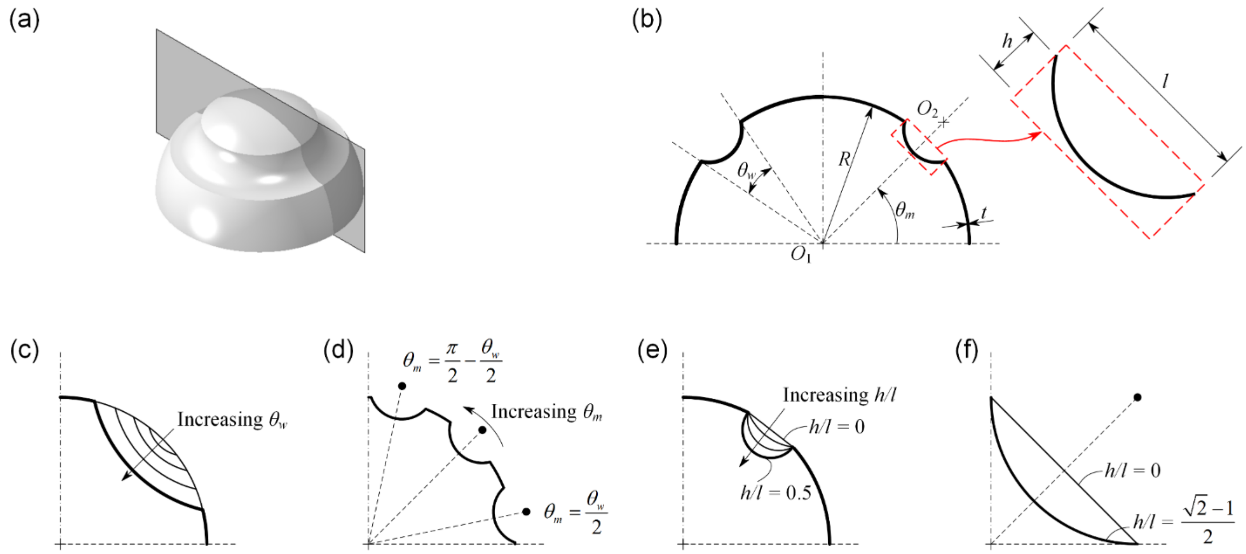

Figure 2-1 (a) Three-dimensional view with an intersecting symmetry plane of a shell with a large geometric imperfection. (b) Shell cross-section on the intersecting plane, with shell geometry described by radius R, radius to thickness ratio R/t, imperfection angular width θ_w, imperfection amplitude h/l, and meridional angle θ_w. Effect of varying defect size and location: (c) increase of defect width through change of θ_w, (d) defect center location through variation of meridional angle, θ_w, (e) defect amplitude for increasing h/l. (f) Special cases: $h/l=0$ yields a linear profile generating a conical shell, $h/l=(\sqrt{2}-1)/2$ gives a concave profile, i.e. an arc generatrix for a surface of revolution that departs from the spherical and conical geometry.

2.4 Methods

2.4.1 Experiment

2.4.1.1 Manufacturing of elastic thin shells and shell geometry assessment

Figure 2-2 shows the basic steps of the manufacturing process adapted from the literature [34, 38] to build shell samples with thin hemispherical smooth geometry. We first used fused deposition modeling (FDM) to 3D print a 1 mm-thick mold (Figure 2-2a) made of Onyx filament, and then poured a silicone-based elastomer solution onto its surface to form a thin shell. Table 2-1 lists the nominal surface geometry of the as-designed mold, which slightly differs from that of the as-built mold. Measures of the radius made with a digital caliper at the equator of the hemisphere provided R = 24.72 mm, a value 1% below from the nominal one.

For the shell material, we chose Vinylpolysiloxane (VPS, Elite Double 32, Zhermark), whose Young's modulus and Poisson's ratio (Table 2-2) were previously measured [39]. After mixing catalyst and base with equal volume fraction, VPS was poured on the surface of the 3d printed mold (Figure 2-2b). During the pouring process, excessive liquid accumulated at the bottom of the mold and formed a band of 2 mm thickness, which acted as clamp at the low boundary of the hemispherical shell. After the complete VPS stabilization at room temperature, the thin shell was peeled off the mold (Figure 2-2c).

The protocol above was followed to manufacture eight samples of identical geometry, and Figure 2-3a shows the cross-section of a representative along the symmetry plane. From a detailed assessment of the shell thickness across the entire shell domain (Figure 2-2c), we observe thickness uniformity along the circumferential direction only. In contrast, along the meridional direction major divergences appear. This is evident in Figure 2-3a, where the inner and outer profiles (red) are fitted with two splines (NURBS). From a top to bottom inspection, we notice the VPS pouring onto the mold surface resulted in two sets of local non-uniform thickening: one above the large imperfection and the other of larger amplitude at its bottom. The distance between the inner and outer profiles (red curve in Figure 2-3a) were assessed at 196 points along the arc length direction, and the thickness profile was adjusted by comparing the maximum thickness obtained from the optical image to the measurement from the digital caliperFigure 2-3b plots the scaled thickness profile as a function of the normalized arc length from the upper pole to the equator. The maximum thickness of the eight samples is $t = 0.88 \pm 0.03$ mm. The thickness profile is relatively uniform with $t = 0.20$ mm and minor fluctuations of 0.07 mm along the normalized arc length, except for peaks appearing at $s/s_0 = 0.36$ and 0.68, which respectively correspond to maximum thickness values of $t = 0.61$ mm and $t = 0.88$ mm.

Figure 2-2 Fabrication steps. (a) 3D printed hemispherical shape mold with axisymmetric circular-arc indentation. A groove at the bottom of the mold is introduced to collect excessive polymer deposition. (b) VPS liquid poured onto the mold surface. (c) Stablized shell sample removed from the mold.

R (mm)	θ_w (°)	h/l	θ_m (°)
24.86	25.2	0.2	43.3

Table 2-1. Nominal geometry of the 3D printed mold.

Linear elastic model		Neo-Hookean model	
E (MPa)	υ	C10 (MPa)	D1 (MPa^{-1})
0.96	0.5	0.16	0

Table 2-2. Measured elastic properties of VPS [39] and computed coefficients of the neo-Hookean model.

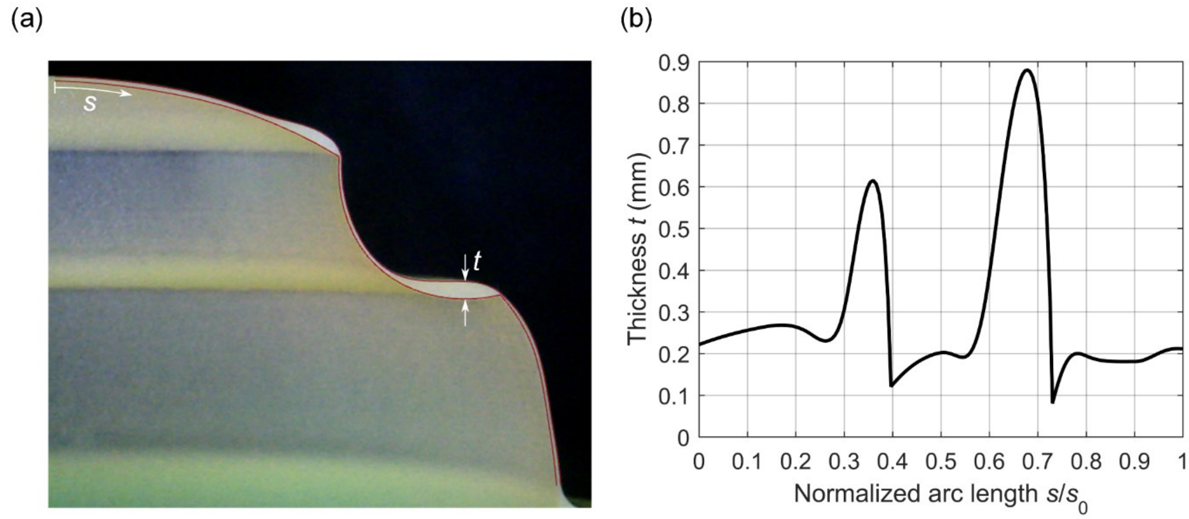

Figure 2-3 (a) Photograph of half cross-section of a representative sample cut along the symmetry plane. Red curves trace lower and upper boundaries of shell surfaces. (b) Shell thickness, t, variation traced from (a) and plotted against the normalized arc length s from pole to equator, where s_0 is the total arc length from the upper pole to the equator. The thickness profile is relatively uniform at about 0.2 mm, with peaks of $t = 0.61$ mm at $s / s_0 = 0.36$ and $t = 0.88$ mm at $s / s_0 = 0.68$.

2.4.1.2 Experimental apparatus

To reduce the volume enclosed by the thin shell and monitor the pressure evolution acting on it, we assembled the experimental setup shown in Figure 2-4. Its main components include a polypropylene syringe to extract the air inside the shell at a controlled flow rate, a Bose ElectroForce 3510 tester (Bose Corporation, Framingham, Massachusetts) used to impart a displacement load on the piston of the syringe, an acrylic fixture to constrain any sample movement, along with a pressure sensor (SM9333, SMI, California) and a microcontroller (Arduino UNO, Arduino, Italy). The thin elastic shell was mounted on an acrylic fixture, which consists of two supporting plates. The upper round plate had a circular hole at the center, with radius slightly larger than the radius of the hemispherical shell R. The thick band at the bottom of the shell was clamped between the acrylic plates, whereas the hemispherical part of the thin shell was allowed to freely deform without entering in contact with the fixture. The upper plate was tightly fastened to the lower acrylic plate with six equally spaced screws to prevent any leakage of air. The lower square plate was connected to the syringe and the pressure sensor. The syringe extracted air from the shell at a constant flow of 54 ml/s rate and was pulled by the Bose ElectroForce 3510 tester with displacement control at a constant speed. The sensor had a calibrated pressure range from −125 Pa to 125 Pa and a typical accuracy of ±0.5% of the full pressure span, which is ±1.25 Pa. The pressure sensor was controlled by the microcontroller, which was programmed to read the pressure data from the sensor at a frequency of 20Hz.

The testing results from our experiments converged at a flow rate of 54 ml/s (Table 2-3). When the flow rate was decreased further, the variations in the snap-through pressure and the maximum pressure were below 0.33 Pa and 0.63 Pa, values below the accuracy of the sensor (±1.25 Pa).

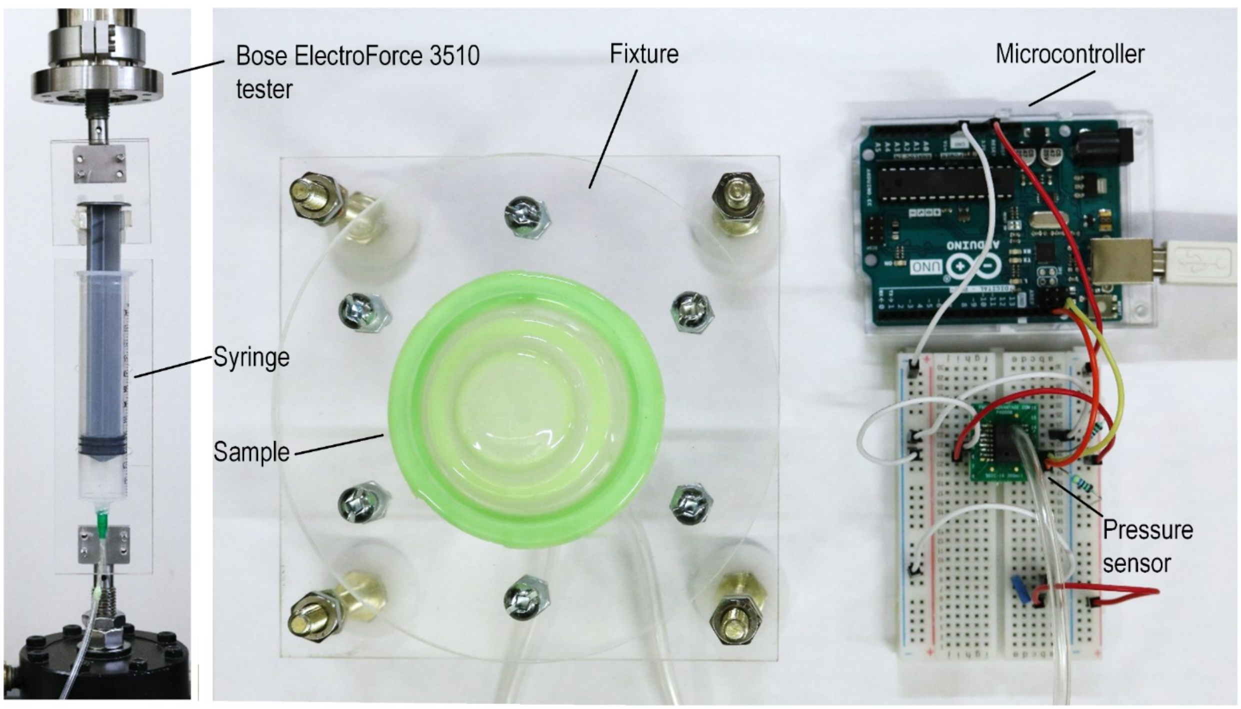

Figure 2-4 Experimental setup: the shell sample is mounted on the basal fixture and connected with two hollow rubber tubes, one to the syringe and the other to the pressure sensor. The syringe is pulled by the Bose ElectroForce 3510 tester to extract air at a constant flow rate of 54 ml/s. A microcontroller regulates the operation of the pressure sensor which measures the internal pressure of the shell.

Flow rate (ml/s)	13	27	54	108	215
Snap through pressure (Pa)	13.55	13.64	13.88	13.82	14.03
Maximum pressure (Pa)	32.05	32.32	32.68	33.38	33.15

Table 2-3. Convergence of flow rate.

2.4.2 Theoretical model

A number of formulations exist in the literature for predicting the buckling pressure of elastic thin shells. Among them for shells undergoing small strains of the middle surface and moderate rotations, approximate expressions of the stretching and bending strains, e.g. the small strain-moderate rotation theory [35] and the Donnell–Mushtari–Vlasov (DMV) theory [35, 40-43], can be used to predict buckling pressure. These theories are accurate for perfect spherical shells, but their precision degrades for shells with relatively large displacements and rotations [35]. Because the shells examined in this work experience large displacements and rotations, we use exact expressions of the Lagrangian stretching strains and changes in curvature as well as live pressure, i.e. the force per current area acting normal to the deformed middle surface, and compute the potential energy of the pressure. We assume the constitutive relation to be linear due to the small strains involved, and present a formulation that enables us to write the shell buckling equations without any restrictions on the magnitude of displacements and rotations [35, 44]. Furthermore, we follow the tensor analysis given by Niordson [44] as well as Koiter and van der Heijden [45] (see Appendix 2.8.2) to derive the nonlinear buckling equations of the middle surface for axisymmetric deformations. The following section presents first the theory for spherical shells with perfect geometry, while Section 2.4.2.2 provides the formulation for shells with large imperfection. Appendix C reports the numerical method used to obtain the solutions.

2.4.2.1 Shell theory for axisymmetric deformations of a spherical shell

Figure 2-5a shows the Euler coordinates $(\theta,\ \omega,\ r)$ for a perfect spherical shell. θ is the meridional angle, ω is the circumferential angle (not shown), and r is the distance from the origin O_1. The meridional angle θ is measured from the equator ($\theta = 0$) to the upper pole ($\theta = \pi/2$). R is the radius of the shell and $(\theta,\ \omega,\ R)$ represents the coordinates of a material point on the middle surface of the shell. For the deformed shell, the location of a material point on the middle surface is

$$\bar{\mathbf{r}} = u_\theta \mathbf{i}_\theta + u_\omega \mathbf{i}_\omega + (R + w)\mathbf{i}_r \tag{2-2}$$

where $(u_\theta,\ u_\omega,\ w)$ are the displacements tangent and normal to the undeformed middle surface, and $(\mathbf{i}_\theta, \mathbf{i}_\omega, \mathbf{i}_r)$ are the corresponding unit vectors. For axisymmetric deformations, the circumferential displacement is null ($u_\omega = 0$), and the other two displacements, u_θ and w, are independent of the circumferential angle ω.

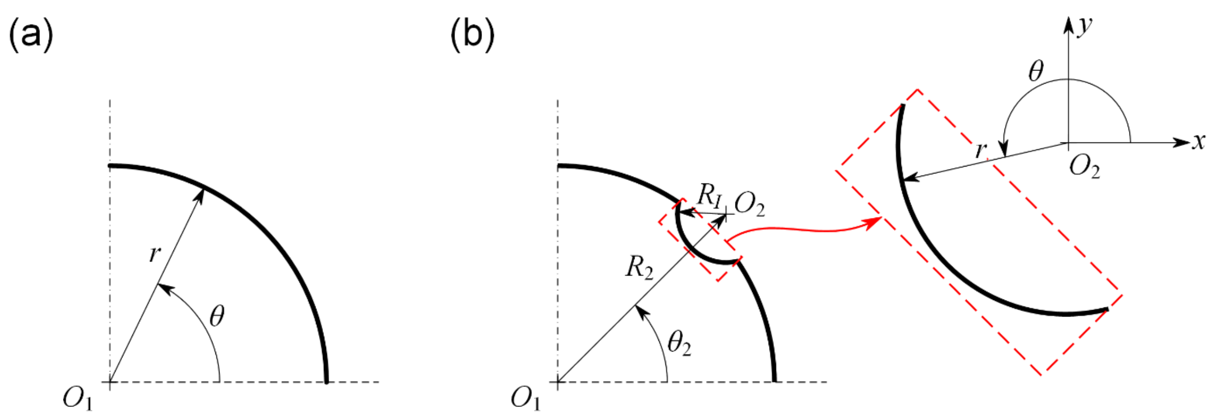

Figure 2-5 Definition of coordinates θ and r: (a) Euler coordinate system (θ, ω, r) for a spherical shell; (b) modified Euler coordinate system (θ, ω, r) for shell with large imperfection. The thick line refers to the shell middle surface.

The nonlinear middle surface strains and the change in curvature of the middle surface are functions of the linear components of both strains $(e_{\theta\theta},\ e_{\omega\omega},\ e_{\theta\omega})$ and rotations $(\varphi_\theta,\ \varphi_\omega,\ \varphi_r)$, the former given by

$$
\begin{aligned}
e_{\theta\theta} &= \frac{1}{R}\left(\frac{\partial u_\theta}{\partial \theta} + w\right) \\
e_{\omega\omega} &= \frac{1}{R}\left(\frac{1}{\cos\theta}\frac{\partial u_\omega}{\partial \omega} - \tan\theta u_\theta + w\right) \\
e_{\theta\omega} &= \frac{1}{2R}\left(\frac{\partial u_\omega}{\partial \theta} + \frac{1}{\cos\theta}\frac{\partial u_\theta}{\partial \omega} + \tan\theta u_\omega\right)
\end{aligned}
\tag{2-3}
$$

where the circumferential displacement u_ω and the partial derivatives with respect to the circumferential angle ω in $e_{\omega\omega}$ and $e_{\theta\omega}$ equal to zero for axisymmetric deformations, On the other hand, the latter, i.e. the linear rotations about the tangents and the normal to the middle surface are:

$$
\begin{aligned}
\varphi_\theta &= \frac{1}{R}\left(\frac{\partial w}{\partial \theta} - u_\theta\right) \\
\varphi_\omega &= \frac{1}{R}\left(\frac{1}{\cos\theta}\frac{\partial w}{\partial \omega} - u_\omega\right) \\
\varphi_r &= \frac{1}{2R}\left(\frac{\partial u_\omega}{\partial \theta} - \frac{1}{\cos\theta}\frac{\partial u_\theta}{\partial \omega} - \tan\theta u_\omega\right)
\end{aligned}
\tag{2-4}
$$

For axisymmetric deformations, the non-vanishing components of the nonlinear middle surface strains and bending strains are given by

$$
\begin{aligned}
E_{\theta\theta} &= e_{\theta\theta} + \frac{1}{2}e_{\theta\theta}^2 + \frac{1}{2}\varphi_\theta^2 \\
E_{\omega\omega} &= e_{\omega\omega} + \frac{1}{2}e_{\omega\omega}^2
\end{aligned}
\tag{2-5}
$$

and

$$
\begin{aligned}
K_{\theta\theta} &= \frac{1}{R}\left[\left(1+e_{\theta\theta}+e_{\omega\omega}+e_{\omega\omega}e_{\theta\theta}\right)\left(-1+\frac{\partial\varphi_\theta}{\partial\theta}-e_{\theta\theta}\right)-\varphi_\theta\left(1+e_{\omega\omega}\right)\left(\frac{\partial e_{\theta\theta}}{\partial\theta}+\varphi_\theta\right)+1\right] \\
K_{\omega\omega} &= \frac{1}{R}\left[\left(1+e_{\theta\theta}+e_{\omega\omega}+e_{\omega\omega}e_{\theta\theta}\right)\left(-1-\tan\theta\varphi_\theta-e_{\omega\omega}\right)+\tan\theta\varphi_\theta\left(1+e_{\omega\omega}\right)\left(e_{\theta\theta}-e_{\omega\omega}\right)+1\right]
\end{aligned}
\tag{2-6}
$$

We note that in Eqs. (2-4) and (2-6), the sign of both rotation and change in curvature is opposite to that of previous works [34, 35, 40, 43], because here the definition of rotation and curvature change follow that of Niordson [44]. For axisymmetric deformations, the last two terms in Eq. (2-4) vanish, i.e. $\varphi_\omega = 0$ and $\varphi_r = 0$.

The resultant membrane stresses $\left(N_{\theta\theta}, N_{\omega\omega}, N_{\theta\omega}\right)$ and the bending moments $\left(M_{\theta\theta}, M_{\omega\omega}, M_{\theta\omega}\right)$ for a shell with isotropic linear elastic material are

$$
\mathrm{PE} = p\Delta V \quad
\begin{aligned}
N_{\alpha\beta} &= \frac{Et}{\left(1-v^2\right)}\left[(1-v)E_{\alpha\beta} + vE_{\gamma\gamma}\delta_{\alpha\beta}\right] \\
M_{\alpha\beta} &= D\left[(1-v)K_{\alpha\beta} + vK_{\gamma\gamma}\delta_{\alpha\beta}\right]
\end{aligned}
\tag{2-7}
$$

where E is the Young's modulus, t is the shell thickness, v is the Poisson's ratio, and

$D = Et^3/[12(1-\nu^2)]$ is the bending stiffness. The subscripts in Eq. (2-7) take on values 1 or 2, and the Einstein summation convention applies. The non-vanishing components in the membrane stress and bending moments are $(N_{\theta\theta},\, N_{\omega\omega})$ and $(M_{\theta\theta},\, M_{\omega\omega})$.

The sum of the stretching and bending energy gives the elastic strain energy (SE) expressed as:

$$\mathrm{SE}(u_\theta, w) = \frac{1}{2}\int_S \left(M_{\alpha\beta}K_{\alpha\beta} + N_{\alpha\beta}E_{\alpha\beta}\right)\mathrm{d}S \tag{2-8}$$

where S is the area of the perfect spherical surface in its undeformed state (Figure 2-5a).

The potential energy of the uniform external pressure is

$$\mathrm{PE} = p\Delta V \tag{2-9}$$

where ΔV is the volume change. For small deformations, the volume change can be approximated with the pressure acting on the initial middle surface in the direction normal to the initial middle surface, namely the dead pressure:

$$\Delta V(u_\theta, w) = \int_S w\mathrm{d}S \tag{2-10}$$

For large axisymmetric deformations, the volume change ΔV is obtained with the pressure acting on the deformed middle surface in the direction normal to the deformed middle surface, i.e. the live pressure, whose exact expression is here derived as:

$$\Delta V(u_\theta, w) = \int_S \left\{ w + \frac{1}{2}\left[w\left(e_{\theta\theta} + e_{\omega\omega}\right) - \varphi_\theta u_\theta\right] + \frac{1}{3}\left(we_{\theta\theta}e_{\omega\omega} - e_{\omega\omega}\varphi_\theta u_\theta\right)\right\}\mathrm{d}S \tag{2-11}$$

Eq. (2-11) contains both the linear term, i.e. dead pressure, and the products of displacements, rotations and strains. While the former term only is sufficient to study the buckling pressure of perfect spherical shells [34, 35], the latter cannot be neglected for a shell with pole displacement comparable to its radius, which experiences large nonlinear deformation, as is the case of the shell examined here.

The total potential energy Ψ of the spherical shell is given by the sum of the elastic strain energy SE and the potential energy PE of the external pressure

$$\Psi\left(u_\theta, w\right) = \mathrm{SE} + \mathrm{PE} \tag{2-12}$$

2.4.2.2 Imperfect shell theory for axisymmetric deformations

To account for the large geometric imperfection (axisymmetric circular-arc), we introduce the modified Euler coordinates $(\theta,\ \omega,\ r)$ shown in Figure 2-5b. Here, the difference from the Euler coordinate system (Figure 2-5a) pertains to the coordinates θ and r, which are defined with respect to the center of the imperfection O_2, rather than the origin of the Euler coordinate system O_1. Following the geometry parameters introduced in Section 2.3, the coordinates of O_2 $(\theta_2,\ \omega,\ R_2)$ are given by

$$\begin{aligned} &\theta_2 = \theta_m \\ &R_2 = R\cos\frac{\theta_w}{2} - 2R\sin\frac{\theta_w}{2}\frac{h}{l} + R\sin\frac{\theta_w}{2}\left(\frac{l}{4h} + \frac{h}{l}\right) \end{aligned} \tag{2-13}$$

In the general case, the coordinates of a material point on the middle surface of the imperfection is $(\theta,\ \omega,\ R_I)$, where the radius of the imperfection, R_I (Figure 2-5b) , is given by:

$$R_I = R\sin\frac{\theta_w}{2}\left(\frac{l}{4h} + \frac{h}{l}\right) \tag{2-14}$$

The location of a material point on the deformed middle surface of the imperfection is

$$\overline{\mathbf{r}} = R_2\mathbf{i}_2 + u_\theta\mathbf{i}_\theta + u_\omega\mathbf{i}_\omega + \left(R_I + w\right)\mathbf{i}_r \tag{2-15}$$

where $R_2\mathbf{i}_2$ is the location of the center of the imperfection, $(u_\theta,\ u_\omega,\ w)$ are the displacements tangent and normal to the undeformed middle surface, and $(\mathbf{i}_\theta,\ \mathbf{i}_\omega,\ \mathbf{i}_r)$ are the corresponding unit vectors. For axisymmetric deformations, the circumferential displacement equals to zero $u_\omega = 0$, and the other displacements, u_θ and w, are independent of the circumferential angle ω.

The nonlinear strains and the change in curvature of the middle surface are functions of the linear components of the strains $\left(e_{\theta\theta},\ e_{\omega\omega},\ e_{\theta\omega}\right)$ and the rotations $\left(\varphi_{\theta},\ \varphi_{\omega},\ \varphi_{r}\right)$, the former given by:

$$
\begin{aligned}
e_{\theta\theta} &= \frac{1}{R_I}\left(\frac{\partial u_\theta}{\partial \theta}+w\right)\\
e_{\omega\omega} &= \frac{1}{R_I\cos\theta+R_2\cos\theta_2}\left(\frac{\partial u_\omega}{\partial \omega}-\tan\theta u_\theta+\cos\theta w\right)\\
e_{\theta\omega} &= \frac{1}{2R_I\left(R_I\cos\theta+R_2\cos\theta_2\right)}\left[\left(R_I\cos\theta+R_2\cos\theta_2\right)\frac{\partial u_\omega}{\partial \theta}+R_I\frac{\partial u_\theta}{\partial \omega}+R_I\sin\theta u_\omega\right]
\end{aligned}
\tag{2-16}
$$

For axisymmetric deformations, the circumferential displacement .. and the partial derivatives with respect to the circumferential angle ω in $e_{\omega\omega}$ and $e_{\theta\omega}$ equal to zero.

The linear rotations about the tangents and normal of the middle surface are expressed as:

$$
\begin{aligned}
\varphi_\theta &= \frac{1}{R_I}\left(\frac{\partial w}{\partial \theta}-u_\theta\right)\\
\varphi_\omega &= \frac{1}{R_I\cos\theta+R_2\cos\theta_2}\left(\frac{\partial w}{\partial \omega}-\cos\theta u_\omega\right)\\
\varphi_r &= \frac{1}{2R_I\left(r\cos\theta+R_2\cos\theta_2\right)}\left[\left(R_I\cos\theta+R_2\cos\theta_2\right)\frac{\partial u_\omega}{\partial \theta}-R_I\frac{\partial u_\theta}{\partial \omega}-R_I\sin\theta u_\omega\right]
\end{aligned}
\tag{2-17}
$$

For axisymmetric deformations, the last two terms vanish ($\varphi_\omega = 0$ and $\varphi_r = 0$), whereas the non-vanishing components of the nonlinear middle surface strains for axisymmetric deformations are given by Eq. (2-5). The non-vanishing changes in curvature for axisymmetric deformations are

$$
\begin{aligned}
K_{\theta\theta} &= \frac{1}{R_I}\left[\left(1+e_{\theta\theta}+e_{\omega\omega}+e_{\omega\omega}e_{\theta\theta}\right)\left(-1+\frac{\partial\varphi_\theta}{\partial\theta}-e_{\theta\theta}\right)-\varphi_\theta\left(1+e_{\omega\omega}\right)\left(\frac{\partial e_{\theta\theta}}{\partial\theta}+\varphi_\theta\right)+1\right]\\
K_{\omega\omega} &= \frac{\cos\theta}{R_I\cos\theta+R_2\cos\theta_2}\left[\left(1+e_{\varphi\varphi}+e_{\omega\omega}+e_{\omega\omega}e_{\varphi\varphi}\right)\left(-1-\tan\theta\varphi_\theta-e_{\omega\omega}\right)\right.\\
&\quad\left.+\tan\theta\varphi_\theta\left(1+e_{\omega\omega}\right)\left(e_{\theta\theta}-e_{\omega\omega}\right)+1\right]
\end{aligned}
\tag{2-18}
$$

From a comparison of Eqs. (2-16)-(2-18) with Eqs. (2-3), (2-4) and (2-6), we find that the linearized strains of the middle surface, the linearized rotation and the change in curvature of the imperfection, have expressions identical to those of a spherical shell with $R_I = R$ and $R_2 = 0$. This describes the limiting case, where the geometry of the imperfection becomes a sphere ($R_2 = 0$), and its size matches that of the spherical shell ($R_I = R$).

The stress strain relations, the elastic strain energy, the volume change for live pressure, and the total potential energy are then given by Eqs. (2-7), (2-8), (2-11), and (2-12).

2.4.3 Finite element modelling

To investigate the shell response controlled by an imperfection varying in size and location, a set of FEM simulations (ABAQUS/STANDARD) were also conducted in parallel to the experimental and theoretical work described above. The complimentary results not only provide context for validation but also serve to study shell sensitivity to defect amplitude and position as well as radius to thickness ratio (Section 2.5.2). For the base material (VPS elastomer), we adopted an incompressible neo-Hookean model, whose coefficients were calculated from previously obtained measures (Pezzulla et al. [39] of Young's modulus and Poisson's ratio (Table 2-2). Clamped boundary conditions were applied at the equator of the hemispherical shell, while a uniform external pressure was imposed on the outer surface of the shell. Due to the unstable post-buckling behavior, the search for the equilibrium path was carried out through the modified Riks method [46].

Two geometries were examined for the shell. The first replicates the non-uniform thickness (Figure 2-3b) induced by the manufacturing process (see Appendix 2.8.1 for inclusion of thickness variation), while the latter reproduces the ideal uniform thickness of the perfect shell, providing a baseline for comparison. Furthermore, since spherical shell deformation can be either axisymmetric or non-axisymmetric [35], both scenarios were examined. For the former, the linear line element SAX1 was used due to its ability to capture only axisymmetric deformation, and for the latter, we built a three-dimensional model with two types of shell elements (linear quadrilateral shell elements S4R with reduced integration, and 3-node triangular shell elements S3R) that together can capture the non-axisymmetric deformation. A set of mesh convergence studies (Appendix D) was performed to determine the sufficient number of elements for each type: 80

elements for the SAX1 axisymmetric line element, and around 10000 for S4R and S3R shell elements.

2.5 Results and discussion

2.5.1 Buckling of imperfect spherical shells with large axisymmetric imperfection

We present here a set of theoretical, computational and experimental results of the shell response to a uniform externally applied pressure under two scenarios: i) as-designed imperfection with a priori assumed thickness (uniform profile), and ii) as-built imperfection with actual thickness variation induced by manufacturing (non-uniform profile).

2.5.1.1 Effects of as designed and as manufactured imperfections

Figure 2-6a shows the baseline response of a perfect hemispherical shell along with that of a shell with as-designed imperfection with uniform thickness and shell geometry given in Table 2-1. The blue dashed line is for the perfect baseline hemispherical shell and represents the classical buckling response extensively investigated in literature [16, 35]. Normalized with the Zoelly's buckling pressure $p_C = 2E(t/R)^2/\sqrt{3(1-\nu^2)}$ [9], the pressure rapidly increases with tiny changes in volume up to unity. Post bifurcation, a monotonic plunge of pressure appears, followed by a gradually descending plateau (just below 0.1) that spans the entire range of $\Delta V / V_0$.

The purple and red curves in Figure 2-6a refer to the imperfect shell with as-designed uniform thickness. The former (purple dots) is the pressure provided by our theoretical model (Section 2.4.2), which assumes axisymmetric deformations, and the latter (red) that obtained by our numerical models (Section 2.4.3), one accounting for axisymmetric (dash-dot) and the other for non-axisymmetric (solid line) deformation. For axisymmetric deformations, the difference between theoretical and FEM models is below 1%. In addition, the responses from the FEM models for both axisymmetric and non-axisymmetric deformations are well aligned with 3.6% relative difference in maximum pressure, a result implying shell deformation being close to axisymmetric. At the volume change of $\Delta V / V_0 = 0.04$, the pressure of the imperfect shell enters a region of snap-through buckling, after which the pressure monotonically increases to reach a maximum value of $p / p_C = 0.34$ at $\Delta V / V_0 = 0.40$.

The divergence between axisymmetric and non-axisymmetric modes occurs at the snap-through region, where the FEM simulation captures an additional peak, which can be attributed to the non-axisymmetric buckling mode. This is shown in Figure 2-6b; here the sequential stages of deformation reveal the start of a buckling transition mode from axisymmetric to non-axisymmetric, the latter requiring lower strain energy than the former and hence most likely to appear. The second peak corresponds to the return of the deformation to the axisymmetric response. After the second peak, the value of pressure gradually approaches the solution of our theoretical model for axisymmetric deformations. Despite the qualitative difference between the red and purple curves, the pressure value of the second peak is only 10% higher than the pressure value at the identical volume change predicted by the theoretical and FEM models for axisymmetric deformations. This result suggests that the axisymmetric mode can provide a sufficient level of approximation for shell design.

A number of differences emerge between the perfect and imperfect shell shown in Figure 2-6a. The main one is their buckling mode. The imperfect shell first undergoes snap-through buckling at a pressure lower than the maximum pressure, and then it regains stability as the pressure increases to the maximum, a phenomenon not observed in the perfect spherical counterpart. The perfect shell undergoes bifurcation buckling for a tiny value (below 1%) of the normalized volume change, where the pressure reaches its maximum without undergoing snap-through instability. After the bifurcation point, the post-buckling pressure decreases monotonically until the shell is everted, thereby denying the chance for the shell to regain stability [35, 47, 48].

Maximum pressure and corresponding volume change are other attributes (besides the buckling mode) that differ in value between the perfect and imperfect shells (Figure 2-6a). The maximum pressure in the imperfect case (point B) decreases to 34% of the theoretical maximum pressure ($p / p_c = 1$) of the perfect shell baseline (not shown in figure). This drop is minor compared to the buckling pressure of perfect shells fabricated with conventional processes; for perfect shells, the experimental values measured in the literature show a large spread with severe drops (up to 90%)

from the ideal case [16, 34]. These well-known results attest to the large sensitivity of perfect shells to geometric defects. On the other hand, the imperfect shell under investigation in this study can provide a maximum pressure value (point B) comparable to that of its perfect counterpart. A similar observation applies to its impact on the volume change. For the perfect hemispherical shell, a tiny value of $\Delta V / V_0 < 0.01$ is required to attain maximum pressure before proceeding spontaneously to catastrophic collapse without an increase in the magnitude of the applied pressure. In contrast, the imperfect shell after the first peak features a gradual and stable response over a large volume change, thereby demonstrating its capacity to resist deformation upon an increase of the applied pressure up to the maximum pressure value reached at $\Delta V / V_0 = 0.40$.

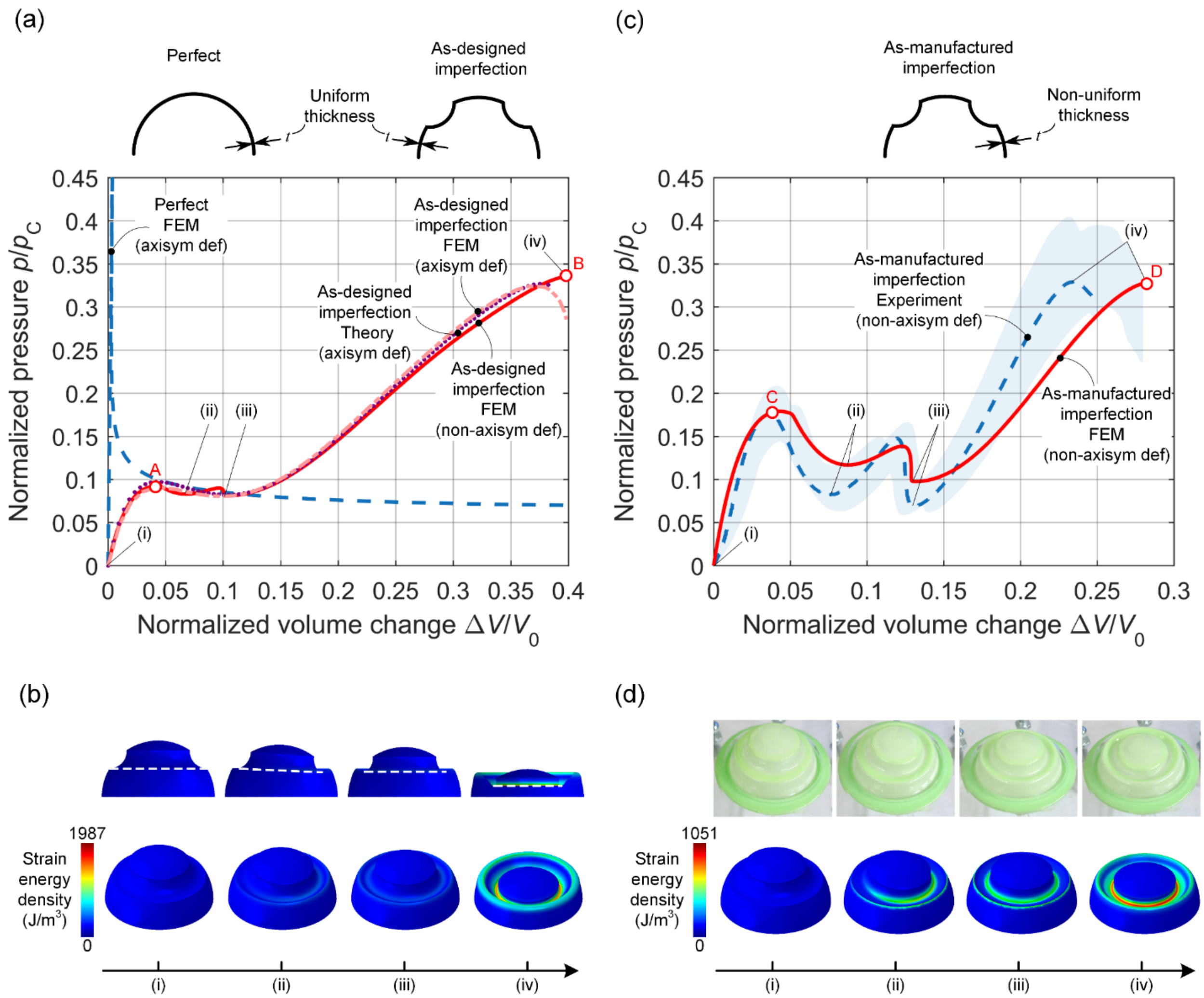

Figure 2-6 Responses of perfect and imperfect spherical shells under uniform pressure. (a) Pressure versus change in volume for perfect and as-designed imperfect shell with uniform thickness, with volume change normalized by the negative of the volume within the middle surface of the undeformed hemisphere, $V_0 = -2\pi R^3 / 3$. Loss of stability for the perfect shell appears with a small volume change, as opposed to the imperfect shell, which remains stable post snap-through buckling for a wide range of volume change. The theoretical solution accounts for axisymmetric deformations, whereas non-axisymmetric modes are captured by FEM. (b) Cross-section view (above) and three-dimensional view (below) of deformed modes and corresponding strain energy density of as-designed imperfect shell with uniform thickness. Changes in the inclination of the horizontal dashed lines below the cap indicate buckling transition from axisymmetric to a non-axisymmetric mode. (c) Pressure versus change in volume obtained from experiment and FEM simulation for as-manufactured imperfect shell with as-measured non-uniform thickness. (d) Deformed configurations from experiments on shell samples (above) and FEM accounting for non-axisymmetric deformations in as-built shell samples (below) along with corresponding strain energy density.

Figure 2-6b shows sequential stages of deformation for the imperfect shell with uniform thickness (solid red curve in Figure 2-6a). At the onset, the shell stays axisymmetric, and its cap reseats without tilting, as shown by the white dashed line tracing the bottom of the imperfection. When the pressure reaches the first peak, a non-axisymmetric response starts to develop. As illustrated in Figure 2-6b (ii), with an increase of the volume change the strain energy density localizes on the right-hand side of the imperfection, and the cap sinks with a tilt to the right hand side. Here the strain energy refers to the energy stored in the shell due to stretching and bending. After the second buckling peak, the localized strain energy starts to propagate circumferentially along the axisymmetric imperfection. At the second local minimum of pressure, the left-hand side of the imperfection also tilts until its height equals that of the right-hand side (Figure 2-6c (iii)). From this stage onward, shell axisymmetry is preserved and no further changes in deformation mode occur up to the maximum pressure (Figure 2-6c (iv)).

Thickness non-uniformity (Figure 2-2) caused by the fabrication process is another factor influencing the snap-through buckling, as shown in Figure 2-6c. The dashed blue line represents the experimental measure of the normalized pressure for one representative sample, and the shaded domain (light blue) is the envelope of responses generated by the eight samples here tested. Similar to Figure 2-6a, the imperfect shell first undergoes snap-through buckling with two local peaks in pressure, followed by a stable response that requires additional deformation to reach the maximum pressure. Aligned with the experimental curves is the computationally obtained response in red with two peaks in pressure in the snap-through region that capture non-axisymmetric deformation. By comparing the solid line curves for the imperfect shell in Figure 2-6 a and c, we can gain insights into the effect of thickness variation on the maximum pressure (point B versus point D) and its corresponding volume change, as well as the snap through pressure (point A versus point C). For the maximum pressure, the deviation is minor (2%) and it occurs with relatively modest change of volume change (29%). This infers a minor sensitivity of the maximum pressure to thickness variations. For the snap through pressure, on the other hand, the impact is severe (93% increase) attesting a high sensitivity as opposed to the volume change which is almost unaffected (5% difference).

Similar to the as-designed imperfect shell (Figure 2-6b), Figure 2-6d shows snapshots of deformation for the as-manufactured shells obtained from experiments (above) and FEM (below). After the first snap-through (Figure 2-6d (ii)), the as-manufactured shell undergoes non-axisymmetric buckling, characterized by strain energy localization mainly in the middle of a given cross-section of the large imperfection. After the second snap-through, the deformation returns to an axisymmetric mode (Figure 2-6d (iii)) until the pressure reaches the maximum (Figure 2-6d (iv)).

In general, the results presented above from shell theory, experiments and FEA are very well aligned with a maximum 5.9% relative difference in maximum pressure. We attribute the reason for these deviations to other imperfections that might be present in our samples but that were neglected in our models. During fabrication, defects intrinsic to the manufacturing process, such as thickness variation along the meridional and circumferential direction, geometric imperfections of the mold, and impurities in the base material, e.g. microvoids, might appear and contribute to the mild departure from the experimental results [34]. In addition, the thickness profile, which was modelled with a relative high level of accuracy (see Appendix 2.8.1), is still an approximation that could play a role in overestimating the minimum pressure in the snap-through region (Figure 2-6c).

2.5.2 Sensitivity to as-designed large geometric imperfection

Here we investigate the buckling sensitivity of a uniform thickness shell with an as-designed imperfection to a set of defects varying in size and location within its hemispherical geometry. We focus on axisymmetric deformations only, given that section 2.5.1 has shown the assumption of axisymmetric deformation leads to a deviation of the normalized maximum pressure of 3.6% from the non-axisymmetric case, hence retaining a sufficient level of accuracy for the study here undertaken.

Let us first define the parameters governing the snap-through buckling response for an imperfect shell with axisymmetric deformation. Figure 2-7 shows a representative response of pressure-volume change, where p_1 and p_2 specify the pressure at the limit points of the initial snap-through buckling, and $p_{\max}$ represents the obtainable maximum pressure. For the metrics here used, we adopt the normalized maximum pressure $p_{\max}/p_{\mathrm{C}}$, the snap-ratio $|p_1-p_2|/p_1$, and the ratio between snap-through pressure and the maximum pressure $p_1/p_{\max}$, along with their counterparts in volume change $V_{\max}/V_0$, $|V_1-V_2|/V_1$, and $V_1/V_{\max}$. p_{C} is Zoelly's buckling pressure. V_0 is the volume of a perfect hemisphere. The definition of these snap ratios enables the assessment of the relative difference in pressure and volume change between the limit points of the snap-through buckling branch [49].

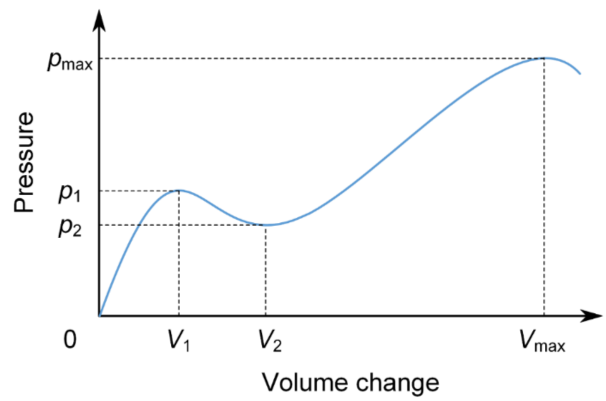

Figure 2-7 Pressure-volume change response of an imperfect shell undergoing axisymmetric deformations. The pressures at the limit points p_1 and p_2 along with the volume change V_1 and V_2 are introduced to describe the snap-through behavior.

Although the large imperfection here presented applies also to degenerate imperfect shells reducing to a cone (Figure 2-1f), in this section we restrict our sensitivity study to hemispherical geometries with imperfection parameters falling within given geometric ranges. Specifically, the angular width θ_w is assumed to range from 2.4° to 24°, the amplitude h/l from 0.05 to 0.5, the meridional angle θ_m from 30° to 70°, and the radius to thickness ratio R/t from 20 to 150. We prescribe also the radius of the shell to be $R = 25$ mm. To ease a systematic interpretation of the results, we divide the other four geometric parameters into two groups. The first describes the size of the imperfection, including the angular width θ_w and the amplitude h/l. The second designates the location of the imperfection and the slenderness of the shell, including the meridional angle θ_m and the radius to thickness ratio R/t. The study then is carried out by exploring the impact of changing the values of one group at a time, i.e. assuming the parameters of the other group are given.

2.5.2.1 Sensitivity to imperfection size

Here, the imperfection size is meant to describe changes in both the angular width θ_w ranging from θ_w=2.4° to 24° and the defect amplitude h/l spanning the interval 0.05 to 0.5. These are the variables, as opposed to the meridional angle and the radius to thickness ratio which are prescribed ($\theta_m = 45°$ and $R/t = 100$).

Figure 2-8 shows four possible modes for the imperfect shell to respond to pressure. We classify them with respect to the deformation mechanism that corresponds to the maximum pressure achievable within the entire response, i.e. the curve: p/p_C versus $\Delta V/V_0$. Mode 1 resembles the classical instability of a perfect spherical, i.e. an inward dimple-like shape (Figure 2-8a) and it is governed by small values of the imperfection (e.g. $\theta_w = 4.6°$ and $h/l = 0.1$) [35, 50]. Here the pressure first increases linearly up to the bifurcation point $p/p_C = 0.81$ at $\Delta V/V_0 = 0.01$, before dropping abruptly to a plateau around $p/p_C = 0.1$. Post bifurcation, there is a deviation in pressure at $\Delta V/V_0 = 0.18$, which is caused by the dimple deformation reaching and interacting with the imperfection, a secondary phenomenon that follows shell collapse. This is a secondary peak of pressure much smaller than the maximum value characterizing mode 1, hence it is of negligible significance. It should also be noted that for a real shell, the maximum pressure may be significantly reduced by other types of defects, e.g. small dimple at the pole, which might be introduced by the manufacturing process.

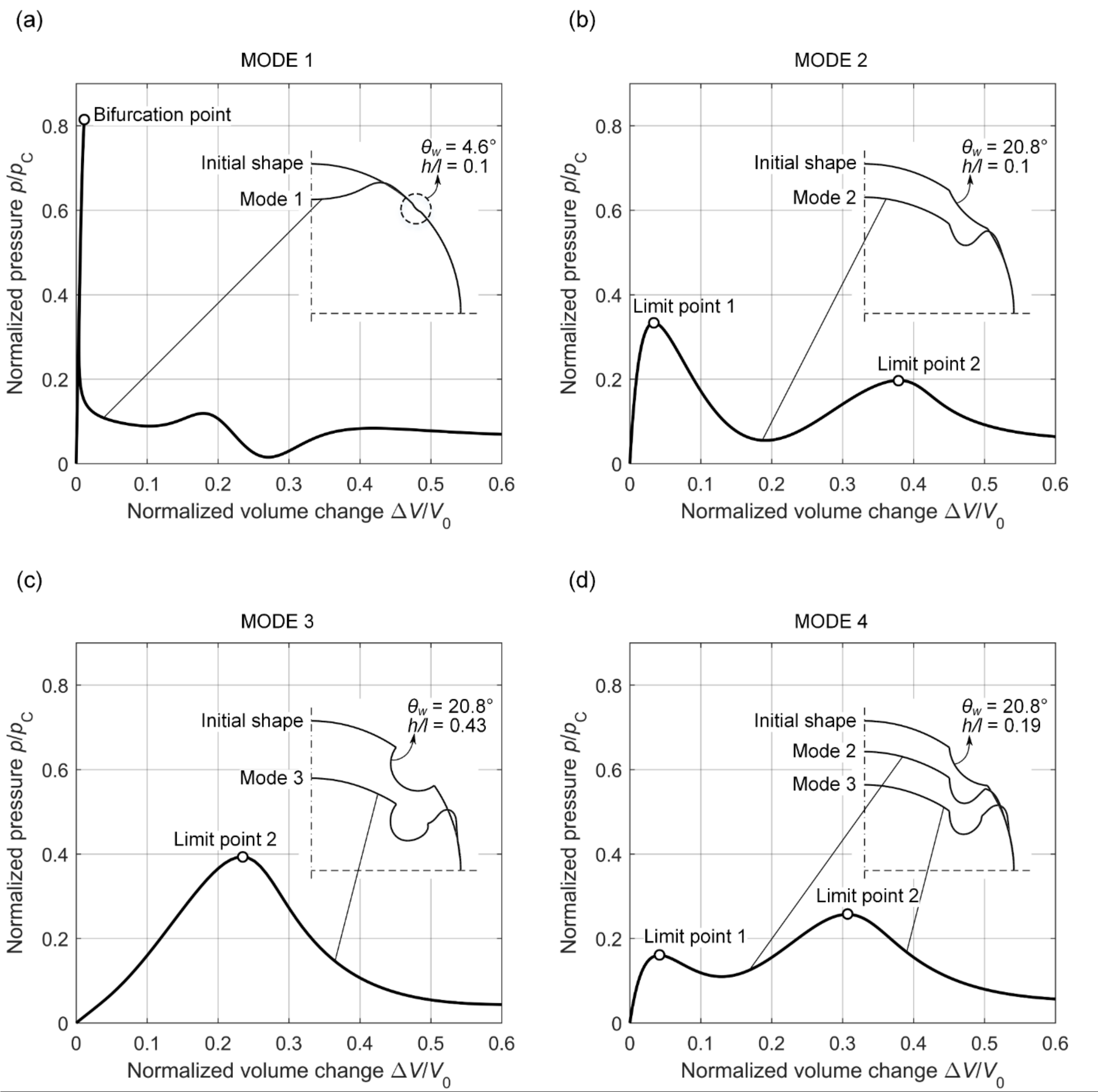

Figure 2-8 Possible deformation modes leading to shell collapse. (a) Mode 1: Bifurcation buckling characterized by a dimple-like shape response. (b) Mode 2: Snap-through buckling 1 describing localized deformation within the imperfection. (c) Mode 3: Snap-through buckling 2 representative of localized deformation below the imperfection. (d) Mode 4: Snap-through buckling combining mode 2 and 3.

Mode 2 identifies a post-buckling response with deformation localized within the imperfection region (Figure 2-8b). This mode indicates a transition from bifurcation to snap through buckling. It is governed by a larger imperfection size with values (e.g. $\theta_w = 20.8°$ and $h/l = 0.1$) above a lower critical bound, as illustrated and further explained in a subsequent figure (Figure 2-9). The pressure here increases monotonically to the maximum at the limit point 1 ($p/p_{\mathrm{C}} = 0.33$) before starting to descend. While the pressure at the limit point 1 is much smaller than the bifurcation pressure in mode 1, the maximum volume change ($\Delta V/V_0 = 0.03$) is still close to that of mode 1. Following snap-through, the pressure may reach a second peak, i.e. limit point 2, at a larger volume change. Its value, however, does not define mode 2 because it is lower than the maximum attainable pressure, i.e. limit point 1, hence it is not considered further.

Figure 2-8c illustrates mode 3, a snap-through buckling controlled by a localized deformation accrued below the imperfection. This response is caused by increasing values of the imperfection size (e.g. $\theta_w = 20.8°$ and $h/l = 0.43$). Snap-through buckling occurs at limit point 2, which is the maximum attainable pressure ($p/p_{\mathrm{C}} = 0.39$) achieved at $\Delta V/V_0 = 0.23$, a value much larger than that observed in mode 1 and 2.

For all of the aforementioned buckling modes (1, 2, and 3), the shell collapses once the prescribed pressure exceeds the buckling pressure. Mode 4 (Figure 2-8d) is hybrid case combining modes 2 and 3. It describes a scenario where snap-through buckling with mode 2 arises before the attainment of the maximum pressure with mode 3. This behaviour is triggered by a large width and moderate amplitude of the imperfection (e.g. $\theta_w = 20.8°$ and $h/l = 0.19$). In addition, this mode can also be triggered in full spheres that are not clamped at the equator (see Appendix 2.8.5). Although the modes in Figure 2-8 is obtained from one imperfection, they can also form a cascade of snap-through buckling in a shell with multiple imperfections (see Appendix 2.8.6).

A map summarizing the buckling modes obtained for a range of combinations of imperfection width θ_w and amplitude h/l is shown in Figure 2-9a. This map helps gain insight into the transition between buckling modes for a given set of imperfection parameters. From visual inspection, we gather that small imperfections lead to mode 1, visualized as the zone in the lower-left corner and below the solid red bound. Within this domain, the lower bounds of the two parameter ranges ($\theta_w = 2.4°$ and $h/l = 0.05$), i.e. the smallest imperfection size, generate the highest maximum pressure ($p_{\max}/p_{\mathrm{C}} = 0.91$), which approaches the theoretical buckling pressure of a perfect spherical shell. As the imperfection size increases, snap-through buckling becomes dominant and replaces bifurcation buckling. From the map, we further observe a set of buckling mode transitions, first to mode 2, and then to mode 4 and mode 3 as controlled by the geometric descriptors of the imperfection. For mode 2, the maximum pressure (at limit point 1) decreases monotonically – as it is the case for mode 1 - if either the imperfection width θ_w or amplitude h/l is increased. When limit point 1 is lower than limit point 2, the buckling mode switches to mode 4, which combines modes 2 and 3. This mode is sandwiched between the zones of mode 3 and mode 2 on the middle-low part of the right hand side of the map, characterized by imperfections with large width θ_w and moderate amplitude h/l. As limit point 1 continues to decrease with increasing θ_w and h/l, it may disappear leaving limit point 2 as the only limit point. The buckling mode here switches to mode 3, which lies in the upper-right corner of the map. In both domains of mode 3 and mode 4, the maximum pressure is attained at limit point 2, and has a reversed trend with the maximum value increasing with both imperfection width and amplitude. The highest maximum pressure in these modes ($p_{\max}/p_{\mathrm{C}} = 0.44$) appears at the upper-right corner for the largest imperfection size ($\theta_w = 24°$ and $h/l = 0.5$).

(a)

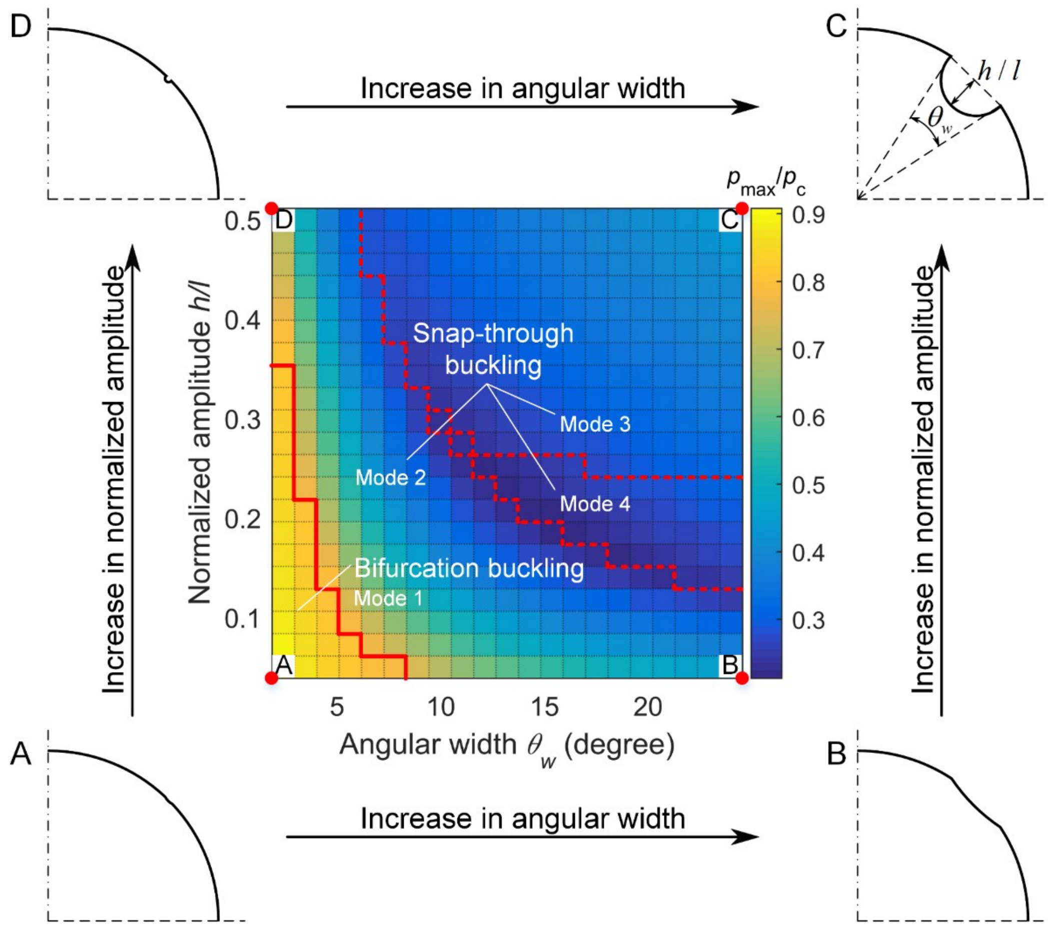

D
C
A
B
Increase in angular width
Increase in angular width
Increase in normalized amplitude
Increase in normalized amplitude
h / l
θw
pmax/pc
0.9
0.8
0.7
0.6
0.5
0.4
0.3
Normalized amplitude h/l
0.5
0.4
0.3
0.2
0.1
5
10
15
20
Angular width θw (degree)
Snap-through buckling
Mode 2
Mode 3
Mode 4
Bifurcation buckling
Mode 1

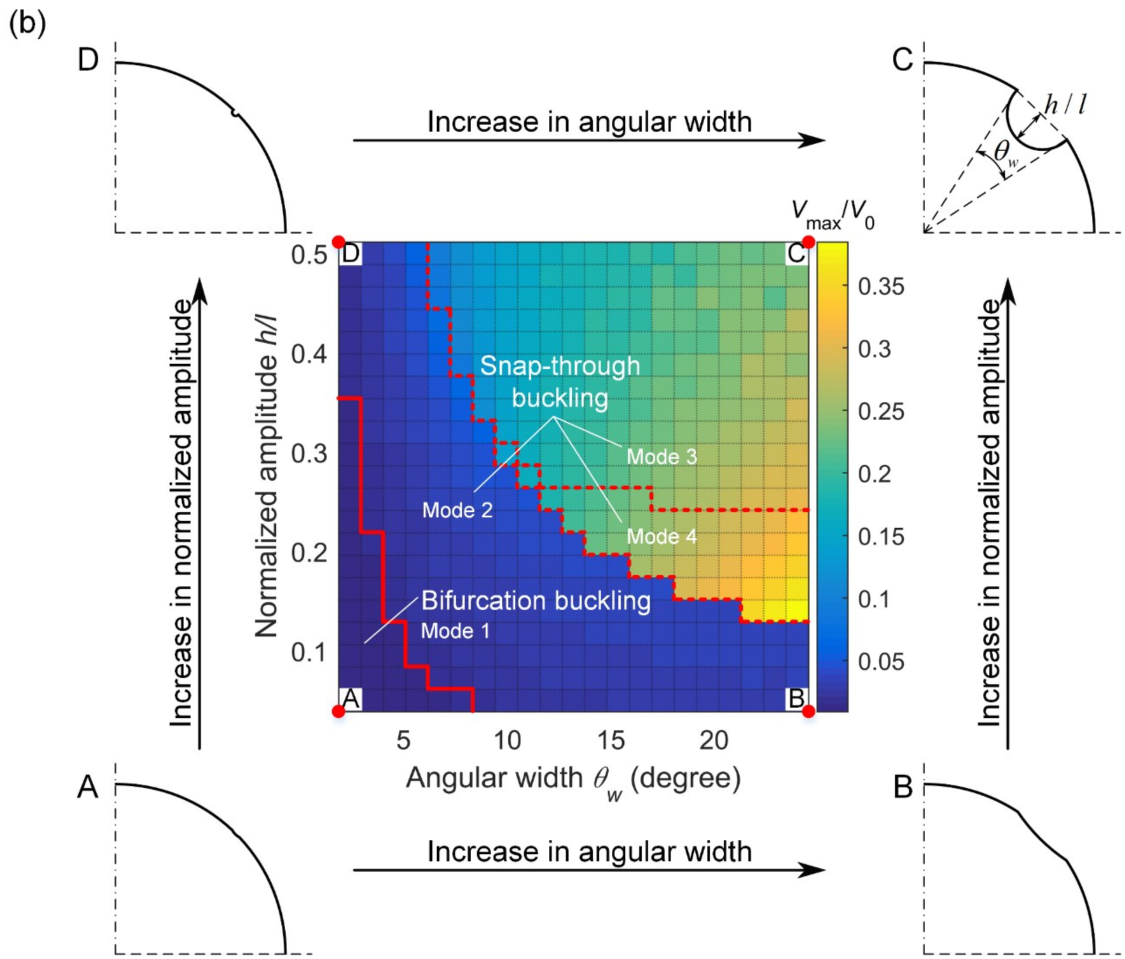

Figure 2-9 Role of imperfection size on (a) the normalized maximum pressure and (b) the normalized volume change at the maximum pressure. With an increase in imperfection size, the buckling mode transitions from bifurcation buckling to snap-through buckling.

Figure 2-9b shows a corresponding map of the normalized maximum volume change. In mode 1 and 2, $V_{\max}/V_0$ is small, typically below 0.07, indicating that here the slightly imperfect shells start to collapse in a configuration resembling its undeformed state. For shells in mode 3 and mode 4, the maximum volume change is attained at limit point 2 with larger values ranging from $V_{\max}/V_0 = 0.08$ to $V_{\max}/V_0 = 0.38$. In these domains, the maximum volume change increases with the imperfection width θ_w and decreases with the amplitude h/l. In addition, $V_{\max}/V_0$ is continuous across the boundary between mode 2 and mode 3, but discontinuous across the boundary between modes 2 and 4. In the former case, the transition in buckling mode is smooth and determined by the condition of volume change equality at limit points 1 and 2. In the latter case, the discontinuous transition to mode 4 implies snap-through occurs prior to the maximum pressure with limit point 1 existing at a volume change lower than that of limit point 2.

Another important insight into the snap-through response of imperfect shells can be gained by plotting (Figure 2-10 a and b) the snap ratios of both pressure $|p_1 - p_2|/p_1$ and the volume change $|V_1 - V_2|/V_1$, with terms defined in Figure 2-7. In these plots the domain of mode 4 is the only domain mapped, since for the others snap-through cannot take place prior to the attainment of the maximum pressure. A reduction of the imperfection amplitude h/l increases the snap ratios $|p_1 - p_2|/p_1$ and $|V_1 - V_2|/V_1$, which translate into the attainment of larger ranges of pressure and volume change. Despite its minor influence, θ_w has an impact on the snap-through response; if θ_w becomes too small, the capacity to snap-through prior to the attainment of the maximum pressure is lost and the shell may enters the domain of mode 1 or mode 2.

To further characterize the competition between limit points 1 and 2 in mode 4, we compare the values of their pressure (Figure 2-10c) and volume change (Figure 2-10d). The change in the snap-through pressure with respect to reduced values of the defect amplitude h/l and width θ_w is shown in Figure 2-10c. Here smaller values make p_1 at limit point 1 approach the maximum pressure $p_{\max}$ at limit point 2, a condition that describes the points on the lower bound of the mode 4 domain. A further decrease of h/l and θ_w make the shell transition to failure mode 2, i.e. the pressure at limit point 1 becomes higher than that of limit point 2 and catastrophic collapse occurs with snap-through. A similar comparison between limit points attributes is shown in Figure 2-10d for the volume change. Here, for all combinations of h/l and θ_w in mode 4, the volume change at limit point 1 is well below that at limit point 2 ($V_1/V_{\max} \leq 0.45$), a condition that corresponds to the jump in the maximum volume change $V_{\max}/V_0$ (Figure 2-9b) from mode 2 to mode 4. We also find that the difference in volume change between the limit points reduces with increasing imperfection amplitude h/l and decreasing width θ_w until the point where mode 2 and mode 3 tend to take place at the identical value of volume change. This observation agrees with the discontinuity in

V_{max}/V_0 shown in Figure 2-9b, where at the boundary between mode 2 and mode 3 (left-hand side) the discontinuity in V_{max}/V_0 diminishes for large imperfection amplitude h/l and small width θ_w.

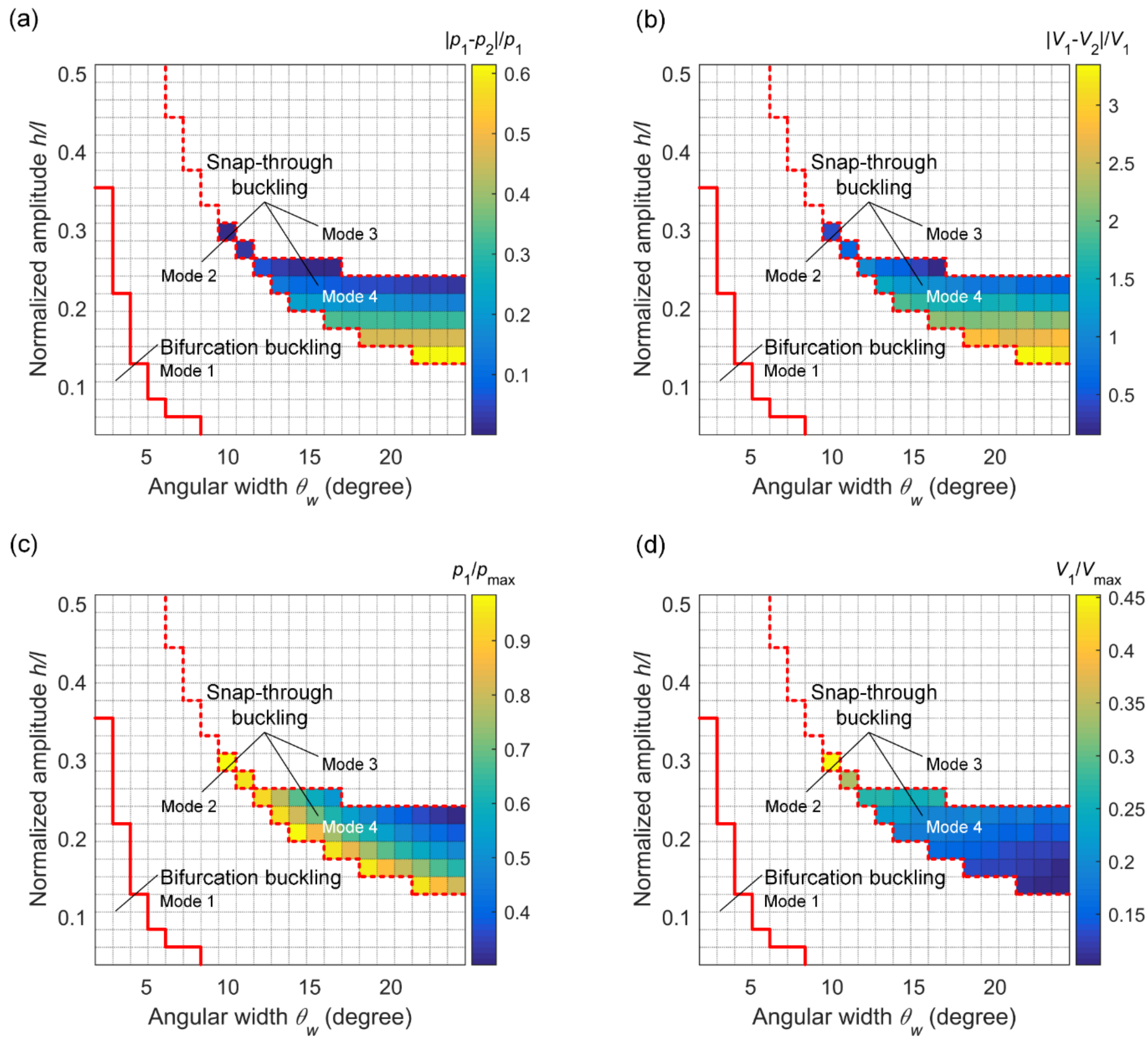

Figure 2-10 Role of imperfection size on snap-through properties. (a) and (b) Snap ratios of pressure and volume change. (c) Ratio of snap-through pressure over maximum pressure. (d) Ratio of snap-through volume change against maximum volume change.

2.5.2.2 Sensitivity to meridional location of imperfection and radius to thickness ratio of shell

Complementary to the sensitivity plots of the previous section, here we map the role of the other geometric parameters of the imperfect shell, i.e. the defect meridional angle ranging from $\theta_m = 30°$

to 70°, and the radius to thickness ratio ranging from $R/t = 20$ to 150. This time the prescribed quantities are the angular width ($\theta_w = 20°$) and the amplitude ($h/l = 0.2$) of the defect.

Figure 2-11a depicts the competition between failure modes for varying values of the meridional angle θ_m and radius to thickness ratio R/t. Since in this case sizeable values of h/l and θ_w are assumed, snap-through buckling occurs at a pressure much lower than the theoretical bifurcation pressure of perfect shells. As a result, the domain of mode 1 recedes in the map, and only failure mode 2 emerges for small θ_m and R/t, with the highest maximum pressure $p_{\max}/p_{\mathrm{C}}$ obtained at point A. The maximum pressure $p_{\max}/p_{\mathrm{C}}$ is attained with limit point 1 and decreases with both the meridional angle θ_m and the radius to thickness ratio R/t. As R/t increases, a switch from failure mode 2 to mode 4 occurs at the boundary of the domains representing the range of R/t values that enable limit point 1 to equal limit point 2. On the other hand, for mode 3 to appear, θ_m should assume large values. For both mode 3 and mode 4, there is a minor change in the maximum pressure for increasing values of R/t and θ_m.

Figure 2-11b shows the maximum volume change $V_{\max}/V_0$ for each buckling mode. Mode 2 features a low maximum volume change, typically below 0.17, meaning that the shell collapses immediately without departing much from its undeformed state. Similar to Figure 2-9b, a jump in the maximum volume change is found between mode 2 and mode 4, caused by the difference in volume change between the limit points. For both mode 3 and mode 4, the maximum volume change $V_{\max}/V_0$ is attained at limit point 2, which decreases monotonically with the meridional angle θ_m but it is insensitive to the radius to thickness ratio R/t. The highest maximum volume change of $V_{\max}/V_0 = 0.52$ appears in mode 4 for a meridional angle at its lower bound ($\theta_m = 30°$).

Similarly to Figure 1-11, Figure 2-12 depicts the snap-through landscape prior to the attainment of the maximum pressure in mode 4. The snap ratios $|p_1 - p_2|/p_1$ and $|V_1 - V_2|/V_1$ are plotted for varying values of θ_m and R/t, showing the dominant role of the meridional angle θ_m as opposed to that of R/t; the larger the meridional angle, the smaller the snap ratios. This observation points to the choice of a low meridional angle θ_m to attain more sizable and exploitable variation in pressure and volume change. On the other hand, the radius to thickness ratio R/t has minor influence on the snap ratios, yet very small R/t is still capable of switching mode 4 into mode 2.

Figure 2-12 c and d show the buckling mode competition between the limit points of domain 4. The former is a plot of $p_1/p_{\max}$, the ratio of the snap-through pressure at limit point 1 over the maximum pressure at limit point 2. The latter is the corresponding plot for $V_1/V_{\max}$. $p_1/p_{\max}$ increases with the decrease of both the meridional angle and the radius to thickness ratio, with a value close to unity at the boundary between the domains of mode 2 and mode 4. With further decrease in θ_m and R/t, the pressure at limit point 1 overcomes that at limit point 2, hence resembling the conditions of mode 2. In Figure 2-12d, the ratio of volume change between the limit points $V_1/V_{\max}$ has a small value from 0.1 to 0.37, a result indicating the large difference between limit points 1 and 2, the former being far below the latter. This explains the abrupt change in the maximum volume change $V_{\max}/V_0$ observed in Figure 2-11b at the boundary between mode 2 and 4. In addition, the value of $V_1/V_{\max}$ increases with θ_m and decreases with R/t, a trend that indicates the occurrence of the limit points at identical values of the volume change, as further corroborated in Figure 2-11b for large θ_m and small R/t.

In summary, the sensitivity investigation carried out above provides valuable insights into the competition between the four buckling modes. The snap ratios quantify the variations in pressure and volume change caused by snap-through buckling at limit point 1, while the ratio of snap-through pressure over the maximum pressure and its counterpart in volume change allows to assess the difference in pressure and volume change between limit points 1 and 2. With these metrics it is possible to characterize the four domains. Bifurcation (mode 1) is triggered by small-sized imperfections and provides the highest maximum pressure. However, since an extremely small volume change leads to bifurcation, the collapse is sudden and spontaneous with no warning of departure from the undeformed shape; the shell here exhausts its capacity to provide further resistance to deformation. As the imperfection increases in size, however, the snap-through modes (2, 3, 4) become dominant, thereby providing additional resistance before the attainment of the maximum pressure. Harnessing defect location and size enables to channel the buckling mode and, as needed by the application, the transition between domains, escaping mode 1 to access mode 2 and mode 3, each corresponding to a maximum pressure value attained at either limit point 1 (mode 2), or at limit point 2 (mode 3). Mode 4 combines mode 2 and mode 3 and represents the failure mechanism for which the pressure at limit point 1 is below that of limit point 2.

On the limitations of the sensitivity study here presented, we recall that our numerical analysis can only predict axisymmetric deformations. Peaks of pressure caused by non-axisymmetric modes, such as those in Figure 2-6b, cannot be captured, but these peaks should be accounted for, should the application require it. Yet again, the choice of focusing in this sensitivity study on the axisymmetric case rather than the non-axisymmetric one is motivated by the minor discrepancy (3.6%) between their maximum pressure. We also recall that for hemispherical shells, the bifurcation pressure can be significantly 'knocked down' by as-manufactured imperfections, which were not considered here. Their impact on the failure mode, however, would be apparent in the mode 1 domain, which would fill a larger area.

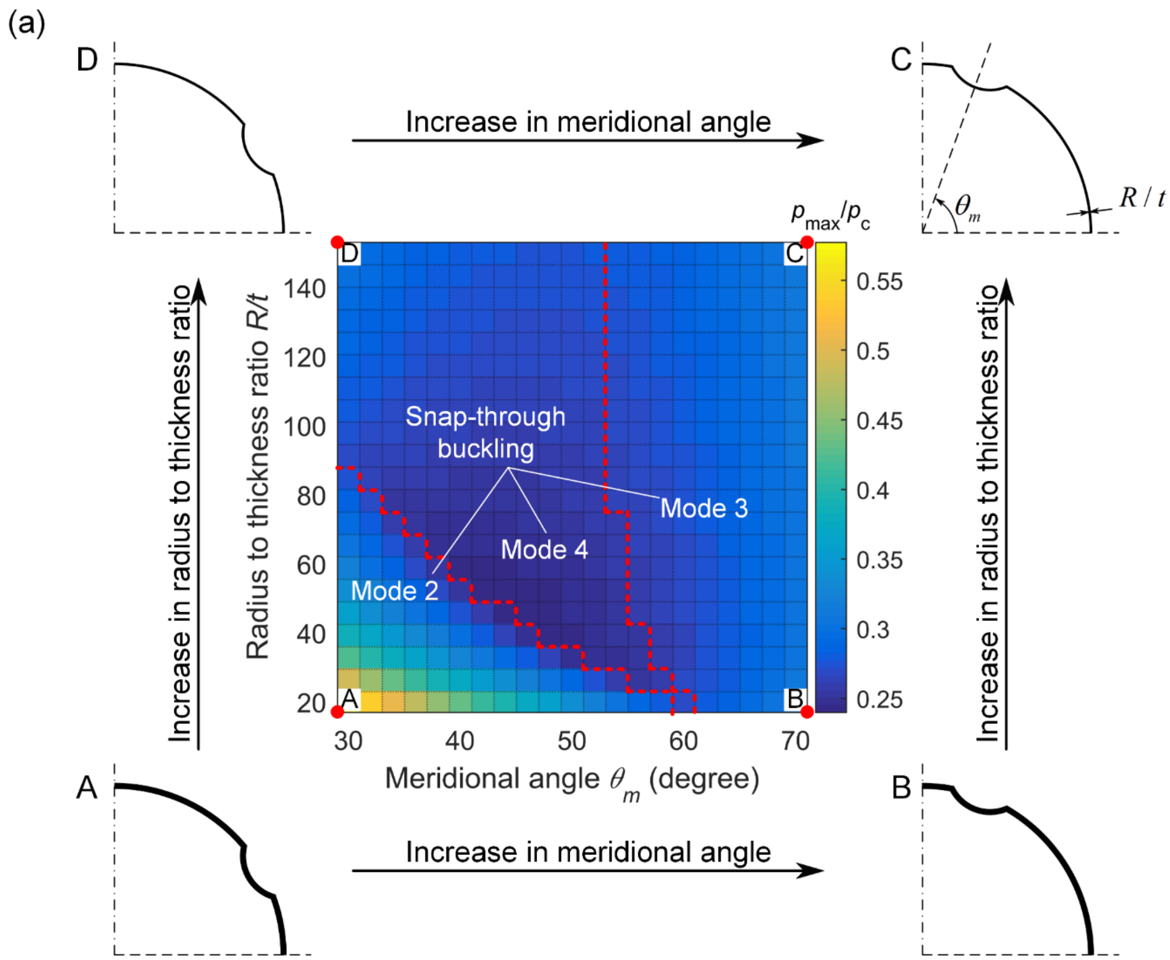
(a)
D
C
A
B
Increase in meridional angle
Increase in meridional angle
Increase in radius to thickness ratio
Increase in radius to thickness ratio
θ_m
R / t
p_{max}/p_c
Radius to thickness ratio R/t
Meridional angle θ_m (degree)
Snap-through buckling
Mode 2
Mode 3
Mode 4
20
40
60
80
100
120
140
30
40
50
60
70
0.25
0.3
0.35
0.4
0.45
0.5
0.55

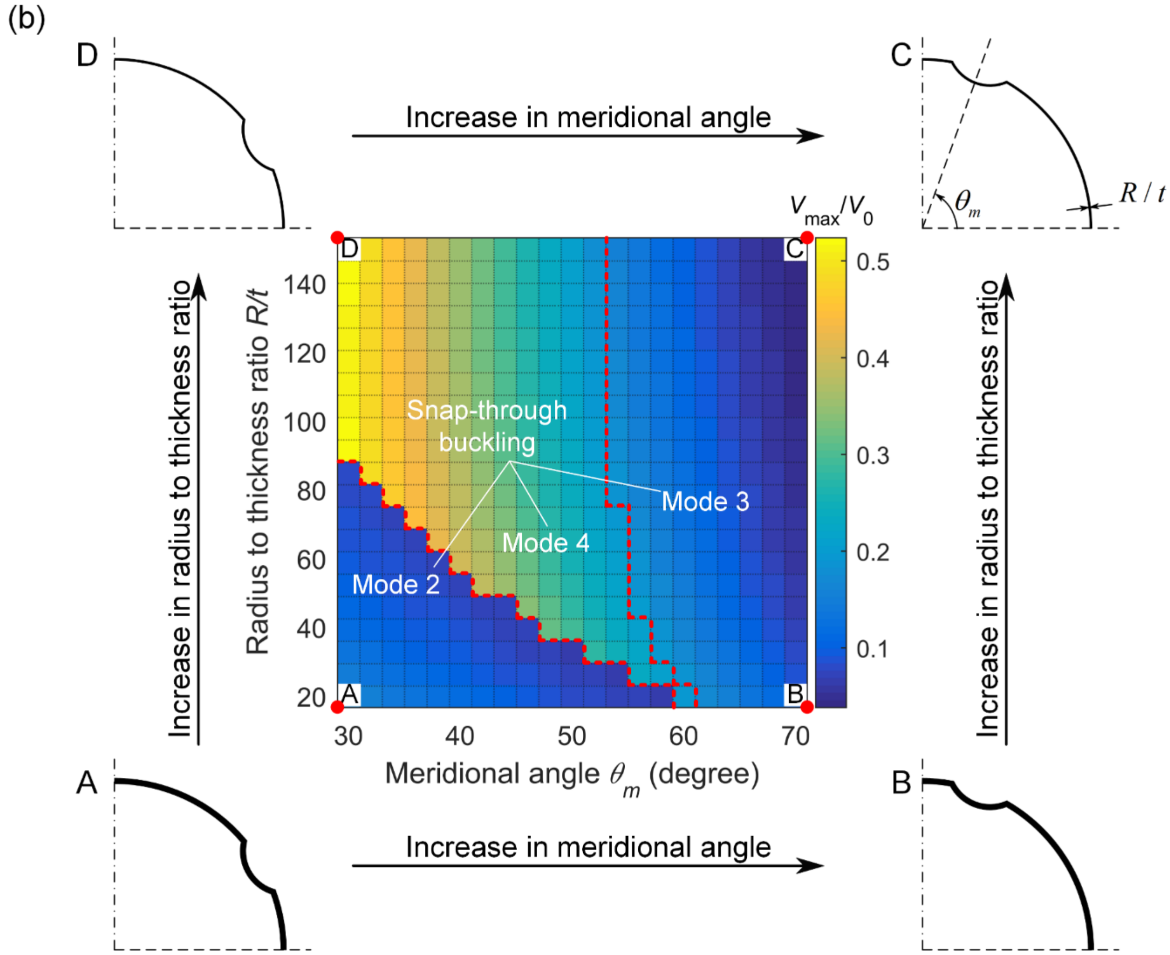

Figure 2-11 Role of the meridional angle θ_m and the radius to thickness ratio R/t on (a) the normalized maximum pressure and (b) the normalized volume change at the maximum pressure.

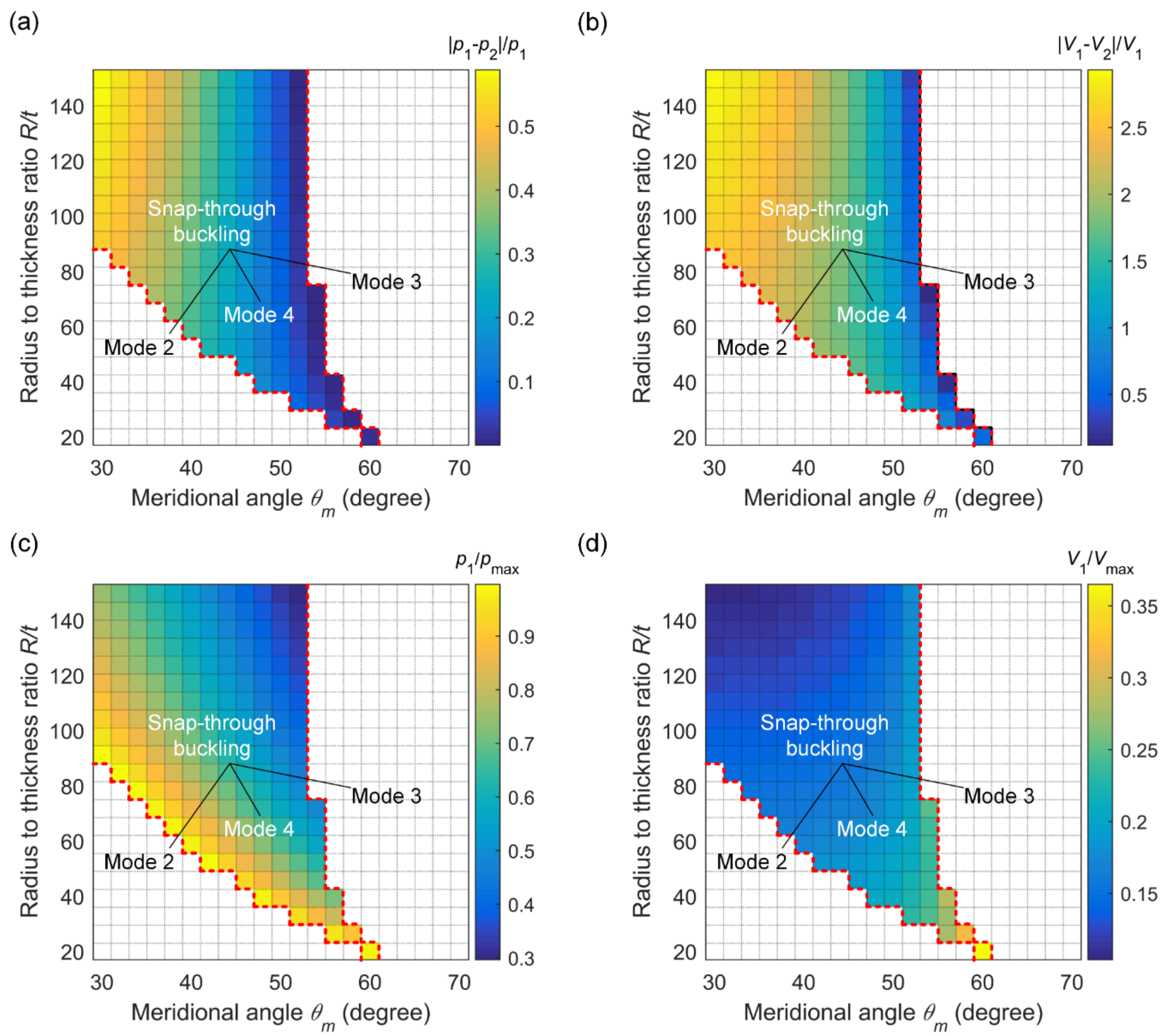

Figure 2-12 Role of meridional angle θ_m and radius to thickness ratio R/t on snap-through properties. (a) and (b) Snap ratios of pressure and volume change. (c) Ratio of snap-through pressure over maximum pressure. (d) Ratio of the snap-through volume change over maximum volume change.

2.6 Concluding remarks

This paper has investigated the impact of a large axisymmetric imperfection on the buckling response of a thin elastic shell subject to uniform external pressure. Our shell theory formulation employs exact stretching and bending strain measures as well as live pressure loading, and can predict buckling for imperfect shells with uniform thickness. For shells of non-uniform thickness, results from experiments and numerical solutions are in quantitative agreement. A number of findings have emerged from the results.

First, a large axisymmetric imperfection can cause the shell response to depart from bifurcation buckling, i.e. the classical dimple-like shape of perfect shells typically triggered by a tiny change in volume. Integrating a large axisymmetric defect into the shell geometry can localize the deformation at the site of the imperfection, which causes snap-through followed by an increase in the post-buckling pressure until the attainment of the maximum pressure. The benefit here is twofold. The maximum achievable volume can reach as high as 0.4, and the maximum attainable pressure is reduced only by 66% from the theoretical buckling pressure of an ideal perfect shell, as opposed to the 90% drop reported in the experimental measurements for as-manufactured perfect shells in the literature.

Second, the buckling response of the imperfect shell can be approximated with an axisymmetric mode. The symmetric breaking of deformation only occurs during the snap-through buckling prior to the attainment of maximum pressure, causing minor (below 4%) deviation in the maximum pressure. This result suggests that the axisymmetric deformation can provide a sufficient level of approximation for shell design.

Third, a sensitivity study on imperfections of varying size and location along with shell radius to thickness ratio has unveiled a number of insights into the buckling landscape of imperfect elastic shells.

- **Buckling modes.** Four modes have been identified for an imperfect shell with axisymmetric defect: bifurcation instability caused by small sized imperfections, and three snap-through responses yielded by large sized imperfections. Their domains have been mapped into charts that show their boundaries and buckling mode competition over a range of combinations of their defect descriptors (defect amplitude h/l, angular width θ_w, and meridional angle θ_m) and shell geometry (radius to thickness ratio R/t);
- **Attainable maximum pressure.** Defect size and location as well as shell radius to thickness ratio can be harnessed to modify the normalized maximum pressure over a large range of values. The bifurcation mode (mode 1), which resembles the response of a perfect shell, yields the highest normalized maximum pressure ranging from $p_{\max}/p_c = 0.78$ to 0.91. The snap-through modes (modes 2, 3, and 4) provide a wide range of maximum pressure from $p_{\max}/p_C = 0.21$ to 0.81. Despite the reduction in maximum pressure, the

imperfect shell can still attain values comparable to those measured in literature for as-manufactured perfect shells.

- **Attainable maximum volume change.** Similarly to the maximum pressure, the normalized maximum volume change can also be increased by harnessing the defect geometry and shell radius to thickness ratio. In particular, $\Delta V/V_0$ for mode 1 remains low (2%) and close to the value for a perfect shell (below 1%), whereas for the snap-through modes 2, 3, and 4, $V_{\max}/V_0$ increases substantially up to 17%, 31%, and 52% respectively.
- **Competition of snap-through buckling modes**. Imperfection amplitude h/l and meridional angle θ_m are the most influential parameters that govern snap-through buckling in mode 4. By harnessing these parameters within the geometric ranges here investigated, the snap ratio of pressure can span 0 to 0.61, and the snap ratio of volume change can range between 0.12 and 3.35. These ranges offer a sizeable snap-through tunability that could be exploited for the design of soft robots and morphing metamaterials.

2.7 Acknowledgement

This work was supported by the Natural Sciences and Engineering Research Council of Canada (Grant # 208241).

2.8 Appendix

2.8.1 Approximation of the non-uniform thickness profile of the as-manufactured shell

In Figure 2-13a, we partitioned the thickness profile of the shell into eight sections (i)-(viii) so as to linearly approximate the thickness profile in each section. The acquired data was then used to generate the corresponding FEM model (Figure 2-13b). The nodal thickness profile in the FEM model was expressed using a cylindrical coordinate system $(\rho,\ \varphi,\ z)$ whose origin is located at the center of the spherical shell. As such, the thickness in each of the eight sections is:

$$
\begin{aligned}
t_{i} &= 0.25 \\
t_{ii} &= (\rho - 10.15)/2.59 * 0.37 + 0.25 \\
t_{iii} &= -(\rho - 12.74)/1.13 * 0.50 + 0.62 \\
t_{iv} &= 0.25 - (z - 14.51)/5.95 * 0.13 \\
t_{v} &= (\rho - 16.22)/3.59 * 0.63 + 0.25 \\
t_{vi} &= -(\rho - 19.82)/1.45 * 0.80 + 0.88 \\
t_{vii} &= 0.20 - (z - 11.20)/1.40 * 0.12 \\
t_{viii} &= 0.20
\end{aligned}
\tag{A.1}
$$

where ρ is the radial distance from the z-axis, φ is the azimuth angle, and z is the height from the plane of equator.

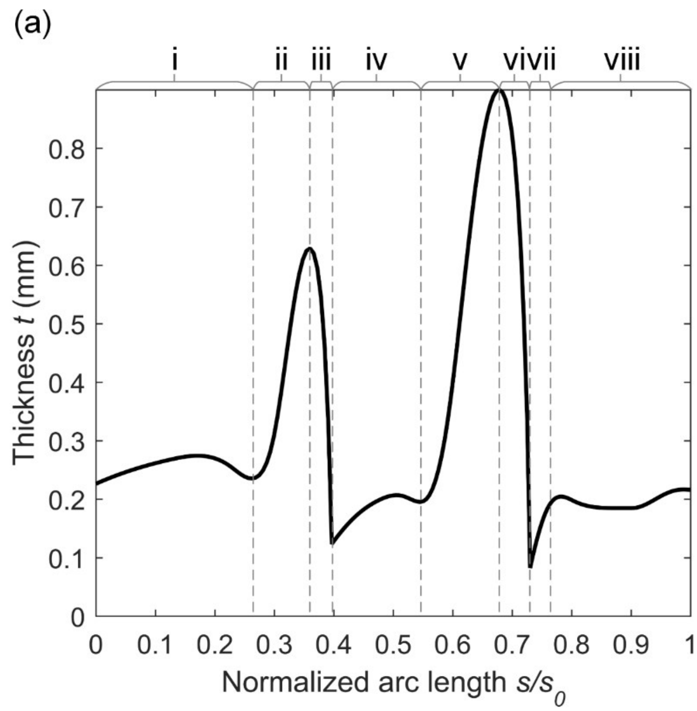

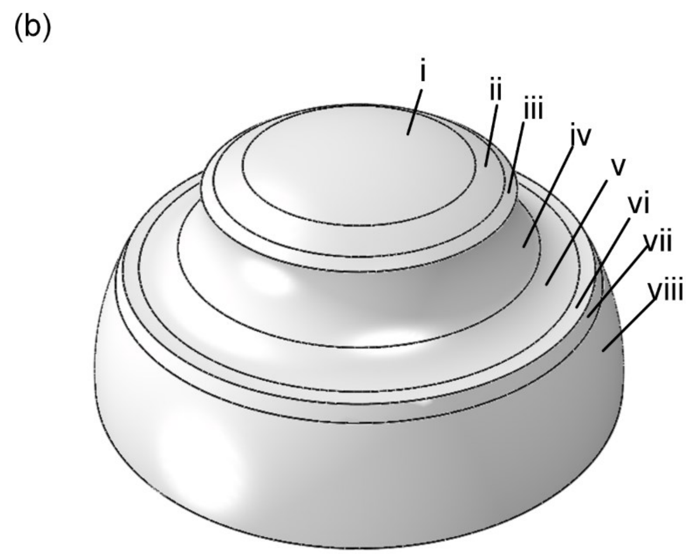

Figure 2-13 Partition of (a) the thickness profile and (b) the FEM model.

2.8.2 Tensor analysis of the middle surface of a shell

Here we present the main equations of the exact shell theory formulation given by Niordson [44]. With a focus on a shell of an arbitrary shape, the parametric relations f^i between the Cartesian coordinates x^i and the coordinates $\left(u^1, u^2\right)$ on the middle surface of the shell can be written as:

$$x^i = f^i\left(u^1, u^2\right) \tag{B.1}$$

The first fundamental tensors (metric or fundamental tensor) of the undeformed and the deformed coordinated systems are

$$a_{\alpha\beta} = f^i_{,\alpha} f^i_{,\beta} \tag{B.2}$$

and

$$a^*_{\alpha\beta} = \left(f^i + \overline{v}^i\right)_{,\alpha}\left(f^i + \overline{v}^i\right)_{,\beta} \tag{B.3}$$

where $\overline{v}^i$ is the displacement in the Cartesian coordinates. An asterisk marks quantities in the deformed state. The second fundamental tensors (curvature tensor) of the undeformed and the deformed coordinated systems are

$$d_{\alpha\beta} = X^i f^i_{,\alpha\beta} \tag{B.4}$$

and

$$\begin{aligned} d^*_{\alpha\beta} = \left(\frac{a}{a^*}\right)^{\frac{1}{2}} \Bigg[& \left(1 + p_\varepsilon{}^\varepsilon + \frac{p}{a}\right)\left(d_{\alpha\beta} + D_\beta q_\alpha + d^\gamma_\beta p_{\alpha\gamma}\right) \\ & -\left(q^\rho + \varepsilon^{\rho\beta}\varepsilon^{\gamma\delta} q_\gamma p_{\delta\beta}\right)\left(D_\beta p_{\alpha\rho} - d_{\beta\rho} q_\alpha\right)\Bigg] \end{aligned} \tag{B.5}$$

where X^i is a unit vector normal to the middle surface, $p_{\alpha\beta} = D_\alpha v_\beta - d_{\alpha\beta} w$ is the two-dimensional displacement gradient, D_α is the symbol for covariant derivative, $q_\alpha = d_{\alpha\beta} v^\beta + w_{,\alpha}$ is the rotation perpendicular to the normal of the surface, and $\varepsilon_{\alpha\beta}$ is the alternating tensor. The quantities without indices are given by the determinants:

$$\begin{aligned} a &= \det\left(a_{\alpha\beta}\right) = a_{11}a_{22} - a_{12}a_{21} \\ a^* &= \det\left(a^*_{\alpha\beta}\right) = a^*_{11}a^*_{22} - a^*_{12}a^*_{21} \\ p &= \det\left(p_{\alpha\beta}\right) = p_{11}p_{22} - p_{12}p_{21} \end{aligned} \tag{B.6}$$

The rotation around the normal of the middle surface is

$$\Theta = \frac{1}{2}\varepsilon^{\alpha\beta} p_{\alpha\beta} \tag{B.7}$$

The strain tensor is defined by

$$\begin{aligned} E_{\alpha\beta} &= \frac{1}{2}\left(a^*_{\alpha\beta} - a_{\alpha\beta}\right) \\ &= \frac{1}{2}\left(p_{\alpha\beta} + p_{\alpha\beta} + p_{\alpha}{}^{\lambda} p_{\alpha\lambda} + q_\alpha q_\beta\right) \end{aligned} \tag{B.8}$$

where the factor $\frac{1}{2}$ is employed to make the definition of strain measure conform with the Lagrangian stretching strain.

The change in curvature is

$$\begin{aligned} K_{\alpha\beta} &= d^*_{\alpha\beta} - d_{\alpha\beta} \\ &= \left(\frac{a}{a^*}\right)^{\frac{1}{2}} \left[\left(1 + p_\varepsilon{}^{\varepsilon} + \frac{p}{a}\right)\left(d_{\alpha\beta} + D_\beta q_\alpha + d^\gamma_\beta p_{\alpha\gamma}\right)\right. \\ &\quad \left. - \left(q^\rho + \varepsilon^{\rho\beta}\varepsilon^{\gamma\delta} q_\gamma p_{\delta\beta}\right)\left(D_\beta p_{\alpha\rho} - d_{\beta\rho} q_\alpha\right)\right] - d_{\alpha\beta} \end{aligned} \tag{B.9}$$

Since the stretching strains are small in the current study, we assume $a/a^* \approx 1$ in the expression of the curvature change (Eq. (B.9)). This approximation is consistent with previous equations in the literature (Hutchinson [35]).

According to Koiter and van der Heijden [45], the volume change is

$$\Delta V = \int_S \left\{ w + \frac{1}{2}\left(w p_\alpha{}^\alpha - q_\alpha u^\alpha \right) + \frac{1}{6}\left[w\left(p_\alpha{}^\alpha p_\beta{}^\beta - p_\alpha{}^\beta p_\alpha{}^\beta \right) - 2u^\alpha \left(q_\beta p_\alpha{}^\beta - q_\alpha p_\beta{}^\beta \right) \right] \right\} \mathrm{d}S \quad \text{(B.10)}$$

2.8.3 Solution method for axisymmetric deformations with the shell formulation

We solved the axisymmetric problem of the imperfect shell based on the shell formulation in Section 2.4.2 with a numerical method (Hutchinson [35]. The hemispherical shell with as-designed large imperfection is divided into three parts: the imperfection, and the parts above and below the imperfection. These parts are connected by imposing the following continuity condition on displacement and rotation for axisymmetric deformation:

$$\begin{aligned} u_1^+ &= u_1^- \\ u_2^+ &= u_2^- \\ \varphi_\theta^+ &= \varphi_\theta^- \end{aligned} \quad \text{(C.1)}$$

where u_1 is the displacement along the horizontal direction, u_2 is the displacement along the vertical direction, φ_θ is the rotation, and the signs + and – indicate the two sides at a boundary.

Within each domain, the shell is discretized into N sections of equal length. We assign displacements tangent and normal to the middle surface, u_θ and w, as unknowns to the $6N+6$ nodes. An additional unknown is the external pressure p. The $6N+7$ unknowns form a vector λ of unknown displacements and pressure. Within each section, we use the shell theory for axisymmetric deformations presented in section 2.4.2 to calculate the average of the potential energy density. Then, the total potential energy is obtained by integrating the potential energy density in each section. The integrations and derivatives are computed numerically.

The solution is steered with the pole displacement w_{pole}. For each step, we prescribe the displacement at the upper pole w_{pole}. Then, we update the increment of the vector of unknowns $\Delta\lambda$ with Newton iterations to find a new equilibrium state

$$\Delta\lambda = -H^{-1}G \tag{C.2}$$

where G is the gradient of the total potential energy, and H^{-1} is the inverse of the hessian matrix. For each step, the Newton iteration is repeated until the solution converges. While this method is straightforward to code as mentioned by Hutchinson [35], it posed a limitation. When the number of unknowns is large, the computation of the hessian and its inverse becomes too expensive and reaching convergence in the process of finding a solution might be challenging.

2.8.4 Convergence study for theoretical and FEM models

We first performed a set of convergence studies for both the axisymmetric solution based on the shell formulation and the FEM simulations. The geometry parameters of the shell for both cases are listed in Table 2-1 (Section 2.4.1.1). The convergence study is performed by assuming a uniform thickness profile with a radius to thickness ratio $R/t = 123.6$.

Figure 2-14 shows the convergence study for the axisymmetric solution based on shell theory. By increasing the number of nodes, the solution gradually approaches the curve of the FEM simulation for axisymmetric deformations. The results of shell theory match well with the FEM results when 270 nodes are used in the numerical solution. Any further increase in the number of nodes makes the solution difficult to converge. Thus in this work, we use 270 nodes.

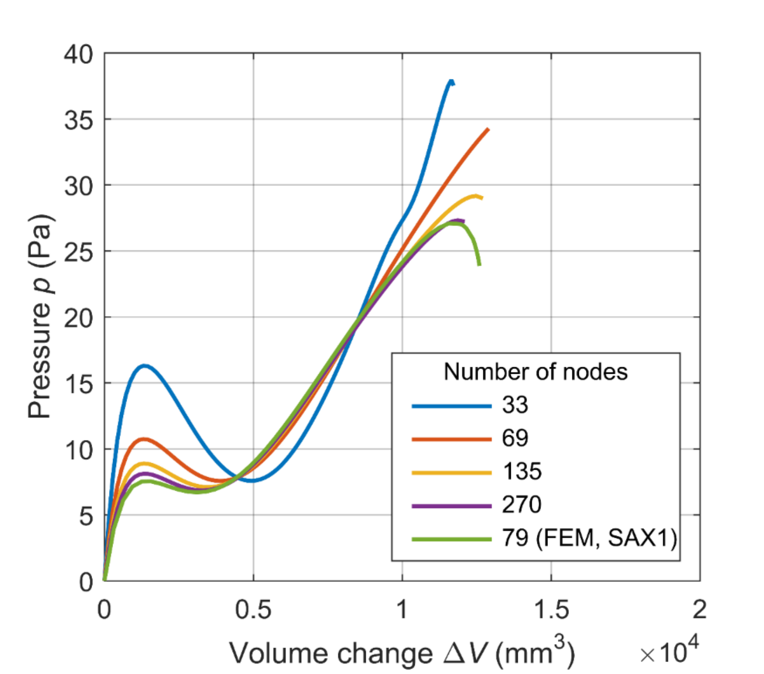

Figure 2-14 Convergence study of the axisymmetric solution based on shell theory. The green curve with SAX1 elements for axisymmetric deformation is shown as a reference.

Figure 2-15 shows the results for FEM simulations with SAX1 axisymmetric line elements. The simulation with 79 elements converges to the simulation employing 161 elements. Hence in this work we select an average of 80 elements.

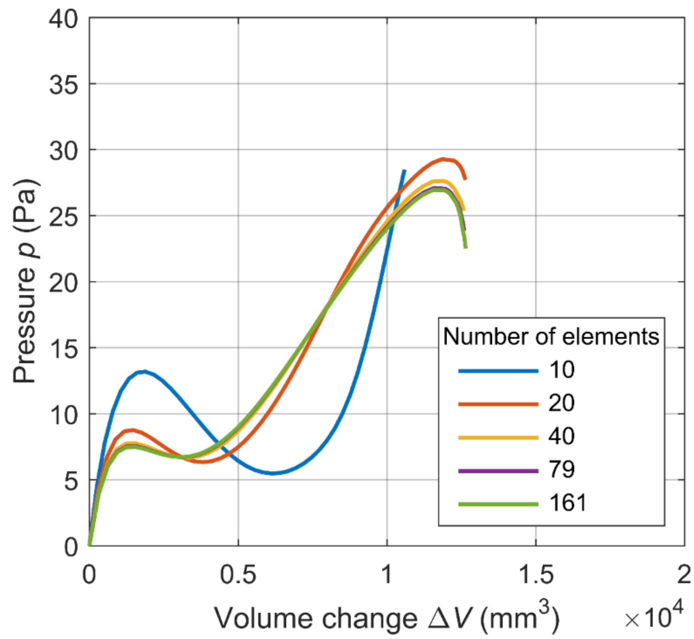

Figure 2-15 Convergence study of FEM simulations with SAX1 axisymmetric line elements

Figure 2-16 shows the results of the convergence study for FEM simulations with S4R and S3 shell elements. The simulation result with 10288 elements converges to that with 15220 elements. Hence in this work, we use around 10000 elements for the FEM simulations with shell elements.

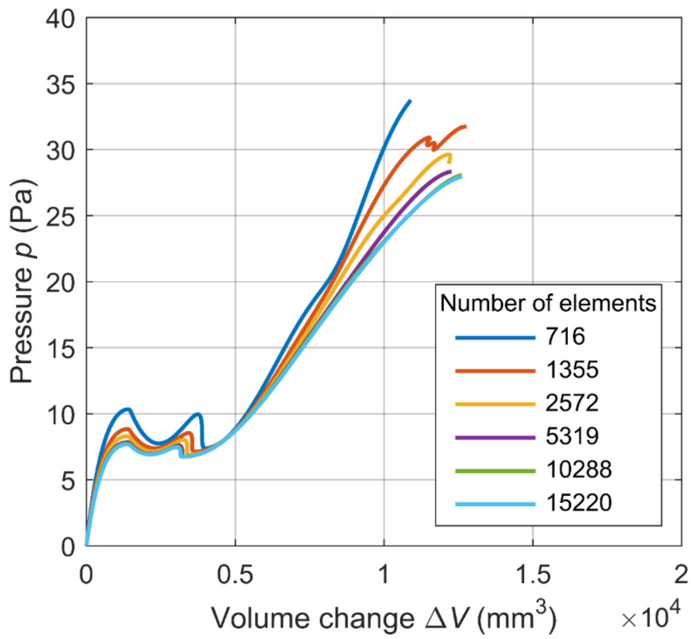

Figure 2-16 Convergence study of FEM simulations with S4R and S3R shell elements

2.8.5 The role of clamped support on the development of mode 4.

Here we aim at understanding the role of clamping the shell equator to trigger mode 4, i.e. snap-through buckling combining mode 2 and 3. A set of axisymmetric simulations have been performed to compare the buckling responses of two cases: a full sphere and a hemispherical shell, both with a prescribed imperfection. Figure 2-17 (below) shows the results. As observed, their normalized pressure curves and shell deformations show no difference for almost the entire response (stages (i) to (iii)), indicating that the influence of the clamping at the equator is not sizeable for shell buckling. This shows that mode 4 does appear also for the full sphere and it is not caused by clamping the equator. The difference between a full sphere and a hemisphere becomes significant only when the deformation zone reaches the equator (stage (iv)), an instance that shows that clamping the equator does constrains shell deformation. At this stage, collapse appears as shell eversion, a condition not examined in this work.

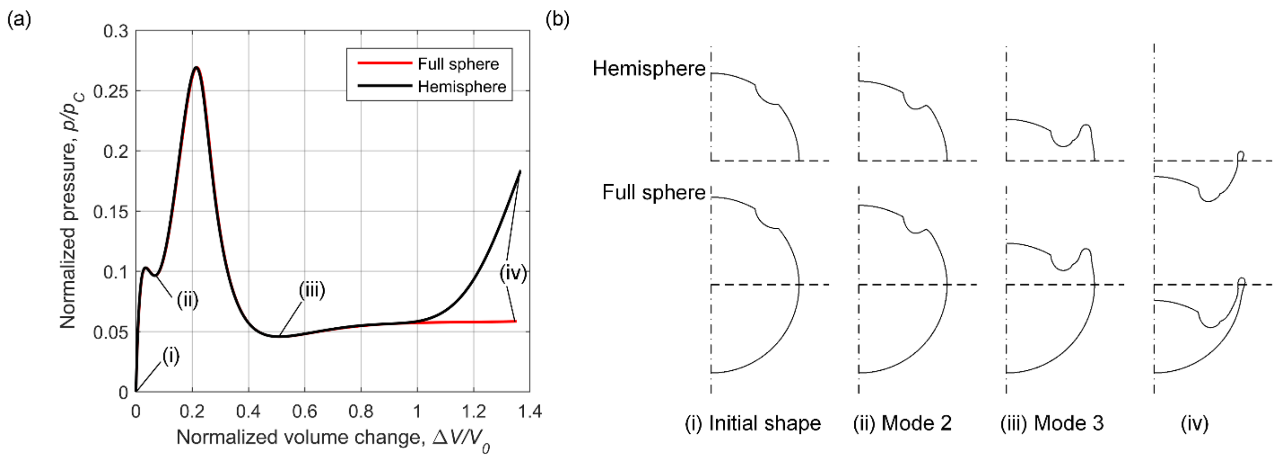

Figure 2-17 Responses of full and hemispherical shells with prescribed imperfection ($h/l = 0.2$, $\theta_w = 20°$, $R/t = 124$, and $\theta_m = 50°$). (a) Pressure versus change in with volume change normalized by the negative of the volume within the middle surface of the undeformed hemisphere, $V_0 = -2\pi R^3/3$. (b) Cross-section view of deformed modes (mode 4).

2.8.6 Cascade of snap through buckling in a shell with multiple imperfections

A cascade of snap through buckling can occur for certain combinations of defects. Figure 2-18 shows an example where two imperfections are examined in a shell with radius of 25 mm and radius to thickness ratio of 124 (Table 2-4 lists the geometric parameters). The result shows that the shell undergoes twice snap-through buckling with mode 2, before attaining the maximum pressure with mode 3.

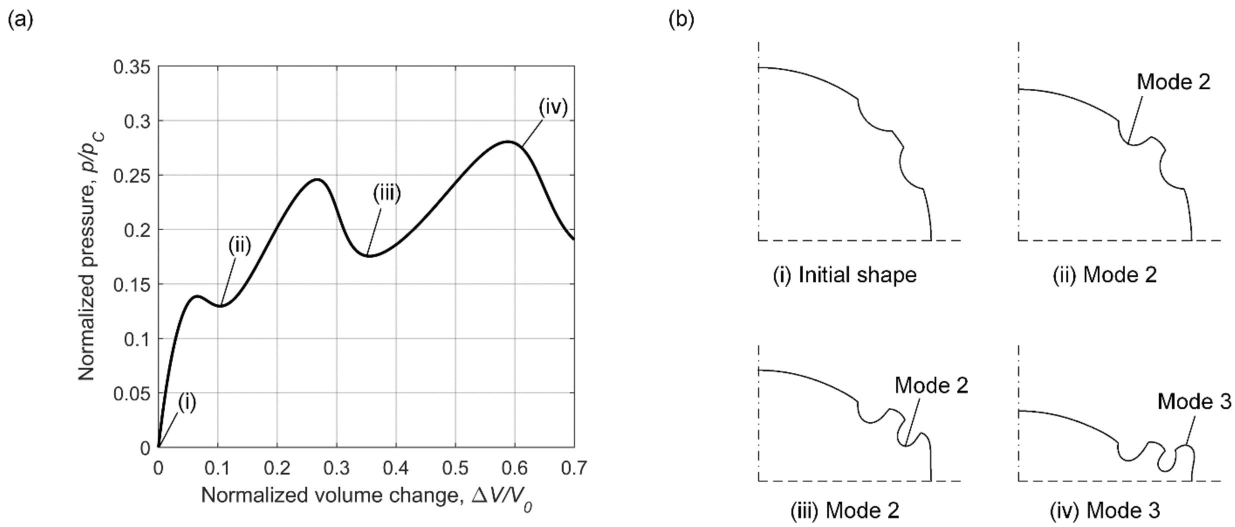

Figure 2-18 Responses of shell with two imperfections. (a) Pressure versus change in volume change normalized by the negative of the volume within the middle surface of the undeformed hemisphere, $V_0 = -2\pi R^3/3$. (b) Cross-section view of deformed modes (mode 4).

	h/t	θ_w (°)	θ_m (°)
Upper imperfection	0.21	15	47
Lower imperfection	0.26	15	24

Table 2-4 Geometric parameters of the imperfections.

2.9 References

[1] J. Arfsten, S. Leupold, C. Bradtmöller, I. Kampen, and A. Kwade, *Atomic force microscopy studies on the nanomechanical properties of saccharomyces cerevisiae.* Colloids and Surfaces B: Biointerfaces, 2010. **79**(1): p. 284-290.

[2] A. Vaziri and L. Mahadevan, *Localized and extended deformations of elastic shells.* Proceedings of the National Academy of Sciences, 2008. **105**(23): p. 7913-7918.

[3] E. Katifori, S. Alben, E. Cerda, D. R. Nelson, and J. Dumais, *Foldable structures and the natural design of pollen grains.* Proceedings of the National Academy of Sciences, 2010. **107**(17): p. 7635-7639.

[4] X. T. Nguyen, S. Hou, T. Liu, and X. Han, *A potential natural energy absorption material – coconut mesocarp: Part a: Experimental investigations on mechanical properties.* International Journal of Mechanical Sciences, 2016. **115-116**: p. 564-573.

[5] J. Jose, M. Kamp, A. van Blaaderen, and A. Imhof, *Unloading and reloading colloidal microcapsules with apolar solutions by controlled and reversible buckling.* Langmuir, 2014. **30**(9): p. 2385-2393.

[6] J. Błachut and K. Magnucki, *Strength, stability, and optimization of pressure vessels: Review of selected problems.* Applied Mechanics Reviews, 2008. **61**(6): p. 060801-060801-060833.

[7] B. B. Pan, W. C. Cui, Y. S. Shen, and T. Liu, *Further study on the ultimate strength analysis of spherical pressure hulls.* Marine Structures, 2010. **23**(4): p. 444-461.

[8] B. B. Pan, W. C. Cui, and Y. S. Shen, *Experimental verification of the new ultimate strength equation of spherical pressure hulls.* Marine Structures, 2012. **29**(1): p. 169-176.

[9] R. Zoelly, *Ueber ein knickungsproblem an der kugelschale*. 1915, Ph.D. thesis, ETH Zurich: Zurich, Switzerland.

[10] H.-S. Tsien, *A theory for the buckling of thin shells.* Journal of the Aeronautical Sciences, 1942. **9**(10): p. 373-384.

[11] A. Kaplan and Y. Fung, *A nonlinear theory of bending and buckling of thin elastic shallow spherical shells*. 1954, National Advisory Committee for Aeronautics, Washington, DC, Technical Note 3212.

[12] R. H. Homewood, A. C. Brine, and A. E. Johnson, *Experimental investigation of the buckling instability of monocoque shells.* Experimental Mechanics, 1961. **1**(3): p. 88-96.

[13] L. Seaman, *The nature of buckling in thin spherical shells*. 1962, WATERTOWN ARSENAL LABS MA.

[14] M. A. Krenzke and T. J. Kiernan, *Elastic stability of near-perfect shallow spherical shells.* AIAA Journal, 1963. **1**(12): p. 2855-2857.

[15] R. L. Carlson, R. L. Sendelbeck, and N. J. Hoff, *Experimental studies of the buckling of complete spherical shells.* Experimental Mechanics, 1967. **7**(7): p. 281-288.

[16] H. N. R. Wagner, C. Hühne, and S. Niemann, *Robust knockdown factors for the design of spherical shells under external pressure: Development and validation.* International Journal of Mechanical Sciences, 2018. **141**: p. 58-77.

[17] NASA, *Buckling of thin-walled doubly curved shells.* NASA Space Vehicle Design Criteria, NASA SP-8032, 1969.

[18] A. Y. Evkin and O. V. Lykhachova, *Energy barrier as a criterion for stability estimation of spherical shell under uniform external pressure.* International Journal of Solids and Structures, 2017. **118-119**: p. 14-23.

[19] J. W. Hutchinson and W. T. Koiter, *Postbuckling theory.* Appl Mech Rev, 1970. **23**: p. 1353-1366.

[20] J. M. T. Thompson and G. H. M. v. d. Heijden, *Quantified "shock-sensitivity" above the maxwell load.* International Journal of Bifurcation and Chaos, 2014. **24**(03): p. 1430009.

[21] D. Bushnell, *Shell buckling*. 2014. Available from: http://shellbuckling.com/index.php.

[22] T. von Kármán and H.-S. Tsien, *The buckling of spherical shells by external pressure.* Journal of the Aeronautical Sciences, 1939. **7**(2): p. 43-50.

[23] T. von Kármán and H.-S. Tsien, *The buckling of thin cylindrical shells under axial compression.* Journal of the Aeronautical Sciences, 1941. **8**(8): p. 303-312.

[24] W. T. Koiter, *On the stability of elastic equilibrium*. 1945, Polytechnic Institute of Delft: Delft, The Netherlands. (An English translation is available as NASA Tech. Trans. F 10833, 1967.)

[25] T. Koga and N. J. Hoff, *The axisymmetric buckling of initially imperfect complete spherical shells.* International Journal of Solids and Structures, 1969. **5**(7): p. 679-697.

[26] R. Kao, *A note on buckling of spherical caps with initial asymmetric imperfections.* Journal of Applied Mechanics, 1972. **39**(3): p. 842-844.
[27] L. H. Donnell, *A new theory for the buckling of thin cylinders under axial compression and bending.* Aeronaut Eng-Trans ASME, 1934. **56**(11): p. 795-806.
[28] L. H. Donnell and C. C. Wan, *Effect of imperfections on buckling of thin cylinders and columns.* J of Applied Mech, 1950. **17**: p. 73-83.
[29] R. Kao and N. Perrone, *Asymmetric buckling of spherical caps with asymmetrical imperfections.* Journal of Applied Mechanics, 1971. **38**(1): p. 172-178.
[30] Q. S. Fan, *Post-buckling behaviour and imperfection sensitivity of spherical shells based on nonlinear elastic stability theory.* Thin-Walled Structures, 1989. **8**(1): p. 1-18.
[31] J. Błachut and G. D. Galletly, *Influence of local imperfections on the collapse strength of domed end closures.* Proceedings of the Institution of Mechanical Engineers, Part C: Journal of Mechanical Engineering Science, 1993. **207**(3): p. 197-207.
[32] J. Błachut, *Locally flattened or dented domes under external pressure.* Thin-Walled Structures, 2015. **97**: p. 44-52.
[33] J. Błachut, *Buckling of composite domes with localised imperfections and subjected to external pressure.* Composite Structures, 2016. **153**: p. 746-754.
[34] A. Lee, F. López Jiménez, J. Marthelot, J. W. Hutchinson, and P. M. Reis, *The geometric role of precisely engineered imperfections on the critical buckling load of spherical elastic shells.* Journal of Applied Mechanics, 2016. **83**(11): p. 111005-111005-111011.
[35] J. W. Hutchinson, *Buckling of spherical shells revisited.* Proceedings of the Royal Society A: Mathematical, Physical and Engineering Sciences, 2016. **472**(2195): p. 20160577.
[36] J. Paulose and D. R. Nelson, *Buckling pathways in spherical shells with soft spots.* Soft Matter, 2013. **9**(34): p. 8227-8245.
[37] N. P. Bende, A. A. Evans, S. Innes-Gold, L. A. Marin, I. Cohen, R. C. Hayward, and C. D. Santangelo, *Geometrically controlled snapping transitions in shells with curved creases.* Proceedings of the National Academy of Sciences, 2015. **112**(36): p. 11175-11180.
[38] A. Lee, P. T. Brun, J. Marthelot, G. Balestra, F. Gallaire, and P. M. Reis, *Fabrication of slender elastic shells by the coating of curved surfaces.* Nature Communications, 2016. **7**: p. 11155.
[39] M. Pezzulla, S. A. Shillig, P. Nardinocchi, and D. P. Holmes, *Morphing of geometric composites via residual swelling.* Soft Matter, 2015. **11**(29): p. 5812-5820.
[40] J. L. Sanders, *Nonlinear theories for thin shells.* Quarterly of Applied Mathematics, 1963. **21**(1): p. 21-36.
[41] W. T. Koiter. *General equations of elastic stability for thin shells*. In *Proceedings, Symposium on the Theory of Shells to Honor Lloyd Hamilton Donnett*. 1967.
[42] W. T. Koiter, *On the nonlinear theory of thin elastic shells.* Proc Koninkl Ned Akad van Wetenschappen, Series B, 1966. **69**: p. 1-54.
[43] B. Budiansky, *Notes on nonlinear shell theory.* Journal of Applied Mechanics, 1968. **35**(2): p. 393-401.
[44] F. I. Niordson, *Shell theory*. North-holland series in applied mathematics and mechanics ; v 29. 1985, New York: Elsevier Science Pub. Co.
[45] W. T. Koiter and A. M. A. van der Heijden, *W.T. Koiter's elastic stability of solids and structures*. 2009, Cambridge ;: Cambridge University Press.

[46] E. Riks, *An incremental approach to the solution of snapping and buckling problems.* International Journal of Solids and Structures, 1979. **15**(7): p. 529-551.
[47] M. Taffetani, X. Jiang, D. P. Holmes, and D. Vella, *Static bistability of spherical caps.* Proceedings of the Royal Society A: Mathematical, Physical and Engineering Sciences, 2018. **474**(2213): p. 20170910.
[48] M. Gomez, D. E. Moulton, and D. Vella, *Dynamics of viscoelastic snap-through.* Journal of the Mechanics and Physics of Solids, 2019. **124**: p. 781-813.
[49] J. Vieira, J. M. A. Osório, S. Mouta, P. Delgado, A. Portinha, J. F. Meireles, and J. A. Santos, *Kansei engineering as a tool for the design of in-vehicle rubber keypads.* Applied Ergonomics, 2017. **61**: p. 1-11.
[50] B. Audoly and J. W. Hutchinson, *Localization in spherical shell buckling.* Journal of the Mechanics and Physics of Solids, 2019: p. https://doi.org/10.1016/j.jmps.2019.103720.

Link between chapter 2 and chapter 3

The previous chapter has introduced a large axisymmetric imperfection and investigated its effects on the buckling of a pressurized hemispherical shell. Among the insights gained from this investigation, a number of them have stood out for application in soft robotics. In particular, imperfect shells with buckling modes 3 and 4 can undergo a large volume change before the attainment of the maximum pressure. These types of response are advantageous for applications involving large volume change as well as energy storage and release. In the next chapter, we capitalize on these insights and focus on the application of this type of imperfect shell to elicit in a soft valve a novel function for soft robotic applications. Therein we investigate the performance of a bi-shell valve, which can harness shell snapping interaction between an imperfect shell and a shallow spherical cap. The goal is to translate a slow volume input into a fast volume output for the rapid actuation of soft pneumatic robots.

Chapter 3

Bi-shell valve for fast actuation of soft pneumatic actuators via shell snapping interaction

Chapter 3: Bi-shell valve for fast actuation of soft pneumatic actuators via shell snapping interaction

*Chuan Qiao, Lu Liu, Damiano Pasini**

Department of Mechanical Engineering, McGill University, Montreal, Quebec H3A 0C3, Canada

Advanced Science, 2021, 2100445. https://doi.org/10.1002/advs.202100445

3.1 Abstract

Rapid motion in soft pneumatic robots is typically achieved through actuators that either use a fast volume input generated from pressure control, employ an integrated power source, such as chemical explosions, or are designed to embed elastic instabilities in the body of the robot. This paper presents a bi-shell valve that can fast actuate soft actuators neither relying on the fast volume input provided by pressure control strategies nor requiring modifications to the architecture of the actuator. The bi-shell valve consists of a spherical cap and an imperfect shell with a geometrically tuned defect that enables shell snapping interaction to convert a slowly dispensed volume input into a fast volume output. This function is beyond those of current valves capable to perform fluidic flow regulation. Validated through experiments, our analysis unveils that the spherical cap sets the threshold of the snapping pressure along with the upper bounds of volume and energy output, while the imperfect shell interacts with the cap to store and deliver the desired output for rapid actuation. Geometry variations of the bi-shell valve are provided to show that the concept is versatile. A final demonstration shows that the soft valve can quickly actuate a striker.

3.2 Introduction

Pneumatic soft robotics is a rapidly evolving field of research that promises to expand the scope of current robotic applications. Distinct from classical rigid body robots, their pneumatic soft counterparts are typically fabricated from soft materials, e.g. elastomers [1, 2], that can undergo large deformations to accomplish complex tasks. A diverse range of input sources are typically used to drive their motion; some resort to internal pressurized air [3-5], and others to external propellers, such as roller modules [6] or moveable bodies [7]. Functions that have been realized span a broad spectrum of motion, from locomotion, including galloping [8], swimming [9], crawling [10], and climbing [11-13], to manipulation, such as gripping [14, 15], stirring [16], and swallowing [7]. An advantage offered by soft robots is that their elastic modulus is similar to that of soft biological tissues, imparting in them the ability to easily adapt to the local profile of adjacent objects, and making them suitable for applications that involve delicate interactions with humans [17, 18], the handling of fragile objects [14] and the adaptation to unknown environments [5]. Pneumatic soft robots do not always require a complex control system of actuators, sensors and control algorithms, as rigid body robots typically do; rather their working principle is to achieve control mainly in a passive way, through either the tuning of the robot body compliance [1, 19, 20] or the integration of a complex internal fluidic circuit [21-24]. Others of their advantages include low mass and cost, high cycle life, availability at small length scales, and damage resistance to impact [2, 25-27].

Key to actuating fluidic soft robots is to have an effective strategy that can power motion and enable complex movements. The most widely used method is pressure control, applied successfully to trigger motion of soft robots of various size [4, 26, 28]. With this strategy, actuation can be rapid and inflation can occur at high speed through the delivery of high pressure low viscosity air [4, 15], and/or by further optimizing the actuator design with the outcome of reducing the amount of air required for actuation [26]. While effective, pressure-controlled actuation has a twofold drawback. First, for pressure generation and control, it requires a bulky pneumatic system that typically includes a pressure supply (e.g. air pumps or compressed gas tanks) and a set of hard valves (e.g. pressure regulators and solenoid valves). Secondly, fine control over the change in volume is difficult to achieve. For a soft robot, this might pose a problem. If motion is driven by the emergence of unstable events, the soft robot might lose its capacity to function properly. For example, a spherical cap embedded into a soft robot that is driven by external pressure will snap from the initial to its fully everted configuration, leaving no chance to access any intermediate states of deformation [29]; if motion requires operation at these states, the soft robot will inevitably fail to do so.

An alternative to pressure-controlled actuation is volume control. This strategy allows for direct adjustment of the volume change. For example, a syringe pump can be used to dispense a precise volume of a fluid into the soft robot, and its pressure-volume response can be registered [29-33]. Besides this advantage, controlling the output volume avoids any jumps in displacement that a pressure control strategy would impose upon snap-through buckling. Volume control strategies used so far, however, have a common drawback; they are unable to drive fast actuation, a limitation ascribed to the limited flow rate that a syringe pump can typically deliver. Only a handful of attempts have been successful to circumvent this issue, and all of them have been devoted to the design of actuators. Their strategy has been to integrate snap-through instability of spherical caps [31] or balloons [32] into the architecture of the actuator.

Besides pressure-controlled and volume-controlled actuation, other actuation methods used in the literature resort to external manipulation [6, 7], dielectric elastomers [34-37], evaporation of low-boiling point fluids [38], chemical decomposition [23], and explosive chemical reaction [39-42]. Their application to soft robots has so far shown to be limited due to the additional components they require, including external mechanisms for manipulation, electrical circuits for dielectric elastomers, heaters for low-boiling point fluids, and integrated systems for chemical decomposition and combustion.

Pneumatic soft robots typically resort to elements other than actuators to operate. One of them is valves. Their function so far has been other than that of actuators. Current valves can control the fluid flow spreading throughout the body of a soft robot. Some concepts comprise rigid elements that can provide a simple and unambiguous control of a fluid flow. Others achieve this function by engaging elastic instabilities, e.g. wrinkling, snapping, and creasing, in their constituents. Sources used to initiate elastic instabilities include air pressure supply, external force, and viscous flux through unstable-arch channels. In all cases, the fluid-control function these valves perform is binary, switching between two distinct states. For example, a spherical cap embedded in the valve has been shown effective to snap from one position to either block or unlock the flow in its internal tubes [29]. Another valve architecture exploits the snapping of an elastic arch embedded in a fluid flow to act as a passive microfluidic fuse that regulates the flow present in its rigid-walled channels [43]. Manifold applications exist for soft valves ranging from soft ring oscillators [44] to pneumatic logic gates [22] and soft kink valves [45]. All the existing implementations can only either fully (on-off control) or partially (binary flux control) block a fluid flow for contunuous operation, but cannot provide an impulse for fast actuation under volume control.

In this work, we introduce a bi-shell valve that can provide volume-controlled rapid actuation to soft actuators. The valve does not resort to the fast volume input typically generated through pressure control strategies [4, 15], nor to any modifications to the body of the actuator that require chemical explosion [39-42] or elastic instability [31, 32, 36, 37]. The valve engages snapping and shell interaction to generate a fast volume output upon a slow volume input. Our bi-shell valve can thus perform a function that is unattainable by existing soft valves. It has the following merits for soft robotics: (i) *Ready for use with volume control*. Common soft actuators can directly use this valve to achieve rapid motion under volume control, without any additional modifications to the body of the actuator. (ii) *Output performance attuning*. The amount of fast volume output can be set in a fully passive way by simply programming the geometry of the constituent shells and their defects to maximize the valve performance and satisfy the functional requirements of a given soft robot. (iii) *Retainment of pre-snapping geometry*. The volume output of the valve is negligible before snapping, thus enabling the soft actuator connected to our valve to preserve its initial undeformed state. (iv) *Inlet flow rate insensitivity*. The fast volume output is not sensitive to the flow rate at the valve inlet, as the output is generated from the air transfer between the constituent shells during snapping. In the following sections, we first study the snapping and interaction between the elastic shells of our bi-shell valve to understand the role that each of them plays during deflation. We then characterize the response of each shell within a wide geometric space and map the range of fast volume outputs our bi-shell valve can achieve. Finally, we demonstrate the application of our bi-shell valve to thrust the motion of an object along a guided track.

3.3 Results and discussion

3.3.1 The bi-shell valve concept: tapping into shell snapping interaction

Our bi-shell valve consists of two interacting elastic shells that cooperate upon snapping to generate a rapid change in volume in response to a slow volume input. Figure 3-1A shows the bi-shell valve concept in its undeformed state. Beneath the shells, an input chamber connecting the shell inner volumes provides deflation under volume control as well as pressure control, if required. On the left-hand side is a perfect spherical cap which exhibits an unstable response, typical of elastic thin shells with a high peak of pressure attained in the nearly undeformed state, followed in turn by a rapid fall of pressure into a plateau leading to full eversion [46]. On the right-hand side is a hemispherical shell featuring a large axisymmetric imperfection in the form of an elliptical arc traced away from the pole. We select this imperfect shell for its stable response over a large change in volume that can be effectively tuned by the geometry of the imperfection, thus attaining a capacity to provide increasing pressure resistance [47]. The bi-shell valve operates through a slow deflation (negative pressure) imparted by the inlet of the input chamber and delivers a fast deflation via the outlet at the output chamber. Since the pressure of the bi-shell valve remains negative during the operation, we have made here the assumption of neglecting the negative sign for the convenience of the analysis.

By combining the two shell architectures, a perfect spherical cap and an imperfect shell, each with its own distinct response, into one bi-shell system (Figure 3-1A), we can program the mechanism of deformation, impart a desired sequence of deflation, and code the global performance of our valve. Our goal is to capitalize on shell snapping interaction to generate a function that adds to the control-flow function of existing soft valves that would be otherwise unattainable through current concepts involving either snapping of a single spherical cap or other strategies.

We start with a description of the qualitative response of the system deformation. Figure 3-1B illustrates that a slow deflation of the input chamber through the inlet (ΔV_{in}), brings each shell into different states. At the onset of deflation (light green), the pole of the imperfect shell deforms downward smoothly without snapping from the initial state to state (i), whereas the perfect cap barely undergoes any deformation, hence retaining its initial state (hidden line overlaid on light-green solid line). There is no snapping during these stages because snapping is triggered by the buckling of the spherical cap. After snapping (dark green), the imperfect shell springs back from state (i) to state (ii), whereas the spherical cap everts downward from its initial upward position.

To capture the snapping behavior in quantitative terms, we determine the pressure-volume response of the bi-shell valve. We first assess how the volume change of the input chamber governs the pressure of the input chamber, and then normalize these values respectively by the buckling pressure $P_C = 2E(t/R)^2/\sqrt{3(1-\nu^2)}$ and the enclosed volume $V_0 = 2\pi R^3/3$ of a baseline hemispherical shell with radius identical to the radius R on the bottom plane of the constituent shell. These metrics are the characteristic axes of the plot reported in Figure 1C. While deflation can be expected to generate negative values of both volume and pressure, here we consider their signs as positive for the convenience of the analysis. The portion of the curve up to (i) describes the initial deformation prior to snapping when the pressure hits the snapping pressure p_i. A further deflation triggers a snap-through instability with a configurational change in both shells, now reaching simultaneously their second state (ii) of equilibrium. The process is characterized by a drop of pressure to p_{ii} with the spherical cap eversion synchronous to the snap back of the imperfect shell. Since the outer side of the former shell is enclosed by the output chamber, its downward snapping produces a rapid change in volume (yellow area ΔV^*, Figure 3-1B), which is bounded by the pre- and post-snapping states of the spherical cap in the output chamber. The hallmark of this concept is that the release of volume to slow deflation is fast and would be otherwise inaccessible by employing either shell individually, as shown later. As per the energy and volume change in the input chamber, the snapping event causes a release of the previously stored elastic energy in both shells (ΔU^*) but with almost no change in volume (less than 0.54% of the total volume); this outcome is due to the extremely small difference in pressure (less than 550 Pa) between the input chamber and the atmosphere (See Supporting Information for details).

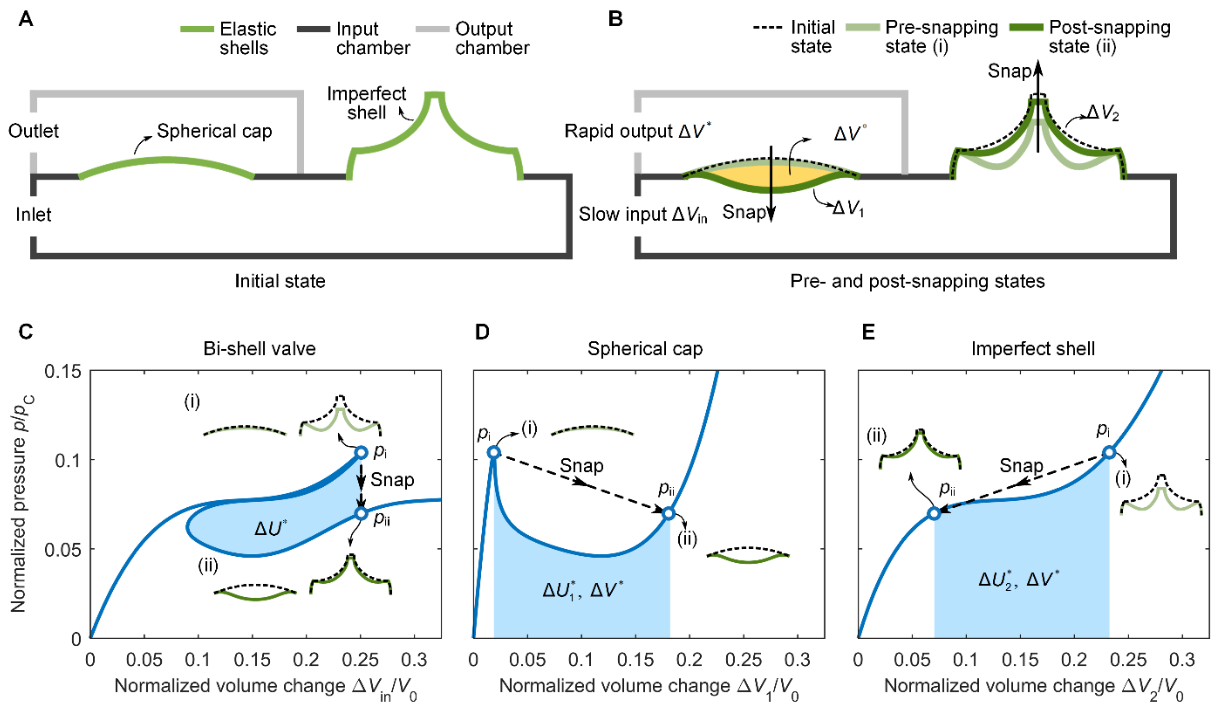

Figure 3-1 Bi-shell valve with snap-through response under volume control. (A) Schematic of the bi-shell system in its unloaded state; the valve comprises two thin elastomeric shells, one with perfect and the other with imperfect spherical geometry, connected through an input chamber (below both) and output chamber (above the spherical cap). (B) Pre and post snapping states of the bi-shell valve under incremental deflation ΔV_{in} . Prior to instability (light green) the spherical cap is almost locked in its initial shape yielding no change in volume ΔV_1 as opposed to its imperfect counterpart, which can deform downward smoothly without snapping from the initial state to state (i) and store elastic energy due to its compliance with an accrued change in volume ΔV_2 . There is no snapping during theses stages because the instability is triggered by the buckling of the spherical cap. Upon snapping (dark green), the former bounces down to its buckled shape with a volume change of ΔV^*, whereas the latter springs up from state (i) to state (ii) with a release of ΔV^*. In yellow is the resulting ΔV^*, i.e. the volume difference between pre (i) and post (ii) snapping states, which describes the rapid change in volume generated by the snapping of the spherical cap. (C to E) Pressure-volume responses of the entire bi-shell system (C), the spherical cap solely (D), and the imperfect shell only (E). The normalization factors of pressure and volume are the buckling pressure $P_{\text{C}} = 2E\left(t/R\right)^2 / \sqrt{3\left(1-\nu^2\right)}$ and enclosed volume $V_0 = 2\pi R^3/3$ of a baseline hemispherical shell with radius identical to the radius R on the bottom plane of the constituent shells.

3.3.2 Inferring the bi-shell valve behaviour from the individual response of each shell

As described above, the deformation of our bi-shell system (Figure 3-1C) is the result of the collective response of the constituent shells, each cooperating distinctly during deflation and snapping. To understand the interaction between them and each of their roles, here we examine each shell separately, investigate their individual responses when deflated separately, and correlate them to the system behavior.

Figure 3-1D pertains to the spherical cap on its own, and Figure 3-1E to the imperfect shell on its own. The former (blue path in Figure 3-1D) shows the characteristic highly unstable response of a perfect elastic shell. A small volume change ($\Delta V_1 / V_0 < 0.02$) makes the pressure quickly escalate to a high critical value ($p / p_{\mathrm{C}} = 0.104$, p_{i}), which immediately drops to a lower plateau ($p / p_{\mathrm{C}} = 0.05$), spanning a wide range of volume change ($0.05 < \Delta V_1 / V_0 < 0.2$). After the plateau, the pressure increases rapidly again. There is no limit point in volume because the spherical cap selected here is thick and shallow, similar to the findings of Gorissen et al. [31]; the elements that are here important to trigger snapping are the initial peak in pressure, the subsequent softening, and a final increase in pressure as noted by Overvelde et al. [32]. The latter shell of our valve exhibits a stable pressure response (blue path in Figure 3-1E) over an increasing volume change ΔV_2 , and its buckling mode is enabled by the size and location of the imperfection (see Supporting Information for details). The pressure-volume path (blues) has three portions: an initial rapid increase of pressure for small values of the volume change ($\Delta V_2 / V_0 < 0.1$), followed by a stable plateau offering a gradual increase of pressure for intermediate values of $\Delta V_2 / V_0$, and finally a steep increase of pressure. While the blue paths in Figure 3-1C, 3-1D and 3-1E represent the static equilibrium responses of each system, the black hidden ones with arrow mark the direction from the pre to the post snapping state.

Once the individual shells join through the input chamber, a concerted deformation (Figure 3-1C) takes place to ensure equilibrium of volume and pressure. Equilibrium requires the balance of their pressure in the stable post-snapping state (see Supporting Information). The conservation of volume requires the input volume change ΔV_{in} to equal the sum of the volume changes of the individual shells, ΔV_1 and ΔV_2 [32, 33, 48, 49]. The onset of snapping is mainly controlled by the spherical cap, which upon winning the critical pressure p_i, cannot accommodate any further increase in pressure, resulting in a sudden drop of pressure due to its elastic instability (Figure 3-1D). It is this event that triggers the snapping of both shells (black paths in Figure 3-1C, 3-1D and 3-1E). Each shell springs into its own snapped state in a swift manner. During snapping, the spherical cap collapses due to its reduced pressure resistance and propels the air in the input chamber towards the adjacent shell for an upward push; the sudden deflation of the former inflates the latter.

As with other forms of elastic deformation, during snapping each shell can store and release elastic energy (cyan areas in Figure 3-1), and their amounts correlate with those of the entire system. In particular, the deflation of the spherical cap by a volume change ΔV^* is accompanied by the storage of elastic energy ΔU_1^* (Figure 3-1D), while the inflation of the imperfect shell by a volume of ΔV^* corresponds to the elastic energy release ΔU_2^* (Figure 3-1E). The difference between them, $\Delta U^* = \Delta U_2^* - \Delta U_1^*$, is the elastic energy released by the bi-shell valve due to the snapping of both constituents (Figure 3-1C), a notion consistent with the existing literature [31-33, 48, 49]. In addition, we note that the energy stored by both shells in the linear portion of the pressure-volume curves is not considered here because it does not contribute to the energy output during snapping.

3.3.3 Experimental investigation

Figure 3-2A shows our bi-shell valve fabricated with two thin shells (green) made out of Zhermack Elite Double 32 (Zhermack, Italy), along with acrylic input (painted in black) and output (transparent) chambers (see Supporting Information for details). Figure 3-2B and C illustrate the mechanism of deformation at two sequential instants (pre and post snapping) upon deflation, with configurations that parallel those shown in Figure 3-1. In the imperfect shell, an axisymmetric mode of deformation first accrues until state (i) is reached, while the spherical cap holds its undeformed shape under initial pressure reduction (Figure 3-2B). Further deflation causes both shells to snap into distinct states (ii), the imperfect shell nearly springing upward to its initial configuration and the perfect shell buckling downward (Figure 3-2C and Movie S1, Supporting Information).

Figure 3-2D to F show the pressure-volume change curves obtained from both our analyses and experiments (see Supporting Information for details). The responses on all fronts, i.e. bi-shell valve, spherical cap, and imperfect shell, show a snapping behavior matching those in Figure 3-1C to E. In Figure 3-2D, the experimental pressure of the input chamber (blue curve) first increases smoothly upon air deflation until state (i) ($\Delta V_{\mathrm{in}} / V_0 = 0.32$), and then plunges from $p_{\mathrm{i}} / p_{\mathrm{C}} = 0.128$ to $p_{\mathrm{ii}} / p_{\mathrm{C}} = 0.064$. Here, the experimental results confirm that the drop in pressure is triggered by the snapping of the spherical cap, which collapses downward (Figure 3-2C). The prediction of our numerical simulation (red curve) agrees with the experimental results, with the predicted pre- and post-snapping states (i) and (ii) resembling those of their experimental counterparts as quantified below.

While the volume change and energy output of the bi-shell valve cannot be directly calculated from the experimental curve (pressure-volume change) in Figure 3-2D, we can still estimate their values through the separate response of their elastic constituents, i.e. spherical cap and imperfect shell (blue curves in Figure 3-2E and F). The post-snapping pressure is determined through the equilibrium condition the two shells should satisfy at $p_{\mathrm{ii}} / p_{\mathrm{C}} = 0.062$ (Figure 3-2E to F), which is close to the value, $p_{\mathrm{ii}} / p_{\mathrm{C}} = 0.064$, from our experimental result in Figure 3-2D. The relative error between the estimated and measured post-snapping pressure is below 4%, demonstrating the accuracy of our estimation. From state (i) to state (ii), the volume change due to snapping is then obtained from the separate response of each shell as $\Delta V^* / V_0 = 0.154$, while the energy output is $\Delta U^* / \left(p_{\mathrm{C}} V_0 \right) = 3.57 \times 10^{-3}$. Our analysis provides an accurate prediction of the valve response, described by a volume change of $\Delta V^* / V_0 = 0.135$ and a released energy of $\Delta U^* / \left(p_{\mathrm{C}} V_0 \right) = 3.63 \times 10^{-3}$. To minimize the error between numerical and experimental results, we employ a realistic model that accounts for any non-uniformity of shell thickness caused by manufacturing as well as for the initial deformation due to clamping (see Supporting Information for details). The discrepancy, especially at larger strains, is attributed to imperfections in shell geometry that emerge during fabrication. This might include geometric deviation of the mold from the nominal design, as well as defects in the base material, such as microvoids.

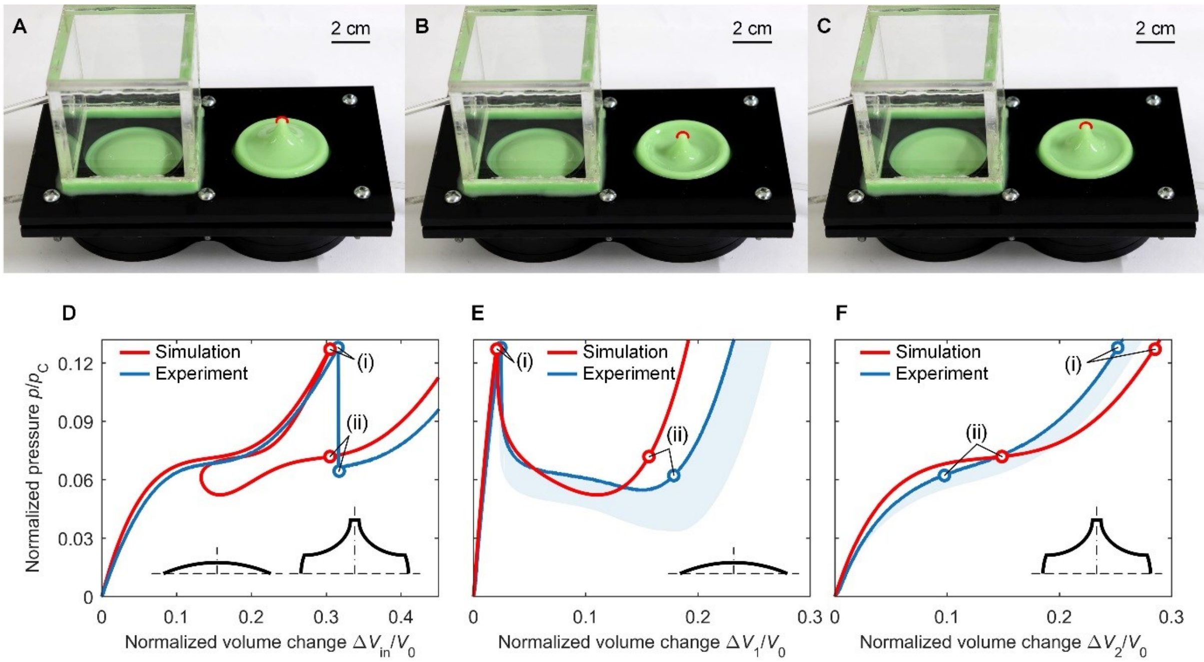

Figure 3-2. Experiment of the bi-shell valve. Photographs of bi-shell valve: (A) initial state, (B) state (i) before snapping, and (C) state (ii) after snapping. The top of the imperfect shell is outlined with a red cap to emphasize the difference between states. (D to F) Pressure-volume responses of the input chamber, the spherical cap, and the imperfect shell. P_C is the theoretical critical pressure of a perfect spherical shell and V_0 is the volume of a hemisphere. The cyan domains in (E) and (F) show the envelope of the experimental response of three tested samples.

The results from both analyses and experiments (Figure 3-1 and 3-2) reveal that shell interaction governs the bi-shell valve behavior, which in turn can be retrieved by combination of the individual shell response. These insights not only enable us to understand the role of each shell during snapping, but also provide principles for valve design involving multiple shells. We propose a two-steps approach (see Figure 3-21 for a flowchart of the design process, Supporting Information), where the bi-shell performance is defined by 4 metrics: the upper bounds of volume and energy, $\Delta V^*_{\text{upper}}$ and $\Delta U^*_{\text{upper}}$, as well as the working ranges of ΔV^* and ΔU^*, i.e. the variation of volume change and released energy within their respective bounds. The first step involves examining the spherical cap only, which sets the valve performance limits, and aims at determining the upper bounds ($\Delta V^{*}_{\mathrm{upper}}$ and $\Delta U^{*}_{\mathrm{upper}}$) of the valve output. These bounds set the upper boundaries for the bi-shell valve performance, i.e. the bi-shell system with a given spherical cap cannot exceed them for any geometric scenario of the imperfect shell. In the second step, we determine the attainable ranges of volume change ΔV^{*} and released energy ΔU^{*} for the bi-shell by exploring the design space of the imperfect shell for a prescribed geometry of the spherical cap. With this approach, we can ensure that we reach the full potential of both shells, thereby yielding a valve output close to the achievable maximum.

3.3.4 Upper bounds of volume change and released energy

The goal is to find the first two performance metrics of our bi-shell valve, i.e. the maximum values of volume change, $\Delta V^{*}_{\mathrm{upper}}$, and released energy, $\Delta U^{*}_{\mathrm{upper}}$, our bi-shell valve can attain. As described earlier, the spherical cap sets the upper performance limit of our bi-shell valve, and is studied here as standalone shell. The modified Riks method is employed to simulate the deflation of a spherical cap subject to uniform pressure and parametrically map $\Delta V^{*}_{\mathrm{upper}}$ and $\Delta U^{*}_{\mathrm{upper}}$ upon snapping. The parameters defining the spherical cap geometry (inset in Figure 3-3) are the radius in the base plane ($R = 25\ \mathrm{mm}$), the normalized thickness (varying between $t_1/R = 0.01$, and 0.1), and the normalized height (ranging from $h/R = 0.1$ to 0.5).

Figure 3-3A shows a representative curve of pressure versus volume change for a perfect spherical cap. The end point (light green) of the pre-snapping path denotes the pressure peak p_{i} (state (i)), which is typically above the end point of the post-snapping path (dark green designating state (ii)) at p_{ii}. As shown in Figure 3-1C to E, the drop of pressure from p_{i} to p_{ii} represents the reduction in pressure resistance offered by the imperfect shell. The position of state (ii) depends on shell interaction, and can be at any point along the post-snapping curve in Figure 3-3A, even at sites approaching state (iii). If snapping brings state (ii) to coincide with state (iii) (red point), then the volume change and the stored energy of the spherical cap reach the maximum values, $\Delta V^{*}_{\text{upper}}$ and $\Delta U^{*}_{1(\text{upper})}$ (Figure 3-3A), which are the upper bounds illustrated in Figure 3-3A respectively in the lower part and in cyan. At this state, the energy released by the bi-shell valve, $\Delta U^{*}_{\text{upper}}{=}p_{\text{i}}\Delta V^{*}_{\text{upper}}-\Delta U^{*}_{1(\text{upper})}$, also reaches the upper bound, (see Supporting Information for details). $\Delta V^{*}_{\text{upper}}$ and $\Delta U^{*}_{\text{upper}}$ describe an ideal scenario for bi-shell valve where the pressure of the imperfect shell is insensitive to snapping, i.e. no pressure drop is developed during snapping and no change in pressure takes place (see Supporting Information for details). In the following, we show that the upper bounds obtained for the perfect spherical cap can be used to characterize the output performance of our bi-shell valve as a function of the cap geometry.

To assess the snapping performance with respect to changes in shell geometry, we first define a widely used parameter of the perfect cap shape, which incorporates the dimensionless size and thickness of the spherical cap. This is $\lambda=\left(12\left(1-\nu^{2}\right)\right)^{1/4}\left(R_{1}/t_{1}\right)^{1/2}\alpha$ [50, 51], where R_1 is the radius of the spherical cap, t_1 is the thickness, α (Figure 3-3A) is the edge angle measured from the axis of symmetry, and ν the Poisson ratio. λ enables for the discrimination of areas of the design space, normalized thickness t_1/R versus normalized height h/R, with snap-through instability from those without. This is illustrated (Figure 3-3B and 3-3C) for both upper bounds of volume change and released energy. For $\lambda<1.04$ (white area in the upper left corner), the spherical cap is thick and shallow, and no snap-through takes place; here there is only shell deflation with a smooth increase of pressure that cannot generate any rapid volume change. In contrast for $\lambda>1.04$, the shell, thinner and deeper in geometry, undergoes snap-through for all combinations of t_1/R and h/R. As per the values of the upper bounds for volume change and released energy, the results in Figure 3-3B and 3-3C help to gain insights into the geometric parameters that govern the output performance of the bi-shell valve. From their contour plots, we observe that $\Delta V^{*}_{\text{upper}}$ increases monotonically with the normalized height h/R and its span is sizeable, from $\Delta V^{*}_{\text{upper}}/V_0=0$ to 0.75 (Figure 3-3B). The main implications is that a shell with higher h/R in its initial state, inherently encloses a larger inner volume, thus outlining a geometry capable of generating large change in volume upon snapping to the fully everted state. On the other hand, compared to h/R, the normalized thickness t_1/R exerts a minor influence on the volume change. As per the energy release, Figure 3-3C shows that $\Delta U^*_{\text{upper}}$ increases from $\Delta U^*_{\text{upper}}/(EV_0)=0$ to 0.004 with both h/R and t_1/R. In comparison, shells with larger h/R can generate more ample change in volume during snapping, with a larger t_1/R providing a higher pressure. The maximum released energy $\Delta U^*_{\text{upper}}/(EV_0)$ is obtained at the upper right corner of Figure 3-3C, where both h/R and t_1/R take their largest values, and both volume and pressure changes have large values.

The results in Figure 3-3B and C become useful for soft robotic applications. $\Delta V^*_{\text{upper}}$ and $\Delta U^*_{\text{upper}}$ set performance limits that apply to our bi-shell valve. h/R and t_1/R are the governing dimensionless parameters. Through the proper combination of their h/R and t_1/R, we can program the max volume change and released energy of the valve from the geometry of the cap only. For example, a sufficiently large h/R is needed to generate enough volume change and energy for soft actuators, whereas a small h/R can limit the upper bound of volume change $\Delta V^*_{\text{upper}}$ and released energy $\Delta U^*_{\text{upper}}$ to within a safety threshold, e.g. to prevent accident in human-robot interaction [52]. On the other hand, the normalized thickness t_1/R has low to mild influence on the volume change $\Delta V^*_{\text{upper}}$, but strong on the upper bound of the released energy $\Delta U^*_{\text{upper}}$.

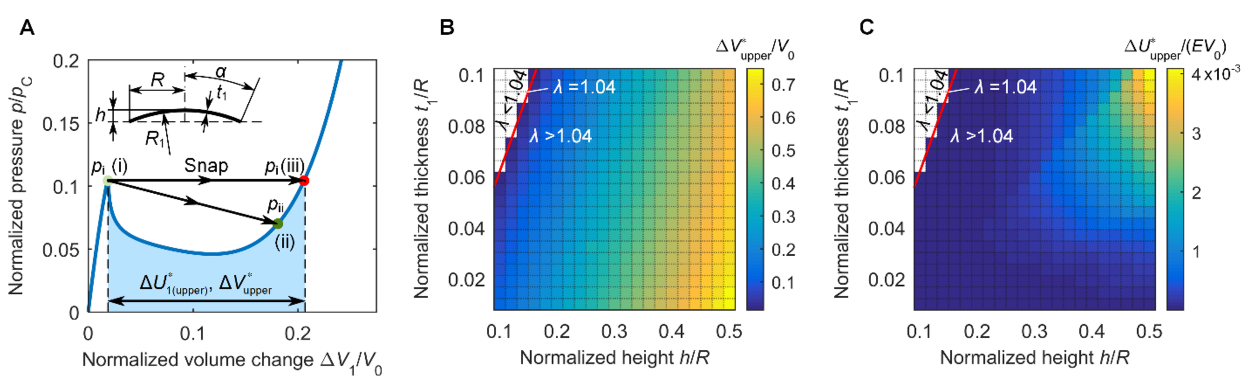

Figure 3-3. Upper bounds of performance for perfect shell limiting our bi-shell valve output. (A) Representative pressure-volume curve of a perfect spherical shell. (B) Upper bound of volume change, $\Delta V^*_{\text{upper}}/V_0$, plotted as a function of the normalized thickness t_1/R and normalized height

h/R. (C) Upper bound of released energy of the bi-shell valve, $\Delta U^*_{\text{upper}} / (EV_0)$, plotted as a function of t_1/R and h/R. $\lambda = \left(12\left(1-\nu^2\right)\right)^{1/4} \left(R_1/t_1\right)^{1/2} \alpha$ with ν the Poisson's ratio. Normalization factors of the volume change and released energy are V_0, the volume of a hemisphere with radius R, and, Young's modulus E.

3.3.5 Bi-shell valve performance in service: attainable values of volume change and released energy

While the cap snapping bounds the theoretical output of the bi-shell valve $\Delta V^*_{\text{upper}}$ and $\Delta U^*_{\text{upper}}$ (top sketch in Figure 3-4A), it is the interaction between the two shells that governs the values of volume change ΔV^* and energy ΔU^* that the bi-shell system can actually release during operation (low sketch in Figure 3-4A). Our goal here is to find this second set of metrics (ΔV^* and ΔU^*) defining our bi-shell valve performance. We do so by first prescribing the geometry of the spherical cap ($t_1/R = 0.05$, $h/R = 0.2$, and $R = 25$ mm), and then systematically exploring the design space of the imperfect shell. This step entails finding the range of ΔV^* and ΔU^* that can be obtained by varying the normalized thickness, t_2/R, within a representative span (0.02 - 0.1), and the meridional angles of the upper and lower boundaries, θ_{U} and θ_{L}, from $20°$ to $85°$, a demonstrative range that we select here for these angles.

Figure 3-4B shows the attainable volume change $\Delta V^* / \Delta V^*_{\text{upper}}$ (blue plot) and released energy $\Delta U^* / \Delta U^*_{\text{upper}}$ (orange plot) as a function of t_2/R, the normalized thickness of the imperfect shell, for given meridional angles ($\theta_{\text{U}} = 85°$ and $\theta_{\text{L}} = 20°$). Here we can identify four regimes, each yielding a distinct performance of the bi-shell valve (see Supporting Information 3.6.5 for the analysis of the buckling modes). For $t_2/R \leq 0.02$ (regime I), no snapping occurs because the imperfect shell is much more compliant than the spherical cap and collapse brings it to full eversion before the pressure is able to reach the snapping pressure of the spherical cap. For $0.02 < t_2/R < 0.035$ (regime II), the volume change ΔV^* decreases with t_2/R from 81% to 47%

of the upper bound $\Delta V^{*}_{\text{upper}}$, and the released energy ΔU drops from 59% to 16% of the upper bound $\Delta U^{*}_{\text{upper}}$. Within this range, the minimum values of ΔV and ΔU are low compared to the upper bounds generated by the spherical cap; this implies that the imperfect shell can only trigger a small portion of $\Delta V^{*}_{\text{upper}}$ and $\Delta U^{*}_{\text{upper}}$. On the other hand, in regime III ($0.035 < t_2 / R < 0.055$), both the volume change and released energy of the bi-shell valve increase rapidly with t_2/R. The volume change ranges from $\Delta V^{*}/\Delta V^{*}_{\text{upper}} = 0.49$ to 0.87 and the released energy ($\Delta U^{*}/\Delta U^{*}_{\text{upper}}$) spans the range 0.16 - 0.70. A further increase in t_2/R (regime IV) leads to an abrupt drop in both volume change and released energy, followed by a plateau that gradually approaches the value of zero. For these shells, snapping offers very modest volume change and released energy.

If the meridional angles, θ_{U} and θ_{L}, are both considered as design parameters, then a larger design space emerges for both $\Delta V^{*}/\Delta V^{*}_{\text{upper}}$ and $\Delta U^{*}/\Delta U^{*}_{\text{upper}}$. This is shown respectively in Figure 3-4C and 3-4D. Here the normalized thickness is prescribed to the value $t_2 / R = 0.05$ to ensure that $\Delta V^{*}/\Delta V^{*}_{\text{upper}}$ and $\Delta U^{*}/\Delta U^{*}_{\text{upper}}$ can take the largest output depicted in Figure 3-4B. In terms of volume change $\Delta V^{*}/\Delta V^{*}_{\text{upper}}$, the yellow upper left corner in Figure 3-4C indicates large values, whereas the other regions in blue show a modest volume change $\Delta V^{*}/\Delta V^{*}_{\text{upper}}$ almost close to zero. For $\theta_{\text{L}} \le 33°$, we find that the volume change $\Delta V^{*}/\Delta V^{*}_{\text{upper}}$ first increases slowly with the upper meridional angle θ_{U} until an abrupt increase from $\Delta V^{*}/\Delta V^{*}_{\text{upper}} = 0.3$ to 0.9 appears at $\theta_{\text{U}} = 78.5°$. With further increase in θ_{U}, the volume change $\Delta V^{*}/\Delta V^{*}_{\text{upper}}$ stays almost constant for the plotted range $\theta_{\text{U}} \le 85°$. As per the released energy, Figure 3-4D shows a contour plot similar to that of the volume change (Figure 3-4C). For $\theta_{\text{L}} \le 33°$, an abrupt increase of released energy from $\Delta U^{*}/\Delta U^{*}_{\text{upper}} = 0.15$ to 0.83, the maximum, appears at $\theta_{\text{U}} = 78.5°$. A further increase in θ_{U}, however, yields reduced values of the released energy, as opposed to $\Delta V^{*}/\Delta V^{*}_{\text{upper}}$ which remains almost constant for $\theta_{\text{U}} \ge 78.5°$. As with Figure 3-4B, the maximum values of the volume change ΔV^{*} and released energy ΔU^{*} in Figure 3-4C and 3-4D can only be attained in a narrow design space (yellow) of the imperfect shell. This zone is key to maximize the valve output, i.e. to release a large amount of energy. Its extent is governed by the interaction between the spherical cap and the imperfect shell. In particular, this yellow zone describes bi-shell valves in which the plateau pressure of the imperfect shell is located between the pre and post-snapping pressure p_{i} and p_{ii} of the spherical cap (See Supporting Information for further details).

In summary, the upper bounds ($\Delta V^{*}_{\mathrm{upper}}$ and $\Delta U^{*}_{\mathrm{upper}}$) in Figure 3-3 and the valve outputs (ΔV^{*} and ΔU^{*}) in Figure 3-4 provide guidelines of practical use for the design of our bi-shell valve. First, the upper bounds in Figure 3-3 can guide the selection of the spherical cap that has the potential to generate a proper valve output. Second, for a given spherical cap, Figure 3-4 (along with Figure 3-18, Supporting Information) summarizes the range of valve output that can be tuned with the geometry of the imperfect shell as well as identifies distinct regimes of buckling modes. In this case, despite the size of the design space, only a small window is available for the imperfect shell (yellow area in the upper left corner of Figure 3-4C and 3-4D) to generate a valve output that is close to the upper bound. The insights here gained point out that $\theta_{\mathrm{U}} = 85.9°$ and $\theta_{\mathrm{L}} = 20°$ are among the best geometric parameters of the imperfect shell that can elicit the large volume change that we observe in our experiments (Figure 3-2 and Movie S1, Supporting Information). While the results in Figure 3-4 mapping the geometric role of the imperfect shell are for a specific geometry of the spherical cap, our analysis can be straightforwardly applied to spherical caps with other geometries; this merely requires updating the spherical cap geometry and replot the bi-shell valve performance of Figure 3-4.

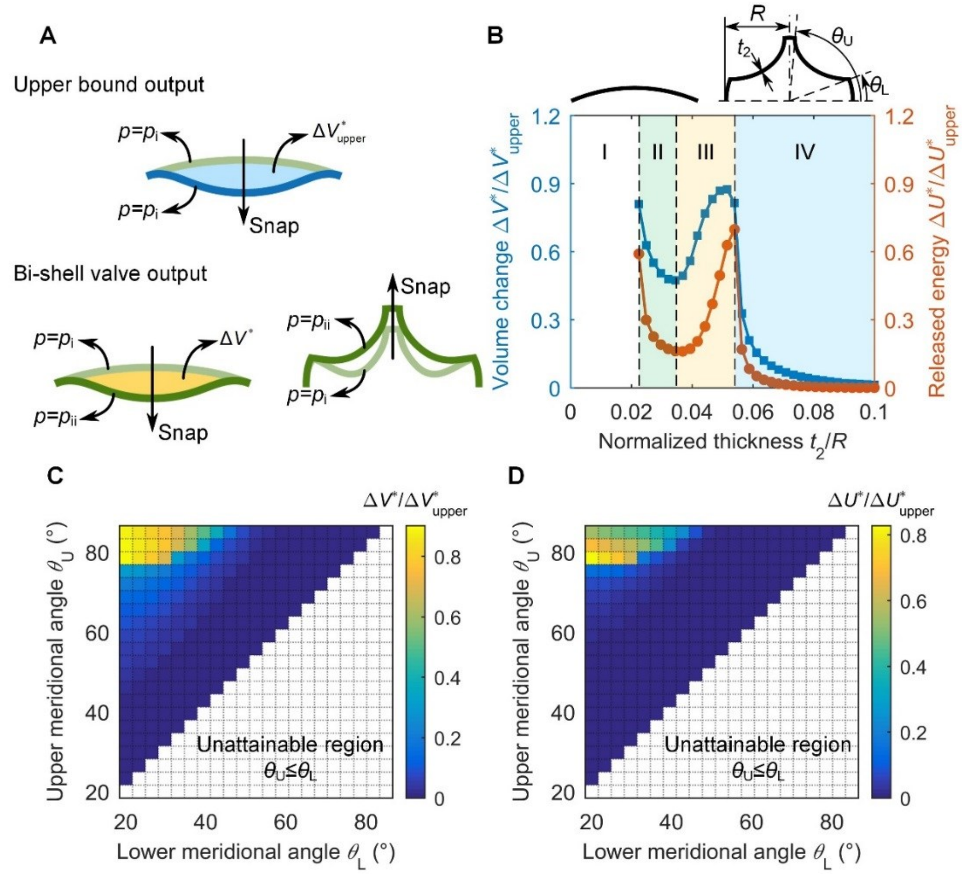

Figure 3-4. Bi-shell valve output. (A) Upper bound output at $p = p_{\mathrm{i}}$ and bi-shell valve output at $p = p_{\mathrm{ii}}$. (B) Performance output of bi-shell valve as a function of the normalized thickness t_2 / R of the imperfect shell for given geometry of the spherical cap. (C) Volume change, $\Delta V^* / \Delta V^*_{\mathrm{upper}}$, as a function of the meridional angles defining the upper and lower boundary of imperfection, θ_{U} and θ_{L}. (D) Released energy, $\Delta U^* / \Delta U^*_{\mathrm{upper}}$, as a function of the meridional angles defining the upper and lower boundary of imperfection, θ_{U} and θ_{L}. Normalization factors of the volume change and released energy are the upper bounds $\Delta V^*_{\mathrm{upper}}$ and $\Delta U^*_{\mathrm{upper}}$. The unattainable region in white corresponds to cases where θ_{U} is below or equal to θ_{L}.

3.3.6 Application of the bi-shell valve

We now capitalize on the performance assessment and physical insights gained so far to demonstrate the capacity of our bi-valve to leverage shell snapping interaction for rapid actuation of fluidic soft actuators. As illustrative application, we employ a soft pneumatic striker that we actuate through our bi-shell valve. The goal is to make the striker suddenly move in response to the concerted snapping of the valve shells, deflated merely with slow volume input, propelling a table tennis ball along a guided track.

Figure 3-5A illustrates the schematic of our ‘soft punch’ system. It consists of an airbag that contracts upon deflation and a paper stick that is driven by the airbag to hit and drive the table tennis ball along a slotted rail. Below the airbag, a pivot is fixed to the slotted rail at its midpoint, around which the paper stick can swing freely through the air. The system works as follows. First, the bi-shell valve is deflated to a state near to its pre-snapping state; during this process, the elastic strain energy is stored in the shells interacting through their input chamber. Second, the airbag is connected to the output chamber. Third, further deflation is applied at a low flow rate; this enables the pressure in the input chamber underneath the shells to reach the buckling load of the spherical cap. At this stage, the spherical cap snaps downward and swiftly engages its imperfect counterpart to snap upward. Shell cooperation is now capitalized. The elastic energy and volume change hoarded in the imperfect shell before snapping is now released to propel fast deflation of the spherical cap. Since the output chamber surrounding the spherical cap connects to the airbag, the accrued rapid volume change is dispensed to fast deflate the airbag (Figure 3-5B). Since the tubing connecting the valve and soft actuator is short, the flow resistance or backpressure of the tubing is negligible. As a result, the upper part of the stick retracts and swings backward around the pivot, whereas its lower portion knocks the ball forward, away from its initial position.

Figure 3-5C and D show the physical realization of the schematics shown in Figure 3-5A and Figure 3-5B. In Figure 3-5C, the airbag is connected through a tube to the output chamber of our bi-shell valve (Figure 3-5A), while a syringe inflates the airbag from its natural flat condition to its fully inflated state. Once full inflation is reached, the syringe ceases to provide any increase of air volume. Deflation of the input chamber at the inlet is at a constant flow rate of 3 mL/min. After snapping, the airbag deflates almost instantly until air exhaustion, a condition where the air bag becomes fully rigid. The absence of air in the airbag impedes the spherical cap to reach full eversion, rather only a dimple forms on its top (Figure 3-5D). Despite full eversion is not being attained, the partial snapping enables the striker to hit the table tennis ball up to 3 cm from its initial position (Movie S2, Supporting Information). We emphasize that if the bi-shell valve cannot generate sufficient volume change to meet the requirements of a given soft robotic application, e.g.

when the stiffness of the actuator influences the bi-shell valve output, then the valve design (see Figure 3-21 for design flow chart, Supporting Information) can be readjusted through the metrics introduced in the maps of Figure 3-3 and 3-4. This shows a versatile design for our valve capable of matching the actuator performance, and reaching the target volume change regardless of the actuator performance.

Figure 3-5E shows the displacement and velocity imparted by the striker to the table tennis ball. Before actuation, the ball rests in its initial position with both displacement and velocity equal zero. This reflects the condition of the airbag being not deflated. Upon snapping, the ball quickly accelerates to reach a speed of 58 mm s^{-1} within 0.16 s. After actuation, the ball keeps moving on the rail until the speed gradually declines to zero, due to the combined effects of rail friction, rail unevenness and air drag.

To further prove that the fast movement of the striker is enabled by our bi-shell valve, we perform two additional tests that compare the striker actuation in two scenarios (Figure 3-6): one with the bi-shell valve and the other without the valve. In this set of tests, we focus on the response of the striker only, and hence we remove the table tennis ball and the rail. For the first test (Figure 3-6A to D), we connect the striker to the bi-shell valve and slowly deflate the valve at a constant flow rate of 3 mL/min. The airbag quickly deflates within 0.16 s upon snapping (Movie S3, Supporting Information), a result in agreement with the time required by the table tennis ball to accelerate. For the second test (Figure 3-6E to H), we remove the bi-shell valve and directly deflate the airbag at the identical flow rate (3 mL/min). What we observe here is that the airbag slowly shrinks to the fully deflated state over about 13 s (Movie S4, Supporting Information), i.e. roughly 80 times slower than the first scenario. The comparison of these test results attests that our bi-shell valve is responsible for the fast movement of the striker. In summary, the experiments above demonstrate that our bi-shell valve can achieve fast actuation through a slow volume input. While existing snapping valves [22, 29, 43-45] can provide binary control of a given flow, our concept leverages shell cooperation and snapping interaction to quickly impart a fast volume change that can be used for actuation.

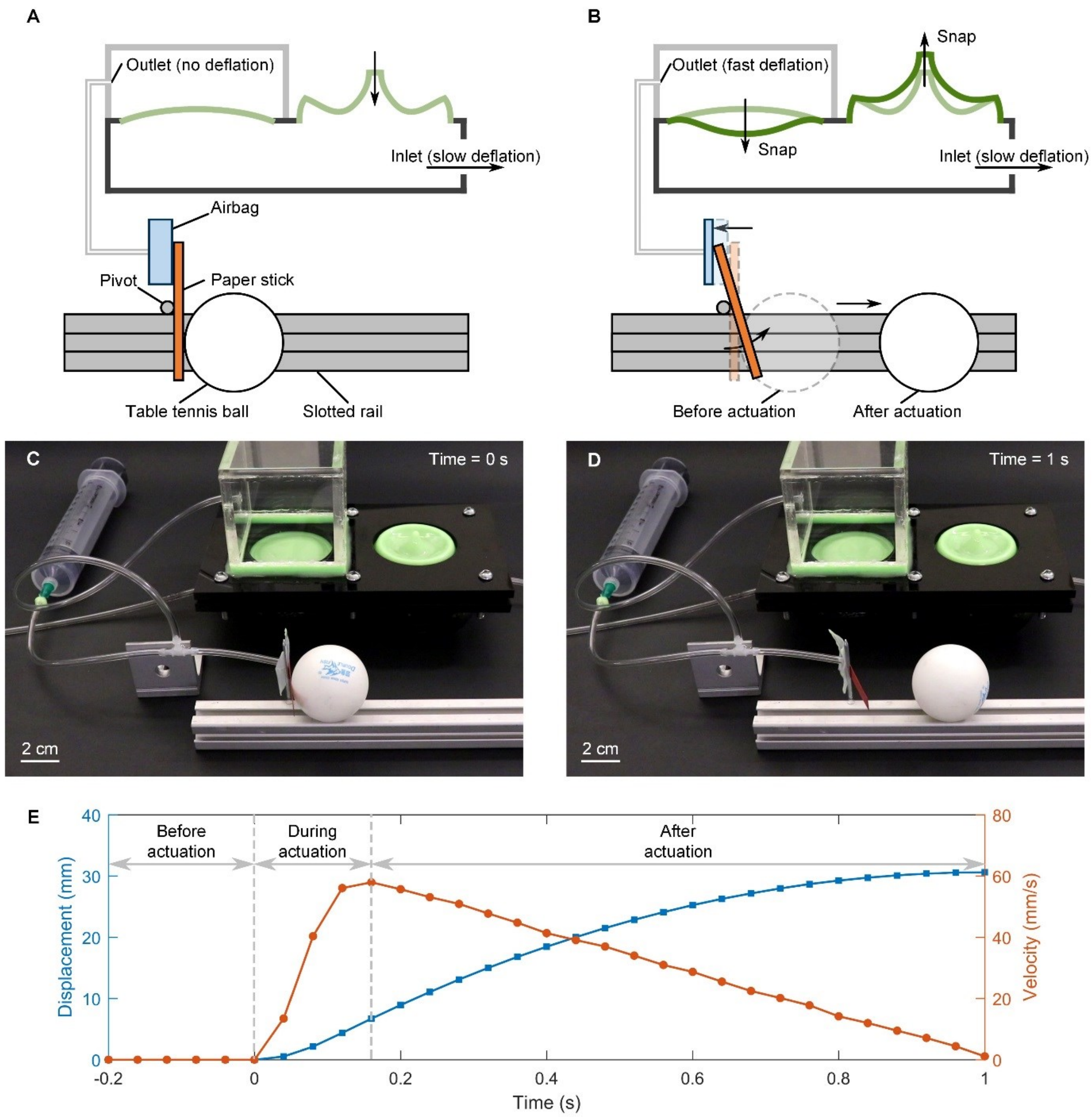

Figure 3-5. A striker rapidly actuated by bi-shell valve to propel motion of table tennis ball. (A) The striker consists of an airbag and a paper stick. The airbag is connected to the bi-shell valve. The paper stick is constrained by a pivot fixed to the slotted rail to enable swinging around its midpoint. A table tennis ball placed on the slotted rail is in contact with the paper stick. (B) Upon snapping of the bi-shell valve, the airbag rapidly deflates to swing the paper stick, which rotates anti-clockwise to hit the ball along the rail. (C) and (D) Photographs prior and post the striker hit (Movie S2, Supporting Information). A syringe is used to inflate the airbag from its natural flat condition to its fully inflated state; it ceases to provide any increase of air volume once full inflation is reached. (E) Displacement and velocity of the table tennis ball as a function of time. Time = 0s is the instant when the striker is actuated by the bi-shell valve.

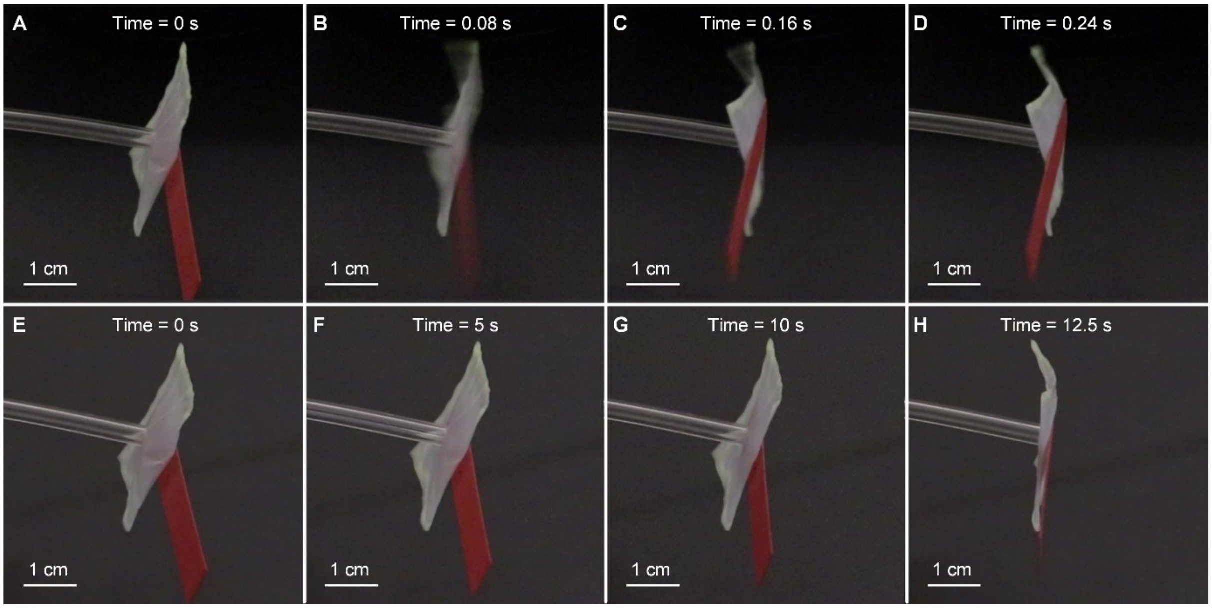

Figure 3-6. (A to D) Fast actuation of the striker enabled by the bi-shell valve. The striker can reach full deflation in 0.16 s and reach a state with no intrinsic vibration at 0.24 s. (E to H) Slow actuation of the striker due to the absence of the bi-shell valve. More than 10 s are required for actuation. For both tests, the actuation time is counted from the 0 s instant.

3.3.7 Discussion

Widely used methods currently available for rapid actuation mainly resort to pressure-controlled strategies that require a bulky system of pressure supply, sensors, hard valves, and control algorithms [4, 15]. Other methods to achieve rapid actuation either employ explosive chemical reaction [39-42] or exploit a structural instability embedded within the actuator, which would require the integration of snapping spherical caps [31] or balloons [32, 36, 37] into the architecture of the actuator. In contrast, our bi-shell valve does not rely on the fast volume input from pressure control or any modifications to the actuator design. It can be easily implemented with a simple volume input dispensed through a syringe and connected to an existing actuator. We note that the pressure output is governed by the constituent shells. In this work, the snapping pressure of the bi-shell valve is in the range 405-549 Pa (Figure 3-12, Supporting Information). Yet, the snapping pressure can be increased by stiffening the shells. On this front, two strategies can be followed. One is to thicken the shell and scale up the snapping pressure to a value as large as 10 kPa, as demonstrated in the literature [29]. Another way is to choose a material with Young's modulus higher than that of our prototype valve (see Supporting Information for details). Both methods can be used either individually or in combination to further amplify the pressure output and meet the design requirements imposed by the application.

In addition, our valve performance could not be achieved by employing one single shell, as in existing valve designs delivering mainly fluid control function [22, 29, 43-45]. The reason is that the flow rate difference between the valve input and the valve output is enabled by the volume rapidly transferred between the constituent shells during snapping. This allows to convert the low flow rate at the inlet to a fast flow rate at the outlet. If only one shell were used, either the spherical cap or the imperfect shell, no fast actuation would be attainable because there would be no means in place for flow-rate conversion, i.e. no fast transfer of air volume can be accomplished. Another advantage is the self-adaptivity of its volume output to that of the actuator. Our experiments have shown that the valve can be autonomously adjusted to yield a volume output that is compatible with the volume of the actuator at the outlet, hence preventing the actuator from any possible damage caused by excessive deflation. Furthermore, the hyperelastic constitutive law of the shell base-material guarantees reversible and repetitive snapping imposed by a cyclic loop of deflation and inflation (Movie S5, Supporting Information), which is common for soft robots and actuators [29, 31]. In our demonstration, the choice to show the bi-shell valve on a system containing rigid components is only for the convenience to observe the snapping event and the interaction of the constituent shells. Our bi-shell valve can be made fully soft by replacing the rigid components with their soft counterparts, and thus it can be embedded into soft robots in a straightforward manner. To integrate our valve within a soft robot, the output chamber can be merged with the interior of the soft actuator, while the whole system of the bi-shell valve and the soft actuator can be controlled from the input chamber. A possible layout of the valve-actuator integration is given in Figure 3-25 (Supporting information). Both the rigid input and output chambers can be replaced with thick soft walls by molding [29]. The integration would only require the merging of both molds, that of the bi-shell valve and that of the soft actuator.

While our current concept is devised mainly to attain rapid deflation, the potential to embed more functions is at hand. For example, the bi-shell valve can be designed as a fuse of volume change by placing the output chamber above the imperfect shell, rather than on the spherical cap (Figure 3-22, Supporting Information). In this case, the volume output will initially increase with the volume input until a threshold is reached; at this stage the imperfect shell inflates with the snapping of the valve. Another example is the potential to swap deflation (negative pressure) with inflation (positive pressure). Several pneumatic robots are actuated by inflation rather than deflation. By flipping the imperfect shell and the spherical cap upside down (Figure 3-22, Supporting Information), our bi-shell valve can be reset to operate under inflation. Compared to existing valves [43, 45, 53] that are capable of continuous operation, the bi-shell valve and the variational designs for inflation here presented can provide an impulse output with finite volume (Figure 4C). At the design stage, it is necessary to ensure that such an impulse can provide the volume change that is sufficient to fast actuate the soft actuator. Moreover, while the bi-shell valve presented here provides a simple task for fast actuation, more complex logic functions could be achieved by integrating the valve into the fluidic system of circuits of a soft robot [22, 23, 29, 44].

3.4 Conclusion

To achieve rapid actuation of soft pneumatic actuators, we have introduced a soft bi-shell valve that can convert a slow volume input into a fast output. The underpinning principle is the interaction during snap-through of its elastic soft constituents: an imperfect shell and a spherical cap. Upon deflation, the former first stores sizeable values of volume change and elastic energy, which are then suddenly released upon snapping of the latter. Its rapid volume output can be used to deliver fast actuation. Upper bounds and performance metrics have been presented to design the bi-shell valve for target requirements of soft robotic applications. The spherical cap determines the snapping pressure and the upper bounds of volume change and released energy, while the imperfect shell interacts with the cap to yield an attainable valve output. Tuning defect geometry and shell shape enables to passively code the snapping event, calibrate volume and energy output and maximize the valve performance. Through the demonstration of the striker, we have shown that the bi-shell valve can accelerate the motion of soft actuators under volume control, thus avoiding the need for fast volume input provided by pressure control nor additional modifications to the body of the actuator that use chemical explosion or elastic instability. In conclusion, the bi-shell valve concept introduced in this work along with its variational designs are poised to offer new routes to provide actuation of soft pneumatic actuators.

3.5 Methods

Methods: Supporting Information 3.6.1 details the fabrication methods, while the experimental characterization of the bi-shell valve and the elastic shells are described in Supporting Information 3.6.2. The effect of air compressibility is discussed in Supporting Information 3.6.3. Supporting Information 3.6.4 reports the numeric analysis. Supporting Information 3.6.5 to 3.6.7 discuss the buckling modes of the imperfect shell, the interaction between the spherical cap and the imperfect shell, and the upper bounds of valve output. The flowchart detailing the valve design as well as design variations of the bi-shell concept are presented in Supporting Information 3.6.8 and 3.6.9. The effects of material property are studied in Supporting Information 3.6.10. Supporting Information 3.6.11 presents a possible layout for the integration of the bi-shell valve into a soft robot or actuators, and 3.6.12 discusses the scenario of a similar valve with only one shell.

3.6 Supporting Information

3.6.1 Fabrication

Fabrication of the input chamber

Figure 3-7 illustrates the manufacturing process for the input chamber encompassing six layers laser cut (CM1290 laser cutter, SignCut Inc., Canada) from a 6-mm-thick acrylic plate (McMaster-Carr, USA). The first layer at the bottom is fully solid with geometry parallel to the external profile of the two shells. From the second to the fifth layer the acrylic plates consist of a 15.5-mm-wide ring with an external profile identical to the first layer, forming the wall of the input chamber. Moreover, the third and fourth layers have an opening at both ends along their long axis, a feature that allows connection to the PVC plastic tubing for volume input and pressure sensor. The sixth layer at the top covers the input chamber enclosed by the first five layers, with two large circular holes that connect the imperfect shell and the spherical cap. In addition, six smaller holes on the top layer are used to fasten the input chamber with other parts of the bi-shell valve. Adhaero SuperGlue (Dollarama, Canada) is used to join all pieces of the input chamber assembly, and silicone rubber Elite double 32 (Zhermack, Italy) is applied to seal off its internal walls.

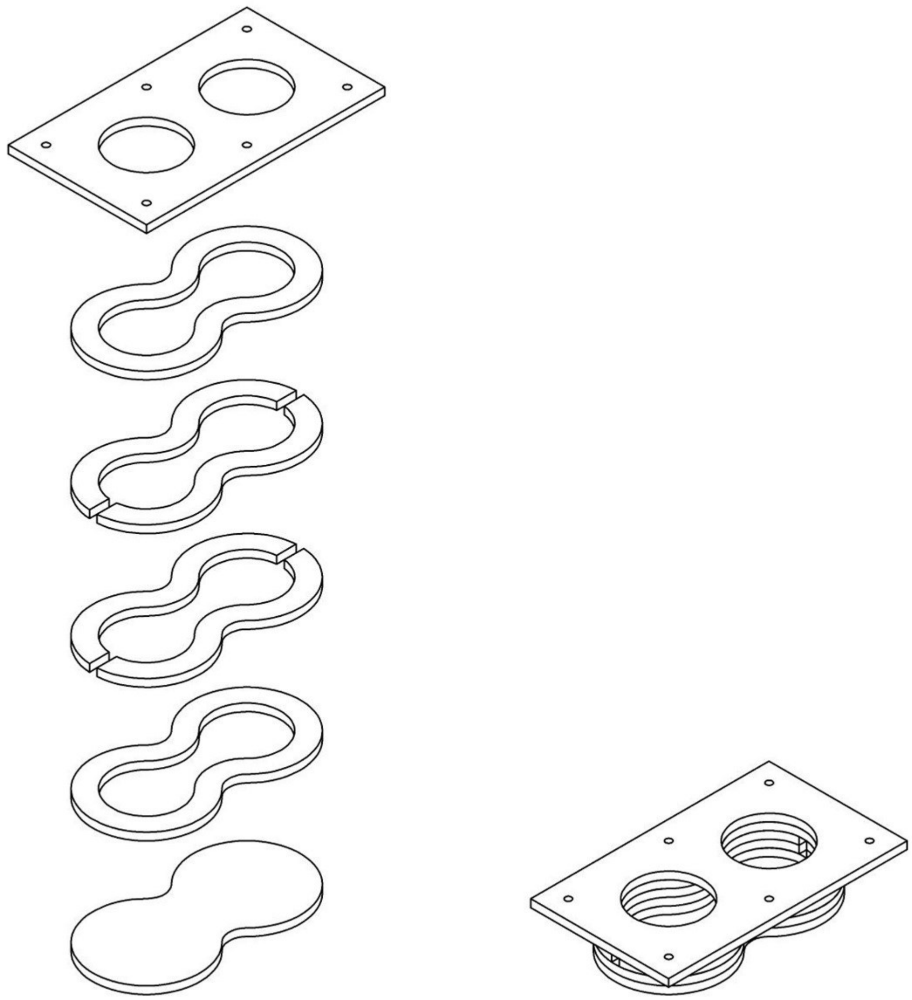

Figure 3-7 Assembly of the input chamber

Fabrication of the output chamber

Figure 3-8 shows the output chamber consisting of five laser cut acrylic plates, which forms an open cubic cell that can capture the rapid volume change of the spherical cap. Again Adhaero SuperGlue (Dollarama, Canada) is applied to join the fives plates and Adhaero epoxy (Dollarama, Canada) is used to seal them. The small hole on the left-hand side of the cell provides the outlet of the output chamber, which in turn is connected through tubing to the soft actuator.

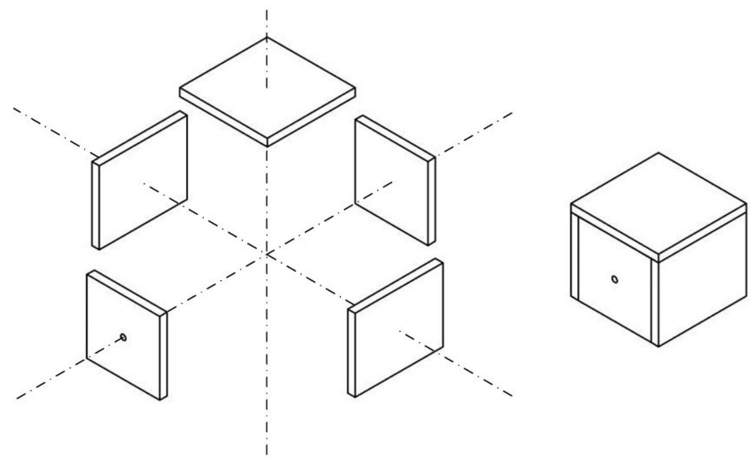

Figure 3-8 Assembly of the output chamber

Fabrication of the elastic shells

Shell fabrication for both the imperfect shell and the spherical cap follows a procedure previously used [47, 54]. Elite Double 32 (Zhermack, Italy) is casted on the surface of 3D-printed molds (Figure 3-9). For each shell, we fabricated a 1 mm-thick mold with Onyx filament using fused deposition modeling (FDM). The surface of the molds has geometry identical to that of the as-designed elastic shells ($R = 25$ mm , $h/R = 0.2$, $\theta_L = 20°$, and $\theta_U = 85.9°$), with a groove at the bottom to collect excessive deposition of liquid and form a thick band that provide a clamping action. To locally reduce excessive accumulation of Elite Double 32 liquid on the curved surface of the mold, we used a homemade spin coating unit to spin the mold at a speed of ~240 rpm. More specifically, the shells were fabricated at room temperature by following these steps:

a) Prepare the catalyst and base of Elite Double 32 with 1:1 volume fraction.
b) Mix and manually stir the prepared catalyst and base for ~1 min.
c) Turn on the power of the spin coating unit.
d) Slowly pour the mixed Elite Double 32 solution onto the mold.
e) Spin ~10 min to remove excessive liquid on the mold.
f) Turn off the power of the spin coating unit.
g) Wait about 15 min to fully cure the Elite Double 32 solution.

h) Systematically increase shell thickness by repeating the above steps a) to g) until the designed thickness is attained.

i) Repeat steps a) and b) and fill the groove at the bottom of the mold with mixed Elite Double 32 solution.

j) Wait ~25 min until the Elite Double 32 solution is fully stabilized.

k) Peel off the elastic shell from the mold.

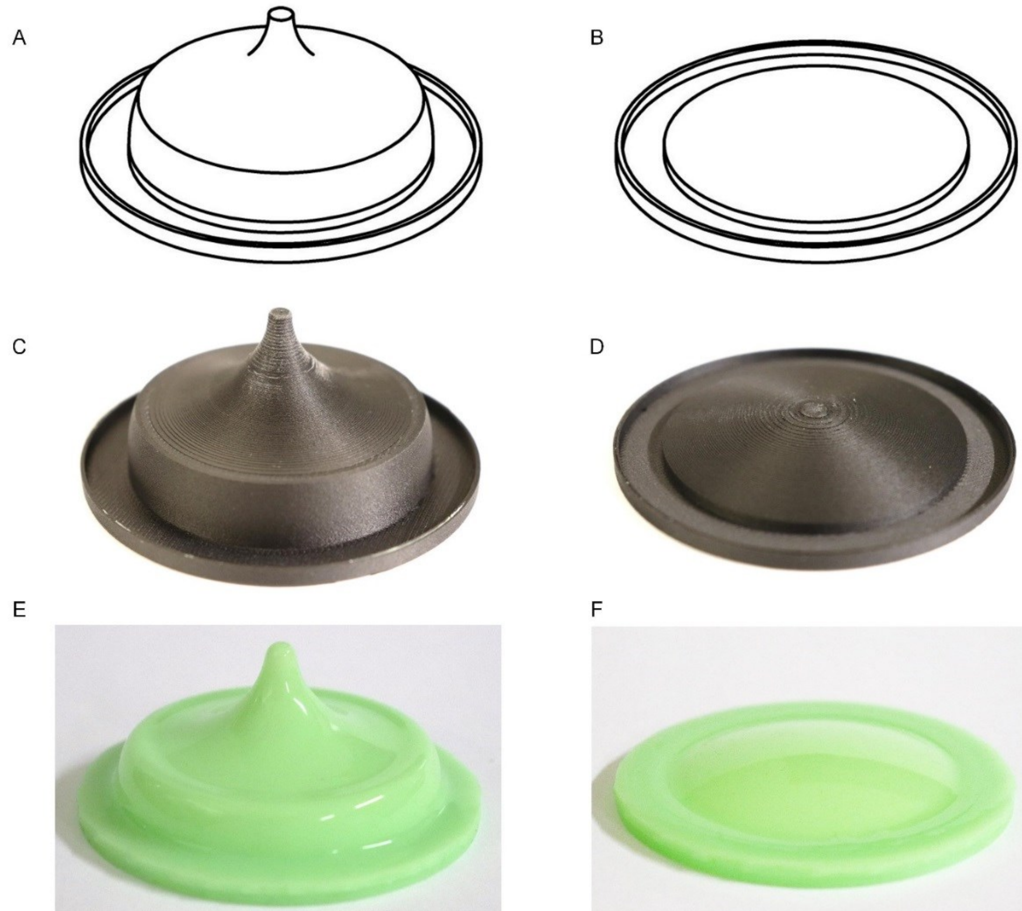

Figure 3-9 Mold for the imperfect shell and the spherical cap. (A) and (B): schematic of each respective mold. (C) and (D): 3D printed mold. (E) and (F): Fabricated shells.

Assembly of the bi-shell valve

Figure 3-10 shows the components and assembly of our bi-shell valve system. The imperfect shell and the spherical cap are mounted on the input chamber, with their inner volume connected through the two large holes on the top surface of the input chamber. Any leakage that may exist between the elastic shells and the input chamber are sealed with Elite Double 32. Above the elastic shells is a fixture plate, which can be fastened to the input chamber with screws through six small holes along its edges. This fixture plate has two large circular holes that allow the elastic shells to freely deform without entering in contact with the fixture plate. Since the base of the spherical cap is thicker than that of the imperfect shell, the fixture plate can tightly clamp the base of the spherical cap on the input chamber to ensure airtight connection to the output chamber. The output chamber is mounted on the fixture plate with a square gasket made of Elite Double 32 that can tolerate the deformation of the fixture plate due to clamping. The leaks that may occur between the fixture plate and the output chamber are sealed with Elite Double 32 and Adhaero 5 minute epoxy (Dollarama, Canada).

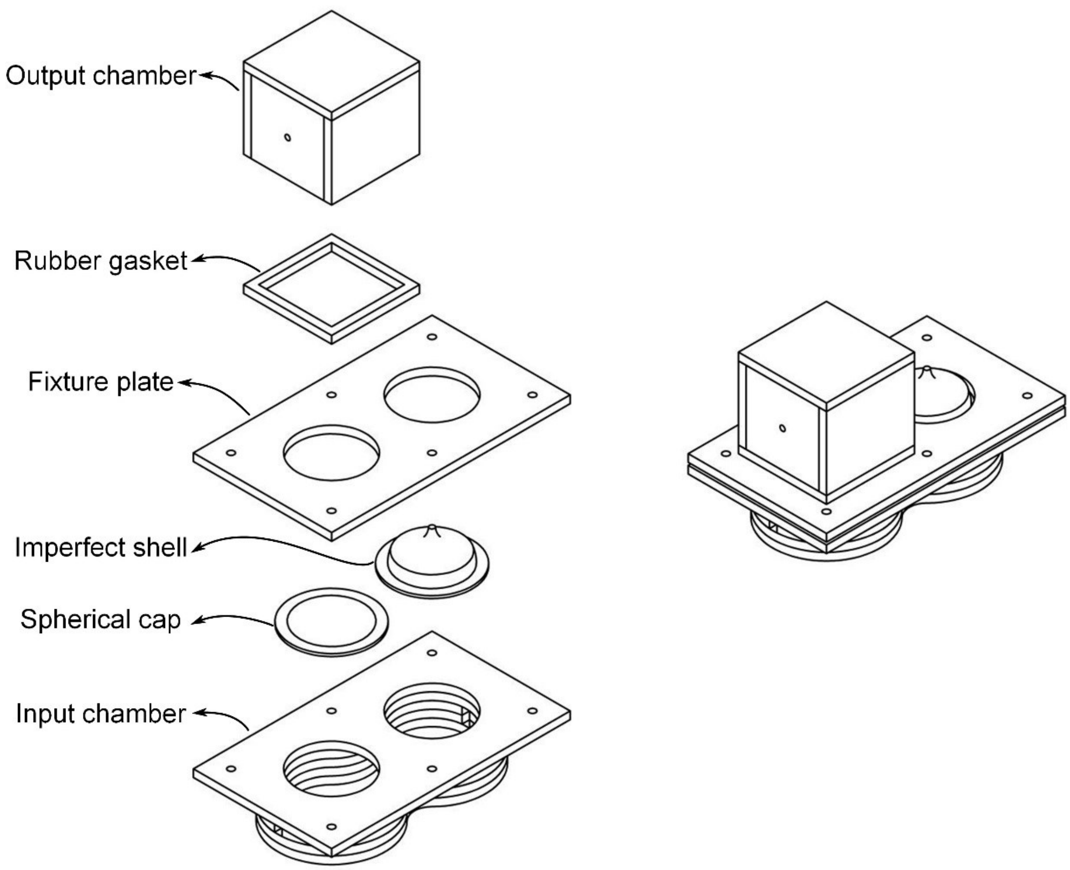

Figure 3-10 Components and assembly of the bi-shell valve system.

Fabrication of the pneumatic striker

Our pneumatic striker consists of two main components: a miniature airbag to convert volume input into motion, and a paper stick to hit the table tennis ball. The airbag is cut from a 0.02-mm-thick compostable kitchen bag (no name, Loblaws Inc, Canada) as a folded bi-layer film with an area of 28x28 mm. A segment of tubing is glued on the bottom surface of the cut film with Adhaero SuperGlue. A hole is then cut through the film to enable airflow between the airbag and the tubing. Finally, the airbag is sealed with Elite Double 32. The paper stick is cut from a 0.29-mm-thick paper and then glued on the top surface of the airbag with Elite Double 32. The length of the stick is 56 mm, and the width is 7 mm.

3.6.2 Experimental characterization

Characterization of a single shell

To characterize the pressure-volume response of a single shell, we assemble the experiment apparatus shown in Figure 3-11, which includes an acrylic fixture to hold the sample, a polypropylene syringe of 60 mL capacity to extract air from the sample, a Bose ElectroForce 3510 tester (Bose Corporation, Framingham, Massachusetts) to control the syringe, a pressure sensor (HSCDRRN002NDAA5, Honeywell, USA) that has a measurement range of ±498 Pa and an accuracy of ±2.5 Pa, and a microcontroller (Arduino UNO, Arduino, Italy).

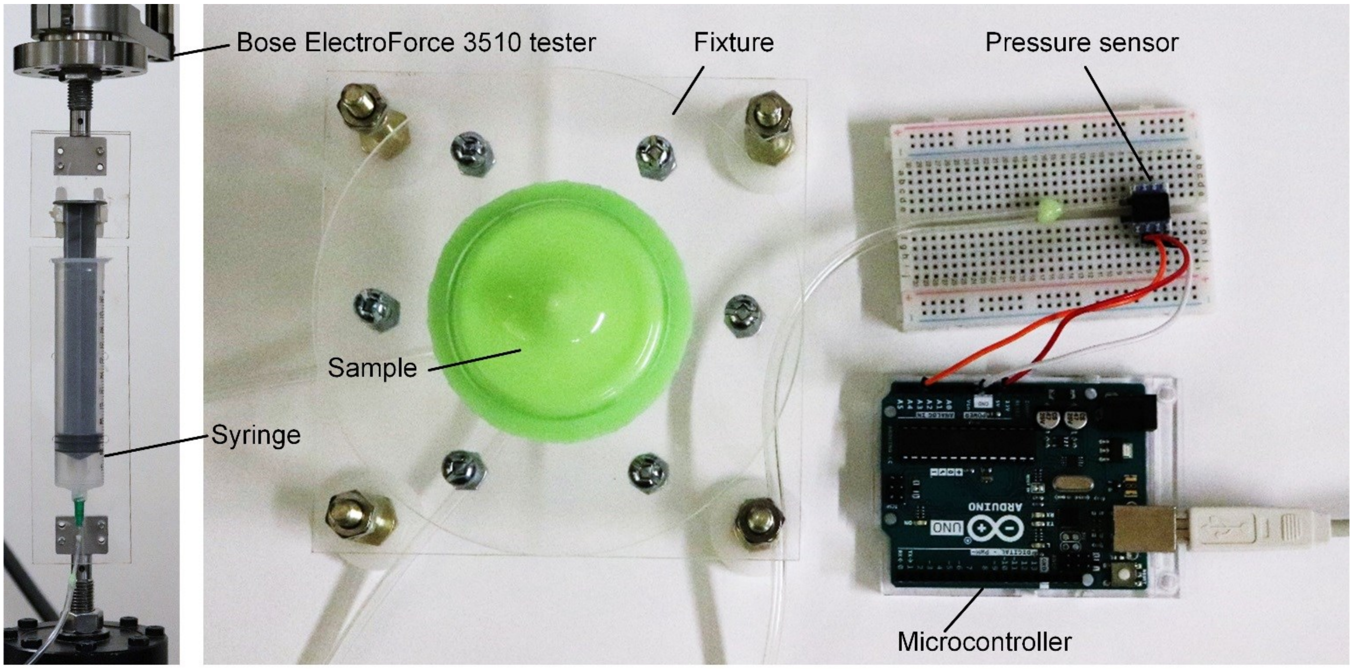

Figure 3-11 Experimental set-up for the characterization of a single shell.

The fixture consists of a top plate and a bottom plate. The top plate has a round geometry and is placed above the shell. There is a circular hole at the center, which not only allows the body of the shell to freely deform without entering in contact with the plate, but also clamps the base of the shell on the bottom plate. The bottom plate features a square geometry, and is connected to the syringe and the pressure sensor with a PVC plastic tubing. A 6-mm-thick ring gasket made of acrylic is glued at the center of the bottom plate, providing room for the spherical cap to fully deflate without getting into contact with the bottom plate. The top and bottom plates can be tightly fastened with six equally spaced screws to prevent any air leakage.

In our test, the syringe is pulled by the Bose tester at a speed of 0.1 mm/s to generate a constant flow rate of 3 mL/min. The microcontroller is programmed to read the pressure measurement at a frequency of 20 Hz, which is then recorded as a function of time with a data acquisition software (PLX-DAQ, Parallax, USA). For both the spherical shell and the imperfect shell, three samples have been tested under identical conditions. The resulting curves (pressure-volume) along with the representative envelope of the experimental response of all tested samples are plotted in Figs. 2E and 2F.

Characterization of the bi-shell valve

Our experiment with the bi-shell valve is performed with the set-up described above for deflation and pressure measurement. The syringe and the pressure sensor are connected to the input chamber with the tubing at the bottom the valve. The flow rate of deflation is 3 mL/min, while the frequency of pressure measurement is 20 Hz. To assemble the bi-shell valve, we select one pair of spherical cap and imperfect shell from the pool of the single shell samples tested individually in the analyses of the previous sections. The result from the tests are shown in Figure 3-12. The results show that the snapping pressure of the valve can be programmed by the clamping condition of the spherical cap from 405 Pa when the spherical cap is not clamped (test 1), to 591 Pa when the spherical cap is tightly clamped (test 4). The increase in snapping pressure is caused by the initial deformation of the spherical cap due to clamping, a behaviour studied numerically in Supporting Information 3.6.4.1. The curve of test 2 corresponds to the results illustrated in Figure 3-2D with a snapping pressure identical to the test result of the individual spherical cap shown in Figure 3-2E. We assume that the initial deformation of the spherical cap in test 2 is identical to the initial deformation of the cap when tested alone. The curve of test 3 corresponds to the bi-shell valve used in our demonstrative experiment, where the spherical cap buckles at 549 Pa. The higher snapping pressure of 591 Pa attained in test 4 is only used to show the role of a given clamping condition.

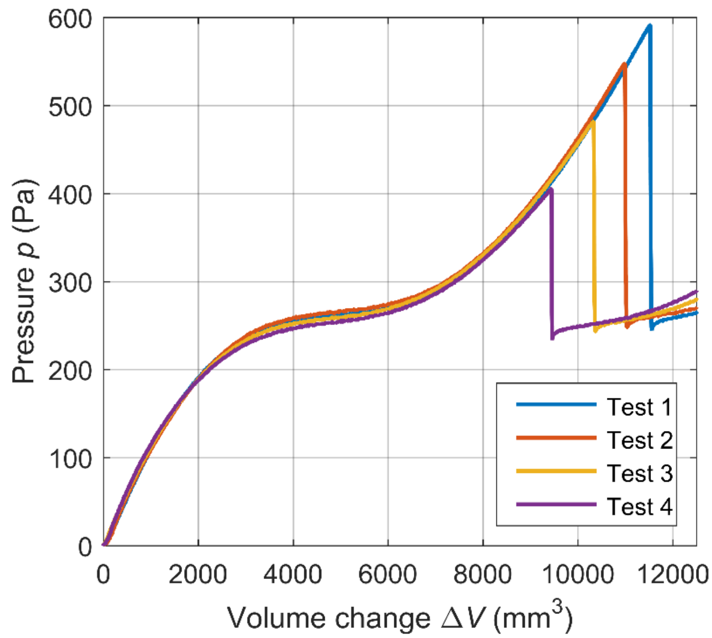

Figure 3-12 Pressure-volume response of the bi-shell valve. Pressure-volume response of the bi-shell valve. The spherical cap is not clamped in test 1 and tightly clamped in test 4, while tests 2 and 3 correspond to intermediate clamping conditions.

3.6.3 Effect of air compressibility

Since air is a compressible fluid, here we study the influence of air compressibility. We assume that the air in the bi-shell-valve, the tubing, and the syringe follows the ideal gas law:

$$pV = nR_gT \tag{3-1}$$

where p is the pressure of the gas, V is the volume of the gas, n is the amount of substance of gas, R_g is the ideal gas constant, and T is the absolute temperature of the gas. In both the initial state and loaded states. the gas in the pneumatic system (the bi-shell valve, syringe and connecting tubing) must satisfy

$$p_{sys0}V_{sys0} = nR_gT_{sys0} \tag{3-2}$$

and

$$p_{sys1}V_{sys1} = nR_gT_{sys1} \tag{3-3}$$

where the subscript stands for initial (0) and loaded states (1).

We assume the gas undergoes an isothermal process ($T_{sys0} = T_{sys1}$), which yields

$$p_{sys0}V_{sys0} = p_{sys1}V_{sys1} \tag{3-4}$$

The volume change due to air compressibility can be expressed as

$$\left|V_{sys1} - V_{sys0}\right| = \left|\frac{p_{sys0}}{p_{sys1}} - 1\right|V_{sys0} \tag{3-5}$$

This value is proportional to the initial volume of the system V_{sys0}, and increases with the pressure change from the initial state. In our bi-shell valve, the maximum change in pressure from the initial state (atmosphere pressure $p_{sys0} = p_{\text{atm}} = 1.01\times10^5\ \text{Pa}$) is below 550 Pa, which yields

$$\left|\frac{p_{sys0}}{p_{sys1}} - 1\right| < 0.54\% \tag{3-6}$$

We can thus rewrite the volume change due to air compressibility as

$$\frac{\left|V_{sys1} - V_{sys0}\right|}{V_{sys0}} < 0.54\% \tag{3-7}$$

For our tests on the bi-shell valve, the total volume is about $V_{sys0} = 1.8\times10^5\ \text{mm}^3$, leading to a volume change of $\left|V_{sys1} - V_{sys0}\right| < 9.9\times10^2\ \text{mm}^3$. For the characterization of a separate shell, the total volume of the system is about $V_{sys0} = 5\times10^4\ \text{mm}^3$, leading to a volume change of $\left|V_{sys1} - V_{sys0}\right| < 2.7\times10^2\ \text{mm}^3$. These values are tiny in comparison with the volume change of the shells ($\sim 1.3\times10^4$ mm^3 for the bi-shell valve and $\sim 7.5\times10^3$ mm^3 for a single shell), and corroborate the assumption made in this work that air compressibility can be neglected. Hence, the volume change of the syringe can be assumed as the volume change of the bi-shell valve and the separate shells.

3.6.4 Finite element analysis

To further investigate the mechanical performance of the bi-shell valve, we conduct a set of finite element method (FEM) simulations with the commercial software package ABAQUS/STANDARD. The shell material is modelled as an incompressible neo-Hookean solid. The Young's modulus and Poisson's ratio (1.23 MPa and 0.5) are determined by fitting the simulation results with the experimental data within a range previously used in the literature [54, 55]. This leads to the adoption of the following coefficients for our neo-Hookean model: $\mathrm{C10} = 0.205$ MPa and $\mathrm{D1} = 0$ MPa^{-1}. We employ the modified Riks method to simultaneously solve for pressure and shell deformation. Since in our experiments we observe that both the imperfect shell and the spherical cap exhibit only an axisymmetric mode of deformation, we build our numerical model with axisymmetric elements (the two-node linear shell element SAX1 or the four-node bilinear quadrilateral element CAX4RH) to avoid the expensive computational cost of three-dimensional simulations. Although in some cases the imperfect shell may exhibit non-axisymmetric deformations, our previous study shows that an axisymmetric analysis can still be sufficient to retain a high level of accuracy [47]. We impose a fixed boundary condition at the bottom of the shells and a uniform pressure at their surfaces. The volume change ΔV is calculated with the pressure p and the total external work done by the pressure U_p, which is given by

$$\Delta V = \int \frac{1}{p} \mathrm{d}U_p. \tag{3-8}$$

As described below, our computational analysis for each separate shell as well as for the bi-shell valve is conducted into two steps. First, we consider an as-designed (ideal) model that is free from any manufacturing imperfections and does not account for any initial deformation caused by the clamping of the bottom ring. In this scenario, we systematically explore the geometric space of the bi-shell valve to unveil its sensitivity to a varying shell geometry. Second, to validate our numerical model with experimental results, we develop a set of realistic models, one for the spherical cap and the other for the imperfect shell. These models enable to capture the effect of the initial deformation due to clamping in spherical cap, and to incorporate as-manufactured imperfections, in particular thickness variations, in fabricated imperfect shells.

3.6.4.1 Modelling of the spherical cap

As-designed model. The as-designed spherical cap is modelled with axisymmetric line element SAX1. The geometry of the spherical cap is $t_1/R = 0.05$, $h/R = 0.2$, and $R = 25$ mm. A mesh convergence study shows that 51 elements are sufficient to model the spherical cap (Figure 3-13A). In this work, around 51 elements are used for the spherical cap. To systematically study the response of the spherical cap with varying geometry, we explore the geometry space defined by the normalized thickness t_1/R ranging from 0.01 to 0.1 and the normalized height h/R spanning from 0.1 to 0.5; the radius at the base is fixed as $R = 25$ mm.

Realistic model. To capture cross-section variation in a representative sample of the spherical cap, we use a digital camera EOS 800D (Canon, Japan). Our observations show that the spherical cap has a uniform thickness profile (Figure 3-14A), hence our analysis of the spherical cap studies only the role of the initial deformation due to clamping.

In Figure 3-15A, the spherical cap is modelled with CAX4RH elements, whereas the acrylic plate that clamps the base of the cap is modelled with rigid body line elements RAX1. For the spherical cap, our mesh convergence study shows that four elements through the thickness are sufficient (Figure 3-13B). Hence, we employ here at least four elements through the thickness.

The interaction between the cap and the plate is set as "hard" contact with a friction coefficient of 0.5. To investigate the effects of the initial deformation due to clamping, we first apply a downward displacement on the plate, and then apply a pressure on the shell to deflate the shell. The displacement is systematically varied from 0 (no clamping) to 0.3 mm (tight clamping). In Figure 3-15B, when the cap is clamped through the plate for 0.3 mm, an upward displacement occurs at the top of the cap. In Figure 3-16A, we find that the buckling pressure increases monotonically with the displacement of the clamping plate over a wide range of values from 403 Pa (no clamping) to 587 Pa (0.3 mm of clamping). From this set of results for the spherical cap, we decide to include the initial deformation due to clamping in our realistic numerical model. To minimize the difference of results between experiments and simulations, the displacement due to clamping is set as 0.1026 mm. This enables to yield a buckling pressure close to that of the representative sample of the spherical cap (Figure 3-2E), and to bring below 0.6% the relative error in the buckling pressure between simulation and experiment. In addition, we find that the buckling pressure of the unclamped case (Figure 3-16A) is slightly lower than the results in Figure 3-13. The reason for this is that in the simulations that study the effect of clamping, the thick band at the base of the shell is included; this provides an elastic support to the shell which is dissimilar to the fixed boundary condition employed in other simulations.

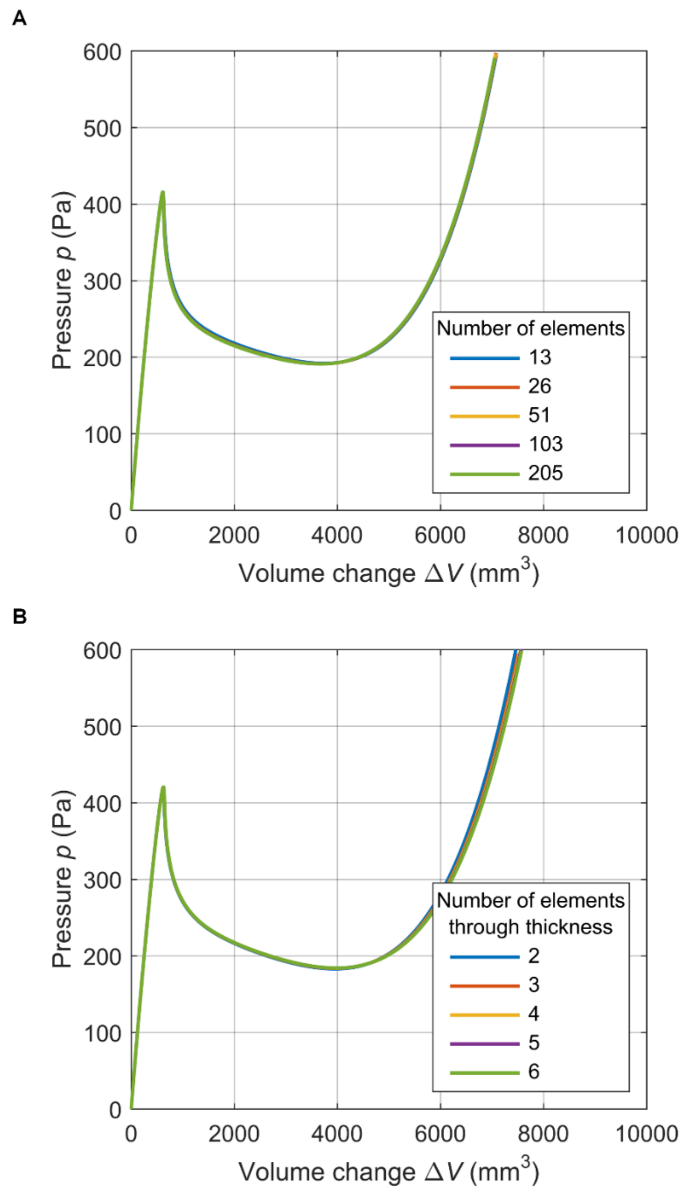

Figure 3-13 Mesh convergence study of the spherical cap. (A) SAX1 element. (B) CAX4RH element. Curves of different colors overlay, thereby showing that the simulation results for meshes with given number of elements have converged.

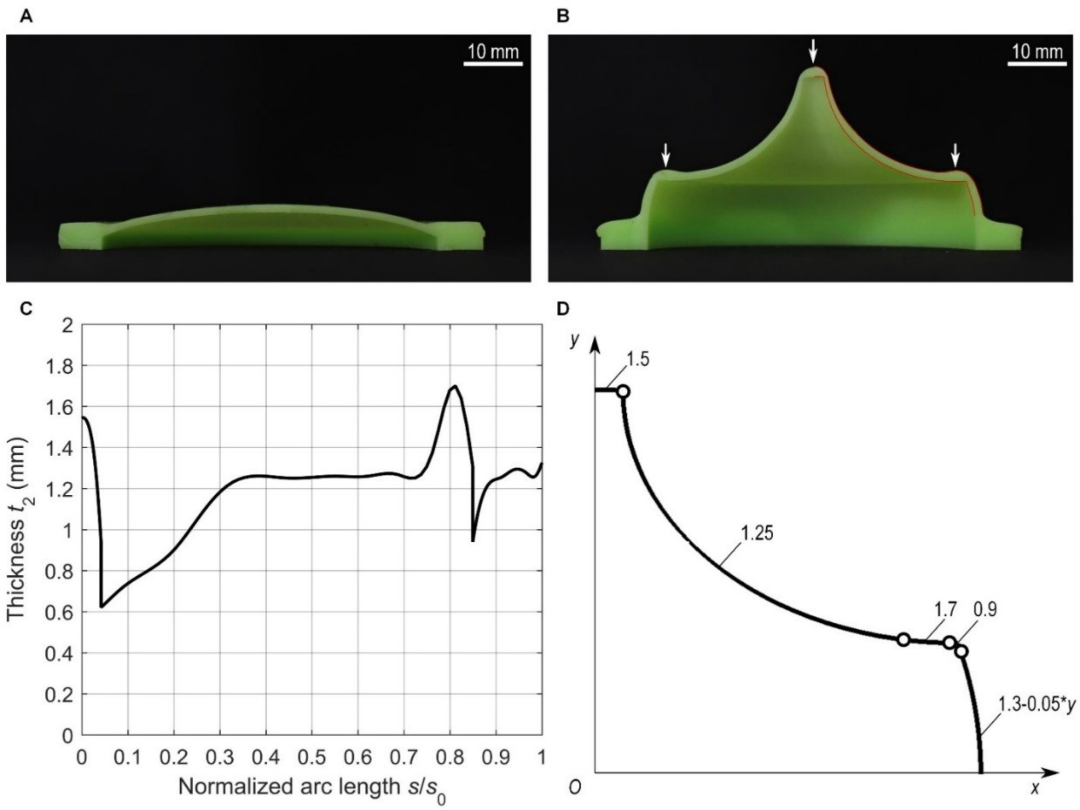

Figure 3-14 Cross-section of representative as-manufactured shell. (A) The spherical cap has a uniform thickness profile. (B) For the imperfect shell, on the other hand, the thickness profile is not uniform due to manufacturing. The red curves mark the upper and lower surfaces of half shell. The arrows marks the spots at the top of the shell and at the bottom of the imperfection with increased thickness. (C) Thickness t_2 of the imperfect shell measured as a function of the normalized arc length s/s_0 from the top ($s/s_0=0$) to the base ($s/s_0=1$). s and s_0 are the arc length and the total arc length. (D) Thickness profile of the imperfect shell used to generate the realistic computational model. The white dots partition the shell into five sections; to each of them the shell thickness is assigned separately to approximate the thickness distribution in (C). y is the distance from the base plane and the unit of the thickness is millimeter.

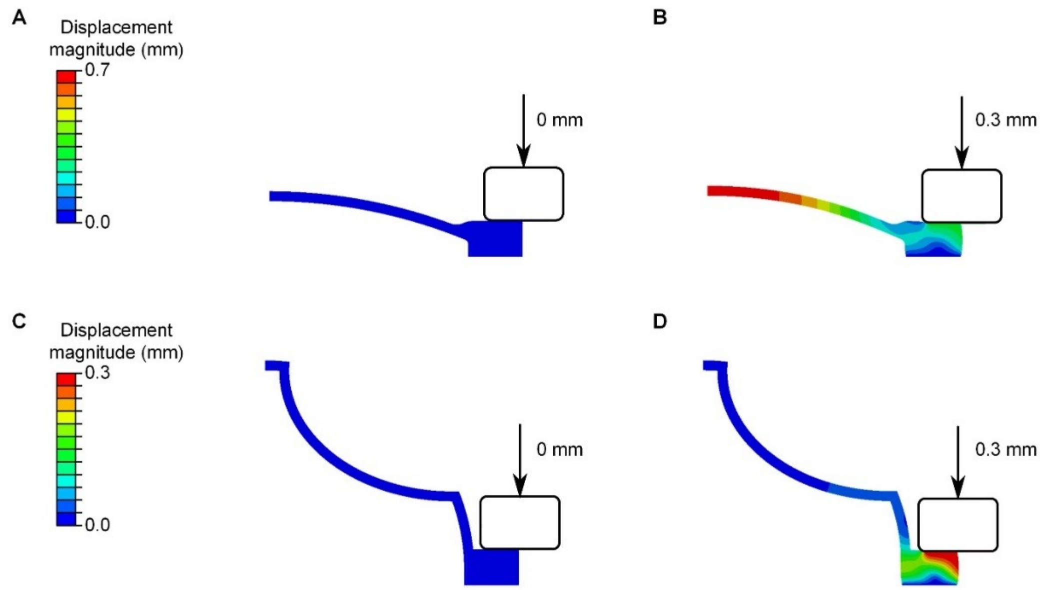

Figure 3-15 Deformation of the shells due to clamping. (A) Initial and (B) clamped configuration of the spherical cap. (C) Initial and (D) clamped configuration of the imperfect shell.

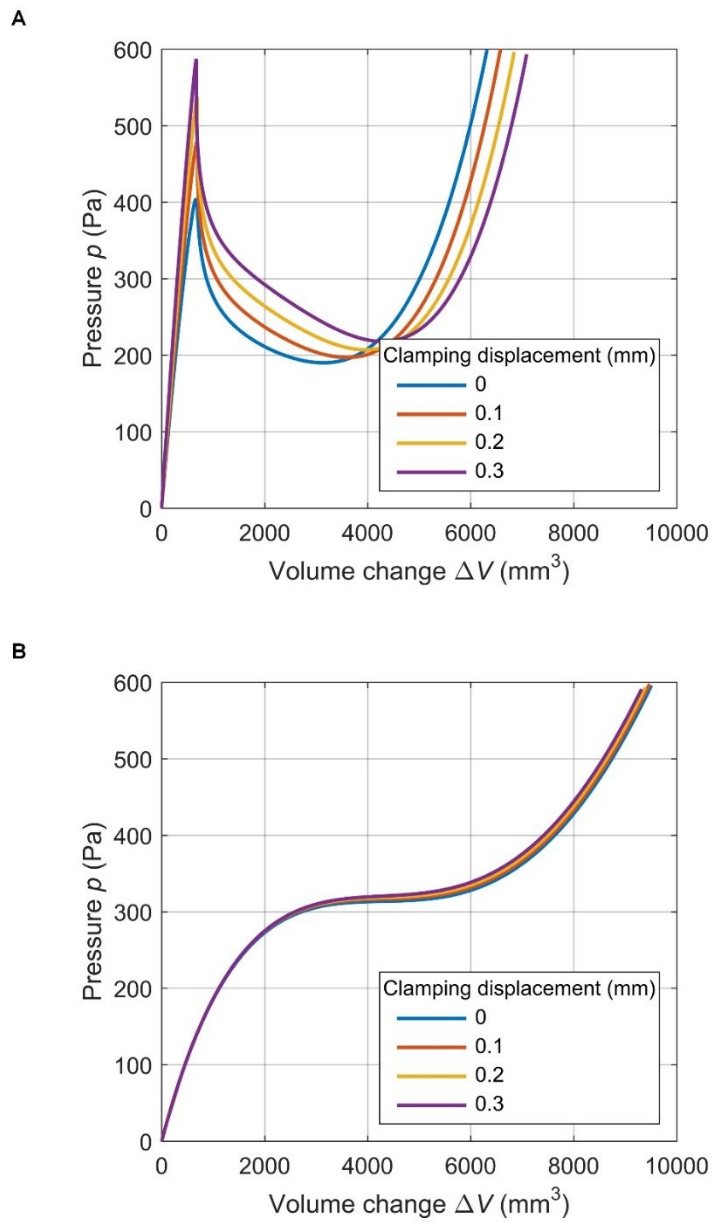

Figure 3-16 Pressure-volume responses of clamped shells. (A) spherical cap, and (B) imperfect shell.

3.6.4.2 Modelling of the imperfect shell

As-designed model

We model the as-designed imperfect shell using the axisymmetric shell element SAX1. The geometry of the imperfect shell is defined by the following parameters: $t_2/R = 0.05$, $\theta_{\mathrm{L}} = 20°$, $\theta_{\mathrm{U}} = 85.9°$, and $R = 25\ \mathrm{mm}$. A wide design space is explored to investigate the buckling sensitivity to the as-designed defect in the form of an ellipse, with respect to the normalized thickness ($0.02 \le t_2/R \le 0.1$) and meridional angle at the upper and lower boundary of the defect ($20° \le \theta_{\mathrm{L}} \le \theta_{\mathrm{U}} \le 85°$). A mesh convergence study shows that 81 SAX1 elements are sufficient to model the imperfect shell (Figure 3-17A). In this work, an average of 81 elements are used for the imperfect shell.

Realistic model

As described above, our fabrication process, in particular the mould we used to produce our samples, had the following outcome on the shell geometries. The thickness profile of the spherical cap is uniform since the mould has no change in curvature, as opposed to that of the imperfect shell, which has variations due to abrupt changes in the curvature of the mould. To develop a realistic model of the imperfect shell with response that parallels that of the as-manufactured geometry, we investigate separately the role of non-uniform thickness as well as that of the initial deformation due to clamping, as described below.

Non-uniform thickness profile. Figure 3-14B shows that the as-manufactured shell features a thickness build up at locations above and below the elliptical arc; it is at those points that sudden changes of curvature appear in the mould. To obtain precise measurement of the thickness profile of the imperfect shell, we determine the distance between the inner and outer surfaces of the shell first from digital images (e.g. Figure 3-14B), and then by rectifying the data with measurements taken through a digital caliper (Figure 3-14C). This set of results is used to generate a numerical model that captures thickness variations along the shell profile; in particular the thickness profile of the shell is partitioned into five sections (Figure 3-14D), and to each of these portions the pertinent thickness is assigned. The SAX1 element is used to generate the model.

Initial deformation due to clamping. Here we solely study the role of the initial deformation due to clamping on an imperfect shell with uniform thickness. Figure 3-15C shows an imperfect shell clamped to the fixture plate. The plate is modelled as a rigid body with the axisymmetric rigid two-node line element RAX1. Since the clamped base of the imperfect shell is too thick to be considered as a shell, we use the axisymmetric quadrilateral element CAX4RH instead of the SAX1 element. Our mesh convergence study shows that four elements through the thickness are sufficient for the imperfect shell (Figure 3-17). Hence, at least four elements through the thickness are adopted. The interaction between the shell and the clamp is set as "hard" contact with a friction coefficient of 0.5. In our simulations, we first simulate the initial deformation by imposing a vertical displacement on the plate, and then apply a pressure on the shell to deflate the shell. The displacement of the plate is varied from 0 to 0.3 mm. Figure 3-15D shows that the deformation due to clamping is localized at the base, while the body of the shell is not affected. In Figure 3-16B, the response of the imperfect shell is also not sensitive to the initial deformation caused by clamping. From these results, we conclude that it is reasonable to neglect the initial deformation of the imperfect shell due to clamping.

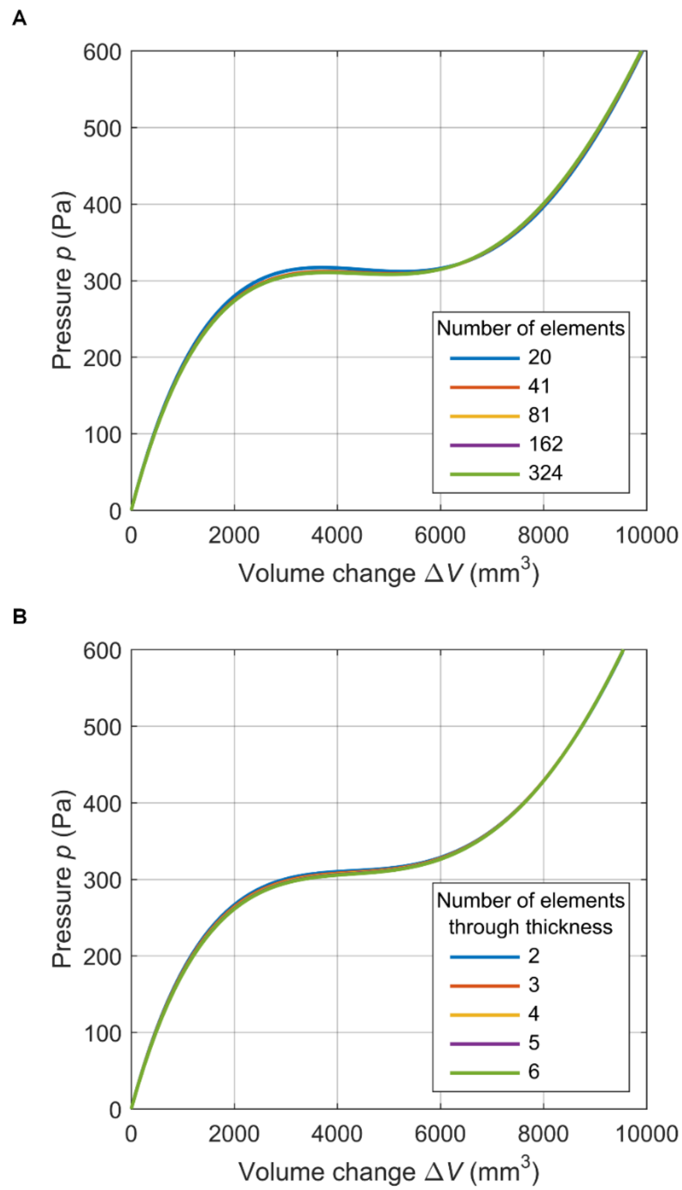

Figure 3-17 Mesh convergence study of the imperfect shell. (A) SAX1 element. (B) CAX4RH element. Curves of different colors overlay, thereby showing that the simulation results for meshes with given number of elements have converged.

3.6.4.3 Modelling of the bi-shell valve

We now study the collective response of the shells forming our valve system by combining the models of each individual shell into one model. SAX1 elements are used for both constituent shells of the as-designed model, which does not feature any variation in thickness or initial deformation due to clamping. On the other hand, for the realistic model, the thickness variation in the imperfect shell and the initial deformation of the spherical cap are modelled as described above for the realistic model of each shell.

We impose a uniform pressure on both shells, and trace the equilibrium path of the bi-shell system with the modified Riks method. The released energy is calculated as the negative of the area under the pressure-volume curve

$$\Delta U^* = -\int_S p\,\mathrm{d}V \tag{3-9}$$

where S is the equilibrium path from the pre-snapping state (i) to the post-snapping state (ii) (Figure 3-1).

3.6.5 Buckling modes of imperfect shell

While the buckling of the spherical cap subject to uniform pressure has been extensively studied in literature [46, 50, 54], only recently we unveil that of an imperfect shell with a large axisymmetric defect away from the pole [47]. Therein, we investigated an individual imperfect shell with a circular defect, and demonstrated the existence of additional three buckling modes, besides to the classical bifurcation, that can be programmed on demand through geometry tuning.

In the current work, we amend the defect geometry to an elliptical arc for the convenience of manufacturing, and specify two defining parameters (Figure 3-4B): the meridional angles at the upper and lower boundary of the defect θ_U and θ_L. By varying θ_U and θ_L, we can show the emergence of four possible buckling modes (Figure 3-18). For a small defect (Figure 3-18A), the shell defect undergoes the classical bifurcation buckling, which is characterized by a downward dimple at the pole of the hemisphere. The pressure increases rapidly to a high buckling pressure (bifurcation point) before dropping immediately to a low plateau. We name this mode as mode 1 [47]. When the defect size increases, Figure 3-18B shows that the buckling mode changes from the classical bifurcation mode to a snap-through buckling mode, which is characterized by a localized deformation that evolves mainly within the defect (mode 2). Similar to mode 1, the pressure attains the maximum at a small volume change (limit point 1). For further increase of defect size (Figure 3-18C), the maximum pressure is reached when the main deformation localizes below the defect (mode 3). Dissimilar from mode 1 and mode 2, the pressure in mode 3 gradually increases to the maximum at a much larger volume change (limit point 2). Depending on the shell geometry, the pressure may also show a plateau before the attainment of the maximum pressure (Figure 3-1E). In a special case (Figure 3-18D), the shell buckles with a mixed mode that combines mode 2 and mode 3. The pressure shows a lower peak at a small volume change (limit point 1) before finally attaining the maximum value at a large change in volume (limit point 2).

The four buckling modes identified above can be overlaid onto the map of the attainable valve output illustrated in Figure 3-4. The result is shown in Figure 3-19. Here, the boundary (red line) is marked between mode 1 and 2, where the imperfect shell collapse immediately upon deflation, and the zone of mode 3 and 4, where the imperfect shell can undergo a large deformation before collapse. The region of mode 1 and 2 is on the lower right-hand side of the red line where θ_{U} and θ_{L} are close in value (small defect), whereas the zone of mode 3 and 4 is on the other side where the defect is large.

The map in Figure 3-19 helps gain essential insights into the role the shell defect plays on the performance of our bi-shell valve. In particular, the domain boundaries demonstrate that to maximize the valve output, values of θ_{U} and θ_{L} falling within the zone of mode 3 and 4 should be preferred, as opposed to those of the other zone (mode 1 and 2), where the valve output is practically null. The cause for the difference we observe here lies in the interaction between the spherical cap and the imperfect shell, as discussed in Section S6 of Supporting Information.

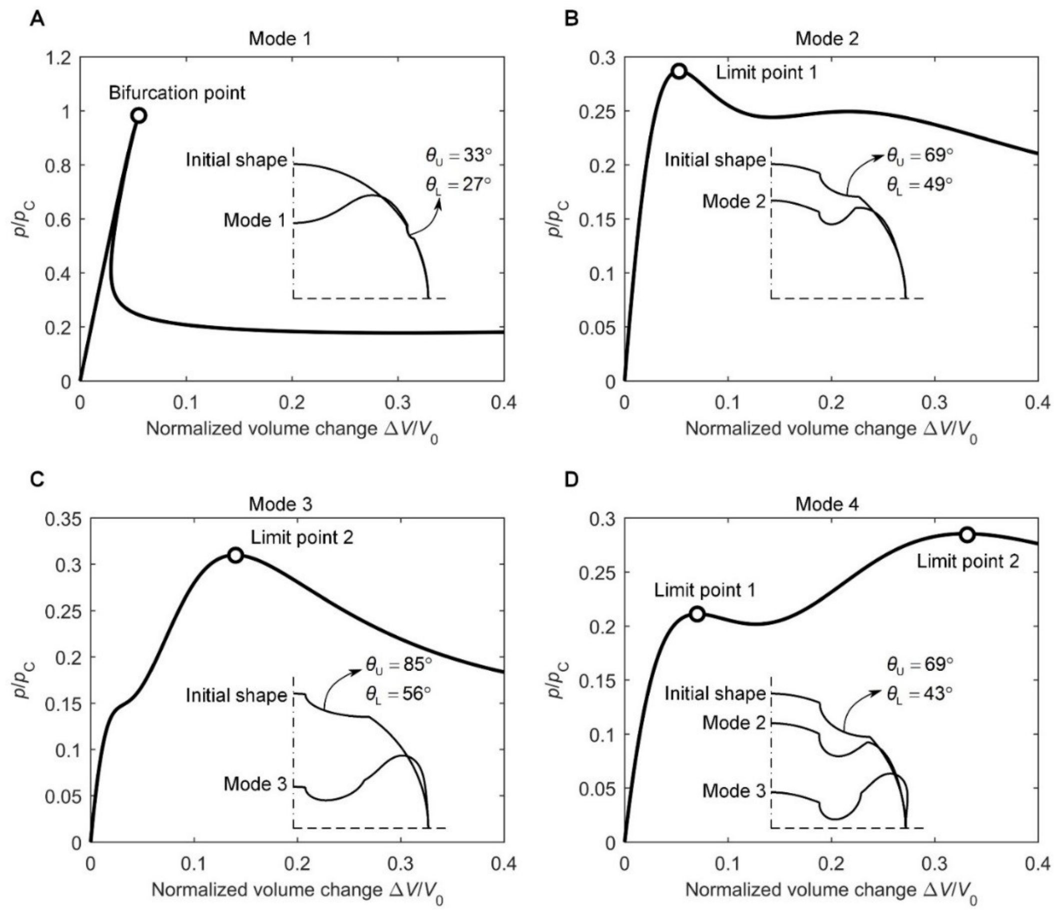

Figure 3-18 Possible deformation modes leading to shell collapse. (a) Mode 1: Bifurcation buckling with a dimple-like shape response. (b) Mode 2: Snap-through buckling 1 characterized by localized deformation within the imperfection. (c) Mode 3: Snap-through buckling 2 with localized deformation below the imperfection. (d) Mode 4: Snap-through buckling combining mode 2 and 3.

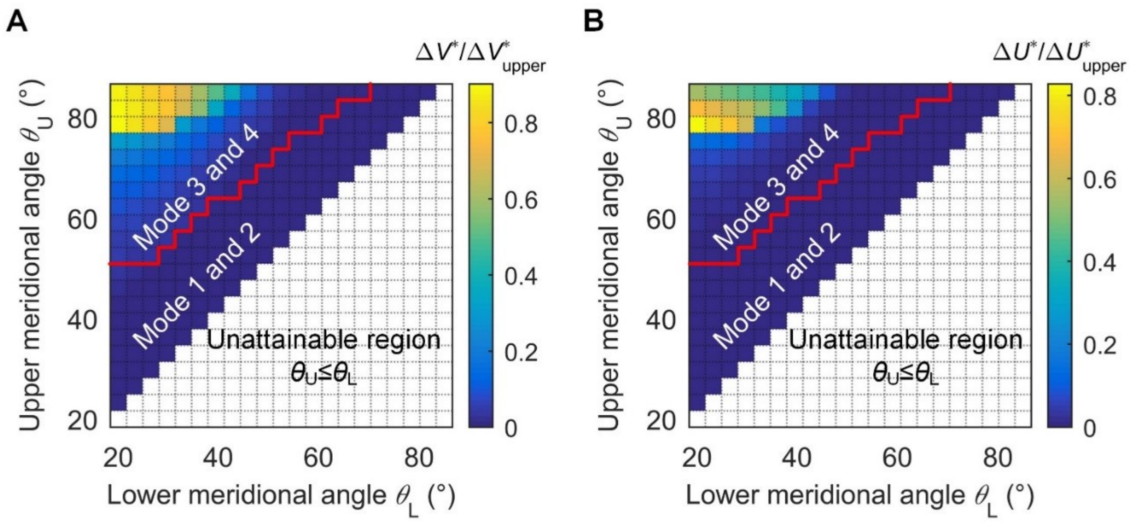

Figure 3-19 Attainable valve output with corresponding buckling modes. (A) Attainable volume change. (B) Attainable released energy. The red line marks the boundary between the zone of mode 1 and 2 and the zone of mode 3 and 4.

3.6.6 Interaction between spherical cap and imperfect shell

Interaction between shells

In our bi-shell valve, the total volume change of the imperfect shell and the spherical cap is determined by the input volume change dispense by the syringe. Since the air compressibility can be neglected (see 3.6.3), the sum of the volume change of each shell (ΔV_1 and ΔV_2) should balance that of the syringe (ΔV_{in}) such that

$$\Delta V_1 + \Delta V_2 = \Delta V_{\text{in}} \tag{3-10}$$

When the imperfect shell and the spherical cap are slowly deflated by the syringe, their pressure at the quasi-equilibrium state must be equal

$$p_1(\Delta V_1) = p_2(\Delta V_2) \tag{3-11}$$

where $p_1(\Delta V_1)$ and $p_2(\Delta V_2)$ are the pressure of each shell as a function of its own volume change. Substituting Eq. (3-10) into Eq. (3-11) yields

$$p_1\left(\Delta V_1\right)=p_2\left(\Delta V_{\text{in}}-\Delta V_1\right) \tag{3-12}$$

At the pre-snapping state (i), Eqs. (3-11) and (3-12) are rewritten as

$$p_1\left(\Delta V_{1(\text{i})}\right)=p_2\left(\Delta V_{\text{in(i)}}-\Delta V_{1(\text{i})}\right)=p_2\left(\Delta V_{2(\text{i})}\right) \tag{3-13}$$

where the subscript (i) denotes the pre-snapping state. While the pre-snapping state of the spherical cap is determined by its own buckling point, the pre-snapping state of the imperfect shell can be determined by finding the value of $\Delta V_{2(\text{i})}$ that satisfies Eq. (3-13).

At the post-snapping state (ii), the balance of pressure is rewritten as

$$p_1\left(\Delta V_{1(\text{i})}+\Delta V^*\right)=p_2\left(\Delta V_{\text{in(i)}}-\left(\Delta V_{1(\text{i})}+\Delta V^*\right)\right)=p_2\left(\Delta V_{2(\text{i})}-\Delta V^*\right) \tag{3-14}$$

where ΔV^* is the volume change due to snapping. Since $\Delta V_{1(\text{i})}$ and $\Delta V_{2(\text{i})}$ are already known from Eq. (3-13), the post-snapping state (ii) can be determined by finding the volume change ΔV^* that satisfies Eq. (3-14).

When the pre and post-snapping states have been determined, the released energy can be calculated from the separate response of each shell as

$$\Delta U^*=-\int_{\Delta V_{1(\text{i})}}^{\Delta V_{1(\text{ii})}} p_1 \mathrm{d}V-\int_{\Delta V_{2(\text{i})}}^{\Delta V_{2(\text{ii})}} p_2 \mathrm{d}V \tag{3-15}$$

where $\Delta V_{1(\text{ii})}=\Delta V_{1(\text{i})}+\Delta V^*$ and $\Delta V_{2(\text{ii})}=\Delta V_{2(\text{i})}-\Delta V^*$ are the volume changes at the post-snapping states.

Since Eq. (3-15) does not require handling the simulation of the whole valve, rather it allows to determine the global performance of the valve from those of the constituents. For this reason, the approach that we propose in this work enables a sizeable reduction of the computational cost, and can be readily used to compute the attainable valve output that is plotted in Figure 3-4.

Relation between shell interaction and valve output

Eqs. (3-10) to (3-15) provide a mathematical description of the general interaction between the shells. However, they have been applied neither to assess the pressure volume curves of the individual shells nor to calculate the valve output. In this section, we apply these equations to analyze a group of pressure-volume curves with changing thickness so as to further explain the relation between shell interaction and valve output. Our specific focus is on understanding the reason for the small yellow regions in Figure 3-4, where the volume change and released energy reach the maximum values.

Figure 3-20 shows a set of the pressure-volume responses of the shells illustrated in Figure 3-4B. The curves pertain to a spherical cap (red line) and a an array of imperfect shells with varying thickness t_2/R (green and black lines). A range of responses can be observed.

- The green curves represent imperfect shells with $0.045 < t_2 / R < 0.055$. Here, the plateau pressure is located between the pre and post-snapping pressure p_{i} and p_{ii}, thereby allowing a large volume change at the plateau stage attained with a minor decrease in pressure resistance. This large volume change is a prerequisite for the shell to release a large amount of energy, hence to maximize the valve performance output. When the plateau pressure values gradually approaches p_{i} with increasing thickness t_2 / R, the released energy reaches a maximum value of $\Delta U/\Delta U_{\mathrm{upper}} = 0.70$ at $t_2 / R = 0.054$ with a sizeable volume change of $\Delta V/\Delta V_{\mathrm{upper}} = 0.81$.
- On the other hand, the black lines describe responses governed by $t_2 / R < 0.045$ and $t_2 / R > 0.055$. In this case, the plateau pressure is either lower or higher than both the pre and post-snapping pressure. Snapping occurs outside the plateau stage, thus causing a fast drop in pressure from p_{i} to p_{ii}. This set of imperfect shells (black) can only snap for a tiny volume change, and release a small amount of elastic energy as opposed to the imperfect shells in the range $0.045 < t_2 / R < 0.055$. Moreover, the thinnest shell with $t_2 / R = 0.02$ have a maximum pressure that is lower than the buckling pressure of the spherical cap. In this case, the bi-shell system cannot snap because the pressure is unable to reach the buckling pressure of the cap.

A comparison of Figure 3-18 with Figure 3-20 highlights that only mode 3 and 4 are suitable for the bi-shell valve. In mode 1 and 2, the pressure of the imperfect shell quickly reaches the maximum with a small volume change. On one hand, if the maximum pressure is larger than the buckling pressure of the spherical cap, the shell interaction will be similar to the case in Figure 3-20 for thick imperfect shells with $t_2 / R > 0.055$ (black lines on the left). The bi-shell valve can only snap for a small volume change and released energy. On the other hand, if the maximum pressure is less than the buckling pressure of the spherical cap, there will be no snapping at all, as in the case with the thinnest imperfect shell ($t_2 / R = 0.02$). In mode 3 and 4, the imperfect shell can undergo a large deformation before attaining the maximum pressure, a response that can potentially form a plateau of pressure before collapse. The green lines in Figure 3-20 therefore identify the set of bi-shell valves that can attain a large volume change when the plateau pressure is between the pre and post-snapping states; in addition, their maximum values of released energy can be obtained when the plateau pressure is just below the pre-snapping pressure.

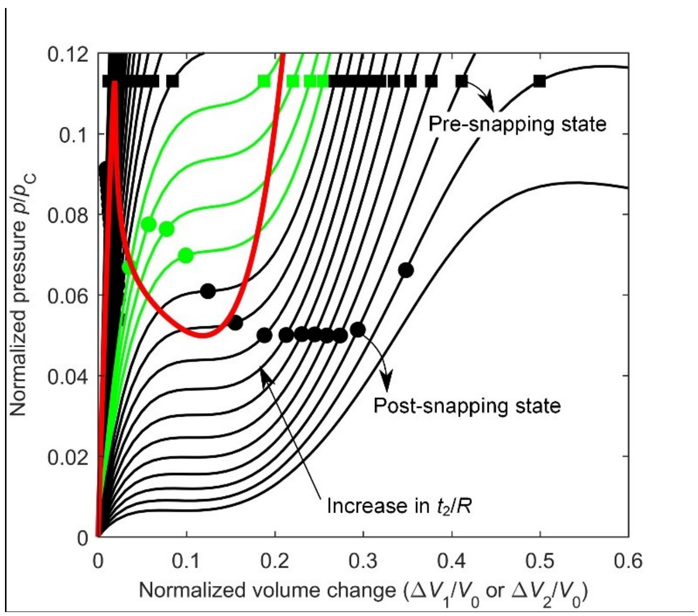

Figure 3-20 Pressure-volume response of the shells in Figure 3-4B. The red curve represents the spherical cap. The green lines describe imperfect shells in the range of $0.045 < t_2 / R < 0.055$, while the black curves pertain to the remaining set of imperfect shells ($0.02 \le t_2 / R < 0.045$ and $0.055 < t_2 / R \le 0.1$). The square and circular dots mark the pre and post-snapping states of each imperfect shell.

3.6.7 Upper bounds of valve output

Here we study the upper bounds of our valve output for both volume and released energy.

Figure 3-21 shows two representative curves of pressure-volume, each representing one individual shell, the spherical cap (A) and the imperfect shell (B). Upon snapping, the pressure of both shells decreases from p_{i} to p_{ii}. In ideal conditions, we could assume the post-snapping pressure of the imperfect shell retains the pre-snapping pressure p_{i} (dashed line in Figure 3-21B). Thus, the pressure of the spherical cap could also retain p_{i}, thus leading to a post-snapping volume change of $\Delta V_{1(\mathrm{iii})}$ (Figure 3-21A). Since it is unrealistic for the imperfect shell to have a post-snapping pressure higher than p_{i}, the post-snapping volume change of the spherical cap will never get larger than $\Delta V_{1(\mathrm{iii})}$. Thus, $\Delta V^{*}_{\mathrm{upper}} = \Delta V_{1(\mathrm{iii})} - \Delta V_{1(\mathrm{i})}$ is the upper bound for the volume change output.

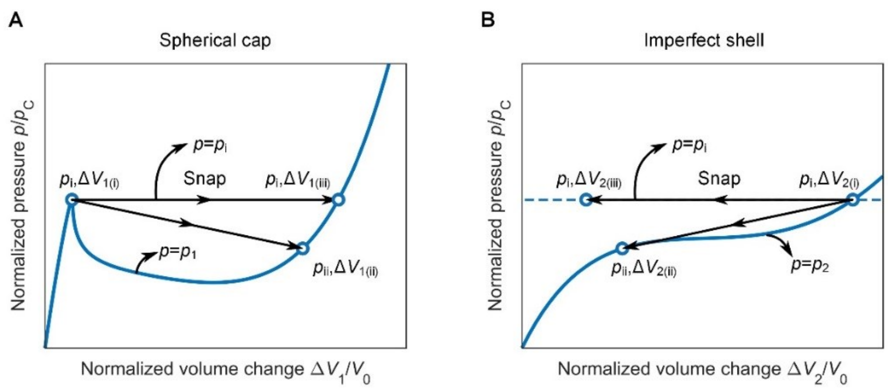

Figure 3-21 Representative pressure-volume responses of individual shells. (A) Spherical cap. (B) Imperfect shell. The dashed line in (B) shows an ideal scenario describing the case where the pressure of the imperfect shell does not drop after snapping; this phenomenon leads to state (iii) with pressure p_{i} and volume change $\Delta V_{2(\mathrm{iii})}$.

As per the released energy, we can use Eq. (3-15) to rewrite the energy released from state (i) to (ii)

$$
\begin{aligned}
\Delta U^{*}_{(\mathrm{ii})} &= -\int_{\Delta V_{1(\mathrm{i})}}^{\Delta V_{1(\mathrm{ii})}} p_1 \mathrm{d}V - \int_{\Delta V_{2(\mathrm{i})}}^{\Delta V_{2(\mathrm{ii})}} p_2 \mathrm{d}V \\
&= -\int_{\Delta V_{1(\mathrm{i})}}^{\Delta V_{1(\mathrm{iii})}} p_1 \mathrm{d}V - \int_{\Delta V_{1(\mathrm{iii})}}^{\Delta V_{1(\mathrm{ii})}} p_1 \mathrm{d}V - \int_{\Delta V_{2(\mathrm{i})}}^{\Delta V_{2(\mathrm{ii})}} p_2 \mathrm{d}V - \int_{\Delta V_{2(\mathrm{i})}}^{\Delta V_{2(\mathrm{iii})}} p_{\mathrm{i}} \mathrm{d}V + \int_{\Delta V_{2(\mathrm{i})}}^{\Delta V_{2(\mathrm{iii})}} p_{\mathrm{i}} \mathrm{d}V \\
&= \left(-\int_{\Delta V_{1(\mathrm{i})}}^{\Delta V_{1(\mathrm{iii})}} p_1 \mathrm{d}V - \int_{\Delta V_{2(\mathrm{i})}}^{\Delta V_{2(\mathrm{iii})}} p_{\mathrm{i}} \mathrm{d}V \right) + \left(-\int_{\Delta V_{1(\mathrm{iii})}}^{\Delta V_{1(\mathrm{ii})}} p_1 \mathrm{d}V - \int_{\Delta V_{2(\mathrm{i})}}^{\Delta V_{2(\mathrm{ii})}} p_2 \mathrm{d}V + \int_{\Delta V_{2(\mathrm{i})}}^{\Delta V_{2(\mathrm{iii})}} p_{\mathrm{i}} \mathrm{d}V \right) \\
&= \Delta U^{*}_{(\mathrm{iii})} + \left(\int_{\Delta V_{2(\mathrm{ii})}}^{\Delta V_{2(\mathrm{iii})}} p_{\mathrm{i}} \mathrm{d}V - \int_{\Delta V_{1(\mathrm{iii})}}^{\Delta V_{1(\mathrm{ii})}} p_1 \mathrm{d}V + \int_{\Delta V_{2(\mathrm{i})}}^{\Delta V_{2(\mathrm{ii})}} p_{\mathrm{i}} \mathrm{d}V - \int_{\Delta V_{2(\mathrm{i})}}^{\Delta V_{2(\mathrm{ii})}} p_2 \mathrm{d}V \right)
\end{aligned}
\tag{3-16}
$$

where $\Delta U^*_{\text{(ii)}}$ is the released energy from state (i) to (ii), $\Delta U^*_{\text{(iii)}}$ is the released energy from state (i) to (iii). Here the snapping pressure of the spherical cap p_{i} is a constant, while p_1 and p_2 are function of the volume change of each shells (blue lines in Figure 3-21).

Since the total volume change is constant during snapping, according to Eq. (3-10) we have

$$\Delta V_{1\text{(i)}} + \Delta V_{2\text{(i)}} = \Delta V_{1\text{(ii)}} + \Delta V_{2\text{(ii)}} = \Delta V_{1\text{(iii)}} + \Delta V_{2\text{(iii)}} \tag{3-17}$$

The first two terms in the bracket of the last row of Eq. (3-16) are

$$\begin{aligned}\int_{\Delta V_{2\text{(ii)}}}^{\Delta V_{2\text{(iii)}}} p_{\text{i}}\mathrm{d}V - \int_{\Delta V_{1\text{(iii)}}}^{\Delta V_{1\text{(ii)}}} p_1\mathrm{d}V &= p_{\text{i}}\left(\Delta V_{2\text{(iii)}} - \Delta V_{2\text{(ii)}}\right) - \int_{\Delta V_{1\text{(iii)}}}^{\Delta V_{1\text{(ii)}}} p_1\mathrm{d}V \\ &= p_{\text{i}}\left(\Delta V_{1\text{(ii)}} - \Delta V_{1\text{(iii)}}\right) - \int_{\Delta V_{1\text{(iii)}}}^{\Delta V_{1\text{(ii)}}} p_1\mathrm{d}V \\ &= \int_{\Delta V_{1\text{(iii)}}}^{\Delta V_{1\text{(ii)}}} p_{\text{i}}\mathrm{d}V - \int_{\Delta V_{1\text{(iii)}}}^{\Delta V_{1\text{(ii)}}} p_1\mathrm{d}V\end{aligned} \tag{3-18}$$

Since $\Delta V_{1\text{(ii)}} < \Delta V_{1\text{(iii)}}$ and $p_{\text{i}} \geq p_1$, we have

$$\int_{\Delta V_{2\text{(ii)}}}^{\Delta V_{2\text{(iii)}}} p_{\text{i}}\mathrm{d}V - \int_{\Delta V_{1\text{(iii)}}}^{\Delta V_{1\text{(ii)}}} p_1\mathrm{d}V = \int_{\Delta V_{1\text{(iii)}}}^{\Delta V_{1\text{(ii)}}} p_{\text{i}}\mathrm{d}V - \int_{\Delta V_{1\text{(iii)}}}^{\Delta V_{1\text{(ii)}}} p_1\mathrm{d}V < 0 \tag{3-19}$$

Similarly since $\Delta V_{2\text{(i)}} > \Delta V_{2\text{(ii)}}$ and $p_{\text{i}} \geq p_2$, the last two terms in the bracket of the last row of Eq. (3-16) satisfies

$$\int_{\Delta V_{2\text{(i)}}}^{\Delta V_{2\text{(ii)}}} p_{\text{i}}\mathrm{d}V - \int_{\Delta V_{2\text{(i)}}}^{\Delta V_{2\text{(ii)}}} p_2\mathrm{d}V < 0 \tag{3-20}$$

Finally, Substituting Eqs. (3-19) and (3-20) into (3-16), we have

$$\Delta U^*_{\text{(ii)}} < \Delta U^*_{\text{(iii)}} \tag{3-21}$$

The above demonstrate that $\Delta U^*_{\text{upper}} = \Delta U^*_{\text{(iii)}}$ is the upper bound of the released energy. State (iii) therefore describe the upper bounds of both volume change and released energy, which are theoretical limits fully determined by the spherical shell. The volume change and released energy output of a given bi-shell valve can never surpass them, because the inflation of the imperfect shell during snapping can only cause a decrease in pressure.

3.6.8 Flow chart of the design process

Figure 3-22 shows the two-steps approach here proposed for the design of our bi-shell valve. It involves the 4 metrics introduced in the main text of the paper: the upper bounds of volume and energy ($\Delta V^*_{\text{upper}}$ and $\Delta U^*_{\text{upper}}$) and the attainable ranges of output (ΔV^* and ΔU^*) within their respective bounds.

The focus of the first step is on the spherical cap only, and aims at identifying the upper bounds ($\Delta V^*_{\text{upper}}$ and $\Delta U^*_{\text{upper}}$) of the valve output. These quantities set the performance limits imposed by the spherical cap to a bi-shell system with any geometric parameters of the imperfect shell. With these upper bounds, we can select the geometry of a spherical cap (t_1 / R and h / R) that meet the requirements of volume and energy output prescribed by a given application.

In the second step, the emphasis shifts to the imperfect shell, and the goal is to obtain the attainable ranges of volume change ΔV^* and released energy ΔU^* for a bi-shell valve with the spherical cap selected in the first step. We do so by first exploring the design space of the imperfect shell. Then, we complete the valve design by selecting a set of the imperfect shell parameters, i.e. t_2 / R, θ_{U} and θ_{L}, that can meet the valve output requirements of the application (ΔV^* and ΔU^*). If there is no feasible design for the imperfect shell, we then return to the first step to revise the design of the spherical cap. With this approach, we can ensure to fully tap into the full potential of both shells and obtain a valve output that is close to the achievable maximum.

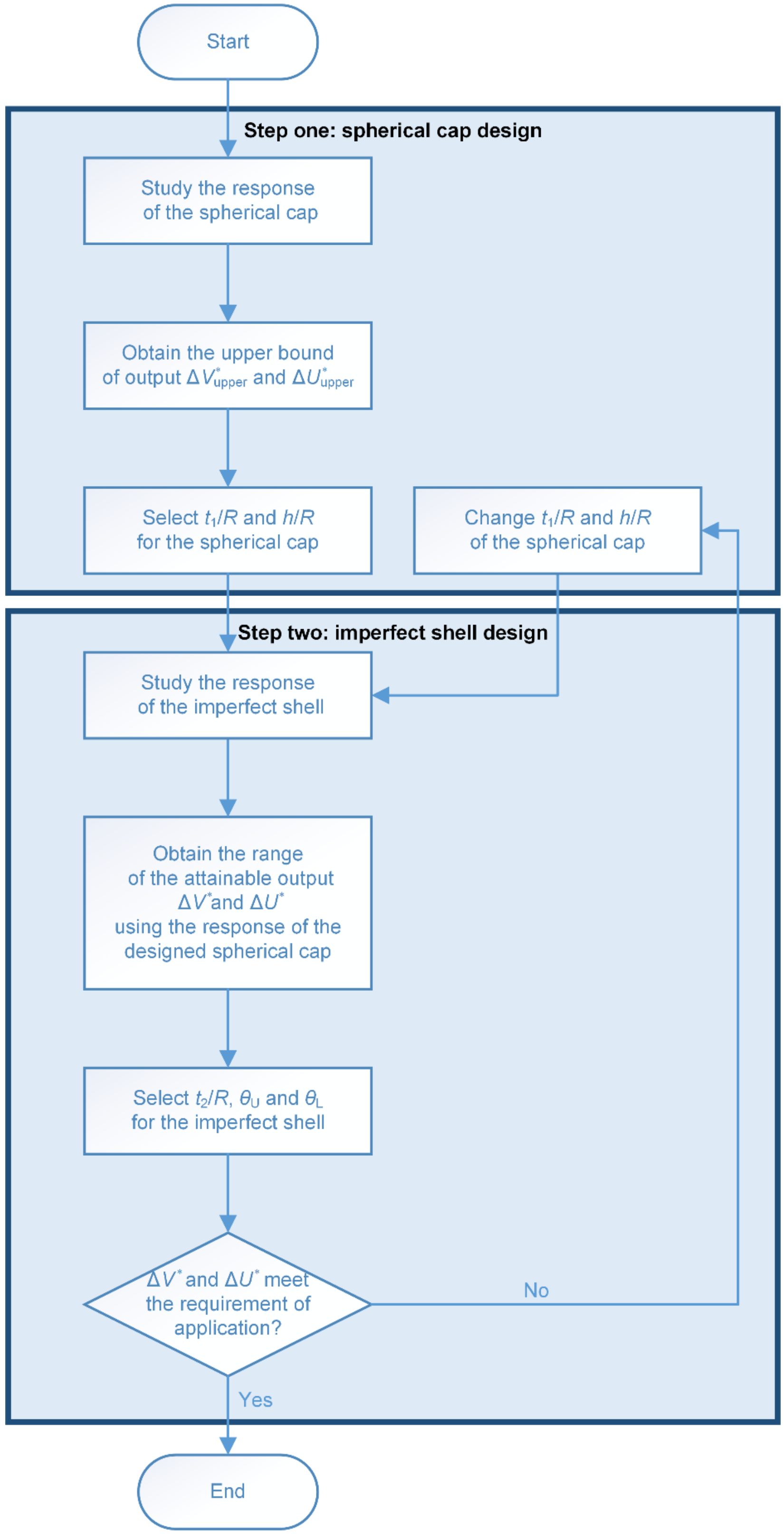
Start
Step one: spherical cap design
Study the response of the spherical cap
Obtain the upper bound of output ΔV^*_{upper} and ΔU^*_{upper}
Select t_1/R and h/R for the spherical cap
Change t_1/R and h/R of the spherical cap
Step two: imperfect shell design
Study the response of the imperfect shell
Obtain the range of the attainable output ΔV^* and ΔU^* using the response of the designed spherical cap
Select t_2/R, θ_U and θ_L for the imperfect shell
ΔV^* and ΔU^* meet the requirement of application?
No
Yes
End

Figure 3-22 Design flowchart describing the steps to design the bi-shell valve.

3.6.9 Alternative designs of the bi-shell valve

The bi-shell valve introduced in the main text operates through deflation. Here we introduce two design variations to achieve alternative functions: a *pneumatic volume fuse* and a *rapid inflation valve*.

Figure 3-23A shows a *pneumatic volume fuse*. This concept modifies the original bi-shell valve operating in a deflation mode in the position of the output chamber, which is here moved on the top of the imperfect shell. In this configuration, before snapping, the imperfect shell can be deflated to generate a continuous volume output ΔV_2 (Figure 3-23B). When the imperfect shell is in the pre-snapping state (i), further deflation will trigger the snapping of the volume fuse, which reduces the volume change of the imperfect shell from state (i) to state (ii). The outcome is a pneumatic fuse: the volume change of the imperfect shell at state (i) sets the threshold of volume output that the fuse cannot exceed.

Figure 3-23C shows a *rapid inflation valve*. The original bi-shell valve concept is here altered by flipping the two elastic shells upside down. This valve works in inflation mode in a way similar to that of the original valve that operation in a deflation mode. When slowly inflated at the inlet (Figure 3-23D), the imperfect shell first inflates to store energy and volume change. Upon snapping, the imperfect shell deflates from state (i) to state (ii) so as to release energy and volume change, while the spherical cap snaps upward. The advantage of this design is the provision of a fast volume output for the rapid inflation of any actuator that may be connected to the outlet.

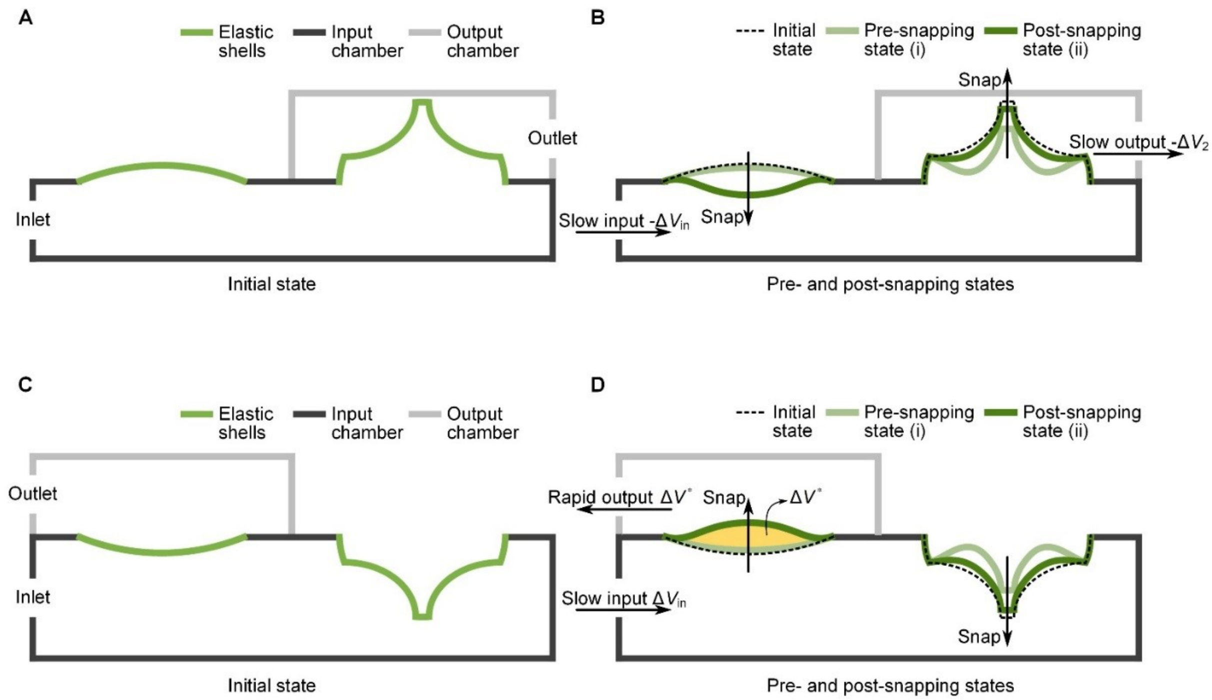

Figure 3-23 Alternative valve designs. (A) and (B) pneumatic volume fuse. (C) and (D) rapid inflation valve.

3.6.10 Effect of elastic modulus on the performance of the bi-shell valve

To study the effect of material elasticity on the performance of the bi-shell valve, we perform a set of numerical simulations, where the shell material is assumed linear elastic with a Young's modulus ranging between 1 and 10 MPa. The geometry of the spherical cap and the imperfect shell are defined as: $R = 25$ mm, $t_1 / R = t_2 / R = 0.05$, $h / R = 0.2$, $\theta_{\mathrm{L}} = 20°$, and $\theta_{\mathrm{U}} = 85.9°$.

In Figure 3-24A, the pressure increases linearly with the Young's modulus, while the volume change is not affected by a change in the Young's modulus values. In Figure 3-24B, the released energy of the bi-shell valve increases linearly with the Young's modulus from 1 to 10 MPa with discrete step of 1 MPa. On the other hand, the volume output of the valve is not affected by a change in the Young's modulus values (Figure 3-24C).

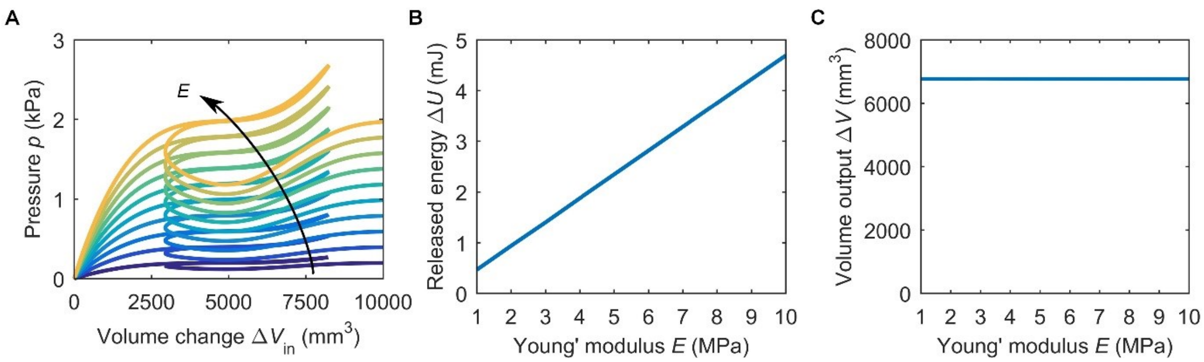

Figure 3-24. Influence of elastic modulus. (A) Pressure-volume change curves, (B) released energy ΔU, and (C) volume output ΔV of bi-shell valves with Young's modulus E increasing from 1 to 10 MPa with discrete step of 1 MPa.

3.6.11 Integration of the bi-shell valve integrated into a soft robot or actuator

To integrate our valve within a soft robot, the output chamber can be merged with the interior of the soft actuator, while the whole system of the bi-shell valve and the soft actuator can be controlled from the input chamber. A possible layout of the valve-actuator integration is given in Figure 3-25. Both the rigid input and output chambers can be replaced with thick soft walls by molding [29]. The integration would only require the merging of both molds, that of the bi-shell valve and that of the soft actuator. The exterior of the robot is purposely left as undefined because it can be shaped by design to deliver a certain function. For example to achieve motion, the exterior body can be designed as a partially corrugated cylinder with grips in contact with the ground [29].

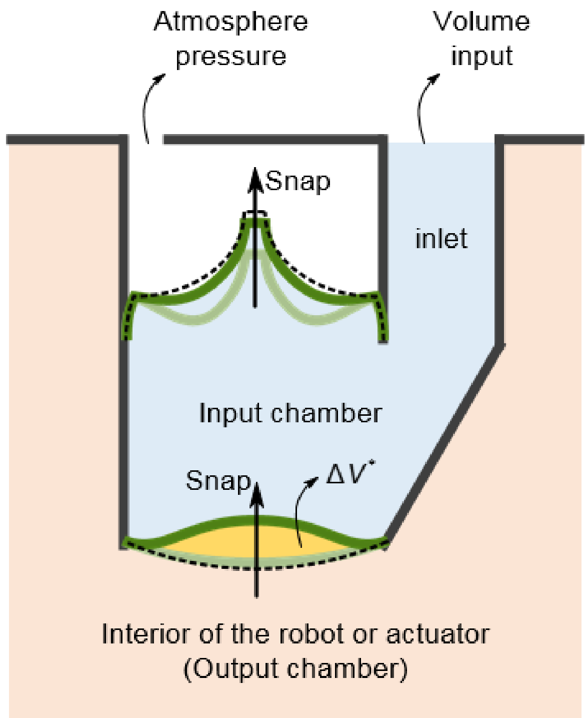

Figure 3-25. Schematic of the bi-shell valve integrated into a soft robot or actuator.

3.6.12 Scenario of a similar valve with only one shell

If there is only the spherical cap (Figure 3-26), there can be no fast transfer of air volume between shells. This means that the total volume of the input and output chambers remains constant. As a result, the flow rate provided at the valve input equals that of the valve output. In our experiment, the flow rate at the valve inlet is 3 mL/min, a value that cannot provide fast actuation. On the other hand, if only the imperfect shell is present, fast actuation cannot yet be achieved. The reason is as for the above. No fast transfer of air volume between shells can occur, hence we cannot convert a low flow rate (input) to a fast flow rate (output).

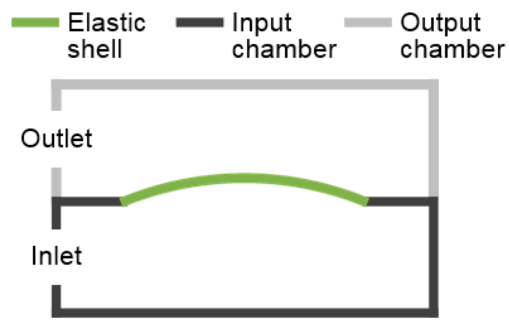

Figure 3-26. Scenario with only the spherical cap.

Movie. S1. Snapping of the bi-shell valve.

Movie. S2. Fast pushing a table tennis ball with a striker actuated through the bi-shell valve.

Movie. S3. Actuation of the striker through the bi-shell valve.

Movie. S4. Actuation of the striker without the bi-shell valve.

Movie. S5. Reversible snapping of the bi-shell valve.

3.7 References

[1] D. Rus and M. T. Tolley, *Design, fabrication and control of soft robots.* Nature, 2015. **521**(7553): p. 467-475.

[2] G. M. Whitesides, *Soft robotics.* Angewandte Chemie International Edition, 2018. **57**(16): p. 4258-4273.

[3] J. H. Pikul, S. Li, H. Bai, R. T. Hanlon, I. Cohen, and R. F. Shepherd, *Stretchable surfaces with programmable 3d texture morphing for synthetic camouflaging skins.* Science, 2017. **358**(6360): p. 210-214.

[4] E. Siéfert, E. Reyssat, J. Bico, and B. Roman, *Bio-inspired pneumatic shape-morphing elastomers.* Nature Materials, 2019. **18**(1): p. 24-28.

[5] E. W. Hawkes, L. H. Blumenschein, J. D. Greer, and A. M. Okamura, *A soft robot that navigates its environment through growth.* Science Robotics, 2017. **2**(8): p. eaan3028.

[6] N. S. Usevitch, Z. M. Hammond, M. Schwager, A. M. Okamura, E. W. Hawkes, and S. Follmer, *An untethered isoperimetric soft robot.* Science Robotics, 2020. **5**(40): p. eaaz0492.

[7] H. Li, J. Yao, C. Liu, P. Zhou, Y. Xu, and Y. Zhao, *A bioinspired soft swallowing robot based on compliant guiding structure.* Soft Robotics, 2020. **7**: p. 491-499.

[8] Y. Tang, Y. Chi, J. Sun, T.-H. Huang, O. H. Maghsoudi, A. Spence, J. Zhao, H. Su, and J. Yin, *Leveraging elastic instabilities for amplified performance: Spine-inspired high-speed and high-force soft robots.* Science Advances, 2020. **6**(19): p. eaaz6912.

[9] Y. Tang and J. Yin, *Design of multifunctional soft doming actuator for soft machines.* Advanced Materials Technologies, 2018. **3**(7): p. 1800069.

[10] L. Qin, X. Liang, H. Huang, C. K. Chui, R. C.-H. Yeow, and J. Zhu, *A versatile soft crawling robot with rapid locomotion.* Soft Robotics, 2019. **6**(4): p. 455-467.

[11] A. Seibel and L. Schiller, *Systematic engineering design helps creating new soft machines.* Robotics and Biomimetics, 2018. **5**(1): p. 5.

[12] Y. Tang, Q. Zhang, G. Lin, and J. Yin, *Switchable adhesion actuator for amphibious climbing soft robot.* Soft Robotics, 2018. **5**(5): p. 592-600.

[13] M. S. Verma, A. Ainla, D. Yang, D. Harburg, and G. M. Whitesides, *A soft tube-climbing robot.* Soft Robotics, 2017. **5**(2): p. 133-137.

[14] J. Shintake, V. Cacucciolo, D. Floreano, and H. Shea, *Soft robotic grippers.* Advanced Materials, 2018. **30**(29): p. 1707035.

[15] Z. Xie, A. G. Domel, N. An, C. Green, Z. Gong, T. Wang, E. M. Knubben, J. C. Weaver, K. Bertoldi, and L. Wen, *Octopus arm-inspired tapered soft actuators with suckers for improved grasping.* Soft Robotics, 2019. **7**(5): p. 639-648.

[16] A. Ainla, M. S. Verma, D. Yang, and G. M. Whitesides, *Soft, rotating pneumatic actuator.* Soft Robotics, 2017. **4**(3): p. 297-304.

[17] P. Polygerinos, K. C. Galloway, E. Savage, M. Herman, K. O. Donnell, and C. J. Walsh. *Soft robotic glove for hand rehabilitation and task specific training*. In *2015 IEEE International Conference on Robotics and Automation (ICRA)*. 2015.

[18] J. Fang, J. Yuan, M. Wang, L. Xiao, J. Yang, Z. Lin, P. Xu, and L. Hou, *Novel accordion-inspired foldable pneumatic actuators for knee assistive devices.* Soft Robotics, 2020. **7**(1): p. 95-108.

[19] C. Paul, *Morphological computation: A basis for the analysis of morphology and control requirements.* Robotics and Autonomous Systems, 2006. **54**(8): p. 619-630.

[20] H. Hauser, A. J. Ijspeert, R. M. Füchslin, R. Pfeifer, and W. Maass, *Towards a theoretical foundation for morphological computation with compliant bodies.* Biological Cybernetics, 2011. **105**(5): p. 355-370.

[21] P. Polygerinos, N. Correll, S. A. Morin, B. Mosadegh, C. D. Onal, K. Petersen, M. Cianchetti, M. T. Tolley, and R. F. Shepherd, *Soft robotics: Review of fluid-driven intrinsically soft devices; manufacturing, sensing, control, and applications in human-robot interaction.* Advanced Engineering Materials, 2017. **19**(12): p. 1700016.

[22] D. J. Preston, P. Rothemund, H. J. Jiang, M. P. Nemitz, J. Rawson, Z. Suo, and G. M. Whitesides, *Digital logic for soft devices.* Proceedings of the National Academy of Sciences, 2019. **116**(16): p. 7750-7759.

[23] M. Wehner, R. L. Truby, D. J. Fitzgerald, B. Mosadegh, G. M. Whitesides, J. A. Lewis, and R. J. Wood, *An integrated design and fabrication strategy for entirely soft, autonomous robots.* Nature, 2016. **536**(7617): p. 451-455.

[24] T. Ranzani, S. Russo, N. W. Bartlett, M. Wehner, and R. J. Wood, *Increasing the dimensionality of soft microstructures through injection-induced self-folding.* Advanced Materials, 2018. **30**(38): p. 1802739.

[25] D. Yang, M. S. Verma, J.-H. So, B. Mosadegh, C. Keplinger, B. Lee, F. Khashai, E. Lossner, Z. Suo, and G. M. Whitesides, *Buckling pneumatic linear actuators inspired by muscle.* Advanced Materials Technologies, 2016. **1**(3): p. 1600055.

[26] B. Mosadegh, P. Polygerinos, C. Keplinger, S. Wennstedt, R. F. Shepherd, U. Gupta, J. Shim, K. Bertoldi, C. J. Walsh, and G. M. Whitesides, *Pneumatic networks for soft robotics that actuate rapidly.* Advanced Functional Materials, 2014. **24**(15): p. 2163-2170.

[27] S. Russo, T. Ranzani, C. J. Walsh, and R. J. Wood, *An additive millimeter-scale fabrication method for soft biocompatible actuators and sensors.* Advanced Materials Technologies, 2017. **2**(10): p. 1700135.

[28] Y.-F. Zhang, C. J.-X. Ng, Z. Chen, W. Zhang, S. Panjwani, K. Kowsari, H. Y. Yang, and Q. Ge, *Miniature pneumatic actuators for soft robots by high-resolution multimaterial 3d printing.* Advanced Materials Technologies, 2019. **4**(10): p. 1900427.

[29] P. Rothemund, A. Ainla, L. Belding, D. J. Preston, S. Kurihara, Z. Suo, and G. M. Whitesides, *A soft, bistable valve for autonomous control of soft actuators.* Science Robotics, 2018. **3**(16): p. 7986.

[30] E. Ben-Haim, L. Salem, Y. Or, and A. D. Gat, *Single-input control of multiple fluid-driven elastic actuators via interaction between bistability and viscosity.* Soft Robotics, 2019. **7**(2): p. 259-265.

[31] B. Gorissen, D. Melancon, N. Vasios, M. Torbati, and K. Bertoldi, *Inflatable soft jumper inspired by shell snapping.* Science Robotics, 2020. **5**(42): p. 1967.

[32] J. T. B. Overvelde, T. Kloek, J. J. A. D'haen, and K. Bertoldi, *Amplifying the response of soft actuators by harnessing snap-through instabilities.* Proceedings of the National Academy of Sciences, 2015. **112**(35): p. 10863-10868.

[33] E. Milana, B. Gorissen, M. D. Voider, and D. Reynaerts. *Design of a bi-segmented soft actuator with hardware encoded quasi-static inflation sequence*. In *2018 IEEE International Conference on Soft Robotics (RoboSoft)*. 2018.

[34] C. Keplinger, T. Li, R. Baumgartner, Z. Suo, and S. Bauer, *Harnessing snap-through instability in soft dielectrics to achieve giant voltage-triggered deformation.* Soft Matter, 2012. **8**(2): p. 285-288.

[35] T. Li, C. Keplinger, R. Baumgartner, S. Bauer, W. Yang, and Z. Suo, *Giant voltage-induced deformation in dielectric elastomers near the verge of snap-through instability.* Journal of the Mechanics and Physics of Solids, 2013. **61**(2): p. 611-628.

[36] L. Hines, K. Petersen, and M. Sitti, *Inflated soft actuators with reversible stable deformations.* Advanced Materials, 2016. **28**(19): p. 3690-3696.

[37] R. Baumgartner, A. Kogler, J. M. Stadlbauer, C. C. Foo, R. Kaltseis, M. Baumgartner, G. Mao, C. Keplinger, S. J. A. Koh, N. Arnold, Z. Suo, M. Kaltenbrunner, and S. Bauer, *A*

lesson from plants: High-speed soft robotic actuators. Advanced Science, 2020. **7**(5): p. 1903391.
[38] M. Garrad, G. Soter, A. T. Conn, H. Hauser, and J. Rossiter. *Driving soft robots with low-boiling point fluids*. In *2019 2nd IEEE International Conference on Soft Robotics (RoboSoft)*. 2019.
[39] R. F. Shepherd, A. A. Stokes, J. Freake, J. Barber, P. W. Snyder, A. D. Mazzeo, L. Cademartiri, S. A. Morin, and G. M. Whitesides, *Using explosions to power a soft robot.* Angewandte Chemie International Edition, 2013. **52**(10): p. 2892-2896.
[40] M. T. Tolley, R. F. Shepherd, M. Karpelson, N. W. Bartlett, K. C. Galloway, M. Wehner, R. Nunes, G. M. Whitesides, and R. J. Wood. *An untethered jumping soft robot*. In *2014 IEEE/RSJ International Conference on Intelligent Robots and Systems*. 2014.
[41] M. Loepfe, C. M. Schumacher, U. B. Lustenberger, and W. J. Stark, *An untethered, jumping roly-poly soft robot driven by combustion.* Soft Robotics, 2015. **2**(1): p. 33-41.
[42] N. W. Bartlett, M. T. Tolley, J. T. B. Overvelde, J. C. Weaver, B. Mosadegh, K. Bertoldi, G. M. Whitesides, and R. J. Wood, *A 3d-printed, functionally graded soft robot powered by combustion.* Science, 2015. **349**(6244): p. 161-165.
[43] M. Gomez, D. E. Moulton, and D. Vella, *Passive control of viscous flow via elastic snap-through.* Physical Review Letters, 2017. **119**(14): p. 144502.
[44] D. J. Preston, H. J. Jiang, V. Sanchez, P. Rothemund, J. Rawson, M. P. Nemitz, W.-K. Lee, Z. Suo, C. J. Walsh, and G. M. Whitesides, *A soft ring oscillator.* Science Robotics, 2019. **4**(31): p. 5496.
[45] K. Luo, P. Rothemund, G. M. Whitesides, and Z. Suo, *Soft kink valves.* Journal of the Mechanics and Physics of Solids, 2019. **131**: p. 230-239.
[46] J. W. Hutchinson, *Buckling of spherical shells revisited.* Proceedings of the Royal Society A: Mathematical, Physical and Engineering Sciences, 2016. **472**(2195): p. 20160577.
[47] C. Qiao, L. Liu, and D. Pasini, *Elastic thin shells with large axisymmetric imperfection: From bifurcation to snap-through buckling.* Journal of the Mechanics and Physics of Solids, 2020. **141**: p. 103959, 103959.
[48] W. Dreyer, I. Müller, and P. Strehlow, *A study of equilibria of interconnected balloons.* The Quarterly Journal of Mechanics and Applied Mathematics, 1982. **35**(3): p. 419-440.
[49] I. Müller and P. Strehlow, *Rubber and rubber balloons: Paradigms of thermodynamics*. 2004: Springer.
[50] J. Paulose and D. R. Nelson, *Buckling pathways in spherical shells with soft spots.* Soft Matter, 2013. **9**(34): p. 8227-8245.
[51] H. N. R. Wagner, C. Hühne, and S. Niemann, *Robust knockdown factors for the design of spherical shells under external pressure: Development and validation.* International Journal of Mechanical Sciences, 2018. **141**: p. 58-77.
[52] S. Haddadin, A. Albu-Schäffer, and G. Hirzinger, *Requirements for safe robots: Measurements, analysis and new insights.* The International Journal of Robotics Research, 2009. **28**(11-12): p. 1507-1527.
[53] M. A. Unger, H.-P. Chou, T. Thorsen, A. Scherer, and S. R. Quake, *Monolithic microfabricated valves and pumps by multilayer soft lithography.* Science, 2000. **288**(5463): p. 113-116.

[54] A. Lee, F. López Jiménez, J. Marthelot, J. W. Hutchinson, and P. M. Reis, *The geometric role of precisely engineered imperfections on the critical buckling load of spherical elastic shells.* Journal of Applied Mechanics, 2016. **83**(11): p. 111005-111005-111011.
[55] M. Pezzulla, S. A. Shillig, P. Nardinocchi, and D. P. Holmes, *Morphing of geometric composites via residual swelling.* Soft Matter, 2015. **11**(29): p. 5812-5820.

Chapter 4

Conclusions and future work

Chapter 4: Conclusions and future work

4.1 Summary of the main results

This thesis has investigated the mechanics of shells, with a focus on two intertwined aspects: 1) the existence of multiple buckling modes in a spherical shell shaped with a large axisymmetric imperfection, and 2) the exploitation of the interaction between buckling of an imperfect shell and a shallow spherical cap for the design of a soft valve that can fast actuate soft robots.

Chapter 2 has examined the buckling of imperfect spherical shells subject to uniform external pressure. Current studies have mainly aimed at small-sized imperfections and investigated their effects on the buckling pressure of spherical shells, whereas defects that can prevent the immediate collapse of the shell have not been explored. In this thesis, we have proposed a large axisymmetric imperfection in the form of a circular arc that can be programed to offer a sizable tunability on the buckling landscape of spherical shells. The buckling response of the imperfect shell has been studied through a theory that employs exact formulations of the middle surface strains, curvature changes, and live pressure loading as well as validating experiments and numerical simulations. The main results are summarized as follows:

- The proposed large as-designed imperfection can be integrated into the geometry of spherical shells to avoid the classical bifurcation buckling that typically occurs at a tiny volume change. The snap-through buckling triggered by this imperfection enables an increasing post-buckling pressure until the attainment of the maximum pressure at a large volume change as high as 0.4 of the volume enclosed by the shell. Furthermore, the maximum pressure of the imperfect shell is reduced by only 66% from the theoretical buckling pressure of a shell with perfect geometry. This is in contrast to the 90% decrease of maximum pressure reported in the literature for as-manufactured shells.
- The buckling of the imperfect shell under pressure is dominated by axisymmetric deformations, while non-axisymmetric deformations only occur during the snap-through buckling prior to the attainment of the maximum pressure. The maximum pressure from numerical and theoretical analysis with axisymmetric deformations shows only a small

discrepancy (below 4%) from the non-axisymmetric case, therefore retaining a sufficient level of accuracy for the study of the buckling response.

- The imperfection sensitivity study has revealed the existence of four possible buckling modes for the imperfect shell with axisymmetric defect. These include the well-known bifurcation mode for small-sized imperfections and three snap-through modes for large-sized imperfections. The competition between buckling modes brings a sizable tunability on the attainable maximum pressure ($p_{\max} / p_{\mathrm{C}} = 0.21$ to 0.91) and volume change ($V_{\max} / V_0 = 2\%$ to 52%) as well as the snap-through behaviors, which could be exploited for the design of soft robots and morphing metamaterials.

Chapter 3 has introduced a bi-shell valve that utilizes the snap-through buckling and interaction of its constituent shells to achieve rapid actuation of soft pneumatic robots. The valve consists of a shallow spherical cap and an imperfect hemispherical shell that has the type of large geometric defect that has been fully investigated in Chapter 2. The concerted snapping of these shells enables the valve to passively translate a slow volume input into a fast volume output, which can be effectively programed through geometric tuning to satisfy the requirement of soft robotic applications. The following summarizes the main results:

- Upon the snapping of the spherical cap, a considerable amount of volume change and elastic energy is released by the bi-shell valve. This energy is stored during the deflation of the imperfect shell prior to snapping. The snapping pressure and the upper bounds of the volume change and released energy of the valve are determined by the spherical cap, while the attainable valve outputs are controlled by the interaction between the cap and the imperfect shell. Performance metrics describing the valve output have been introduced along with a two-steps design strategy that can guide the selection of the constituents for soft robotic applications.
- Compared to existing methods for fast actuation that demand a large set of components or modifications to the actuator design, the bi-shell valve here introduced can be easily implemented with a simple volume input dispensed through a syringe to quickly actuate an existing robot. The illustrative application has shown that this valve can actuate a pneumatic striker within 0.16s.

- The volume output of the valve can be autonomously limited to the volume of the actuator at the outlet by the compliance of the constituent shells, thus protecting the actuator from any possible damage due to excessive deflation. Furthermore, the bi-shell valve has been shown capable of repetitive fast actuation due to the elasticity of the shells, which can be achieved through cyclic loop of deflation and inflation at the valve inlet.
- Two variational designs of the bi-shell valve have been proposed. One is a pneumatic volume fuse that reduces the volume output once a threshold is reached. The other is a rapid inflation valve that can produce a fast output for the inflation of soft actuators, as opposed to the bi-shell valve whose output is for deflation. These variational designs have shown that the design of our bi-shell valve is versatile and can be exploited to offer a new function for the control of soft pneumatic actuators and robots.

4.2 Original contributions

The following list summarizes the main findings emerging from this thesis.

- A large axisymmetric imperfection in the form of a circular arc has been for the first time introduced to escape the classical bifurcation buckling of elastic spherical shells subject to uniform external pressure. The outcome is snap-through buckling with a stable post-buckling behavior that exhibits increasing pressure resistance over a large volume change.
- Exact expressions of the stretching and bending strain measures as well as live pressure loading have been derived for the imperfect shell to predict its axisymmetric buckling response under external pressure with large displacements and rotations. Results have demonstrated that the axisymmetric deformation can provide a sufficient level of approximation for shell analysis and design.
- The imperfection sensitivity study has unveiled four buckling modes for the imperfect shell. Tuning the imperfection geometry and shell thickness to radius ratio enables to program the shell response, in particular the normalized maximum pressure, the snap ratio of pressure, and the ratio between snap-through pressure and the maximum pressure, along with their counterparts in volume change .

- Exploiting the findings in Chapter 2, a bi-shell valve that consists of an imperfect shell and a shallow spherical cap has been for the first time proposed for the rapid actuation of soft pneumatic robots under volume control. This valve is ready for use in existing soft robots without any modification to their body architecture.
- The bi-shell valve is the first that can directly capture the snapping deformation of volume-controlled shells to generate a volume output for the rapid actuation of soft pneumatic robots. The snapping of the valve under volume control is enabled by the interaction between the constituent shells, which cannot be achieved with only one shell as in the soft valves existing in the literature.
- The upper bounds and performance metrics of the bi-shell valve have been introduced according to the role of the constituent shells in their snapping interaction. A two-steps design strategy has been proposed to reach the full potential of both shells and to yield a valve output close to the achievable maximum.

4.3 Future work

The following is proposed as a future continuation to this work:

- Chapter 2 has demonstrated that a large axisymmetric imperfection in the form of a circular arc can be introduced to escape the classical bifurcation buckling of spherical shells subject to uniform external pressure. Future work can investigate the effects of imperfections in the form of other geometric shapes on shell buckling.
- Besides elastic shells, shells made of other materials, e.g. glasses, metals, and ceramics, are also widespread in engineering applications. The application of large geometric imperfections in tuning the mechanical response of these shells can be explored in the future.
- Shell structures are not only used to carry pressure loadings, but can also be under other loading scenarios, such as blast loading, point force, indentation, electromagnetic force, and combined loadings. Future work can study the response of the imperfect shell in these loading conditions.

- Chapter 3 has presented a bi-shell valve to control the actuation of soft pneumatic robots. The concept of this valve can be extended to propose other soft valve concepts with novel function, such as a pneumatic volume fuse and a rapid inflation valve. Future work can fabricate prototypes to validate these variations and characterize their performance.
- While this work has demonstrated that buckling interaction of elastic thin shells can be utilized by a soft bi-shell valve for fast actuation, this strategy can be extended to other applications, such as for the development of pneumatic metamaterials with digital logics.

4.4 Publications

4.4.1 Refereed journals

- C. Qiao, L. Liu, and D. Pasini, Bi-shell valve for fast actuation of soft pneumatic actuators via shell snapping interaction. *Advanced Science* 2021, 2100445. https://doi.org/10.1002/advs.202100445
- C. Qiao, L. Liu, and D. Pasini, Elastic thin shells with large axisymmetric imperfection: From bifurcation to snap-through buckling. *Journal of the Mechanics and Physics of Solids*, 2020. 141: 103959.
- L. Liu, C. Qiao, H. An, and D. Pasini, Encoding kirigami bi-materials to morph on target in response to temperature. *Scientific Reports*, 2019. 9(1): 19499.

4.4.2 Conference abstracts

- C. Qiao and D. Pasini, From bifurcation to snap-through buckling of elastic thin shells: defect tuning for soft robotic materials, in Virtual Technical Meeting of the Society of Engineering Science 2020, 2020.
- D. Pasini, C. Qiao, From bifurcation to snap-through buckling of elastic thin shells for soft robotic materials, in APS March Meeting 2021, 2021.
- C. Qiao, L. Liu, D. Pasini, From bifurcation to snap-through buckling of elastic thin shells with large axisymmetric imperfection, abstract accepted for ICTAM 2021, 2021.
- C. Qiao, L. Liu, D. Pasini, A bi-shell valve utilizing shell snapping interaction for fast actuation of pneumatic soft robots, abstract accepted for ICTAM 2021, 2021.